Level set numerical approach to anisotropic mean curvature flow on obstacle

Siddharth Gavhale

Level set numerical approach to anisotropic mean curvature flow on obstacle

A thesis presented for the degree of

Doctor of Philosophy

by

Siddharth Gavhale

Department of Mathematics

Kyoto University, Japan

under the supervision of

Assoc. Prof. Karel Švadlenka

January 2021

Abstract

Level set numerical approach to anisotropic mean curvature flow on obstacle

Siddharth Gavhale

The objective of this work is to deepen the understanding of the anisotropic multiphase mean curvature flow problem in the setting allowing for topological changes where mathematical analysis is still developing. The motivation also comes from applications such as the manufacturing of nanopatterned substrates, where the precise control of the size and location of forming nanoparticles is essential to boost the functionality of the product. Here particles with anisotropic surface energy evolve on a substrate towards a shape with minimum surface energy experiencing topological changes.

We deal with the particular case of *obstalce problem*, which leads to a degenerate, nonlinear partial differential equation. This thesis is divided into three main parts: literature review (Chapters 1, 2), methodology (Chapter 3) and new findings (Chapters 4, 5).

The first part investigates the anisotropic mean curvature flow via a two-phase problem. Further, we discuss implicit and explicit approaches to solve the governing differential equations. We discuss the existence of solutions singularities and summarise known results and properties of the flow. The second part introduces a level set-based numerical method, namely, the thresholding method, to solve governing PDEs of the flow, which can be realized by a suitable convolution kernel. Originally this method was developed for isotropic two-phase problems, which leads to convolution with Gaussian kernel. The extension to the anisotropic case was theoretically addressed by introducing anisotropic kernels by several researchers.

The third part starts with the first contribution of the thesis, which is based on numerical findings:
⋄ *We perform a systematical investigation of the numerical properties of the anisotropic kernels in terms of error behaviour, convergence order, CPU time, etc., through a series of numerical comparison tests using different types of anisotropies. Our findings assess the numerical behaviour of kernels in view of multiphase or obstacle problems.*

Employing the knowledge obtained through the numerical tests, in the final part, we proceed to the analysis of the core problem, i.e., obstacle problem. As a starting point, numerical approximation of the problem is addressed. For the obstacle problem, the explicit approach was implemented by Wang et al. They use surface diffusion as the evolution law and implement a finite element scheme to investigate the resulting shapes of anisotropic particles. However, the explicit approach inherently cannot cope with possible topological changes unless their appearance and nature are apriori known.
To resolve the question of topological changes, Xu et al. in developed a numerical scheme based on the implicit approach. Namely, they solved the obstacle problem using level set approach, but their scheme pertains only to the isotropic energy case. The motivation of this work comes from the absence of methods for obstacle problems that could handle both anisotropic energies and topological changes.

◇ *We construct a new thresholding algorithm for the realization of mean curvature flow on obstacles in the anisotropic setting where interfacial energy depends on the orientation of the interface. The thresholding method is based on a linearization of the original problem leading to an anisotropic diffusion problem, which can be solved by convolution of the characteristic function of a phase with a suitable convolution kernel. The convolution kernels were developed in previous studies. This type of scheme treats the interface implicitly, supporting the natural implementation of topology changes, such as merging and splitting. Further, we modify the algorithm to improve its performance at contact points by implementing a time-scaling.*

As an important property, we rigorously prove the stability of the algorithm. Moreover, we provide a detailed report on the numerical properties of the proposed algorithm. In this way, the present work closes the gap between works of Wang et al. and Xu et al. and allows for simulations of obstacle problems involving topology changes, as demanded in applications.

***Codes**: All the codes generated during this research are available here and at the link https://github.com/siddharthgavhale/ThesisCodes*

Keywords: interface evolution, anisotropic energy, mean curvature flow, obstacle problem, thresholding method, convolution kernels, topology change, numerical analysis.
Mathematics Subject Classification 2020: 53E10, 65K10, 74P20

Advisor: Assoc. Prof. Karel Švadlenka

Contents

List of Figures

List of Tables

List of Algorithms

List of notations

$\mathbb{N}$	set of natural numbers
$\mathbb{Z}$	set of integers numbers
$\mathbb{R}$	set of real numbers
$\lvert \cdot \rvert$	Euclidean norm
$\mathbb{S}^{d-1}$	unit sphere in $\mathbb{R}^d$
∇	gradient vector
Δ	Laplace operator
$\Delta_{\Gamma(t)}$	Laplace-Beltrami operator
$L^2(\Omega)$	set of square integrable L^2 functions with domain Ω
$\boldsymbol{n}$	unit normal vector to a given set
$\boldsymbol{t}$	unit tangent vector to a given set
C^k	class of functions with k continuous derivatives
$\langle \cdot, \cdot \rangle$	inner product
$x \cdot y$	dot product in$\mathbb{R}^d$
$A * B$	convolution of A and B
$\mathcal{H}^k$	$k-$ dimensional Hausdorff measure
$\eta^\perp$	orthogonal complement of a vector η
1_P	characteristic function of set P

Introduction

Motivation

In coating techniques such as thermal spraying, it is important to predict the dynamics of spreading of impinging particles [7]. Likewise, in the manufacturing of nanopatterned substrates, the precise control of the size and location of forming nanoparticles is essential to boost the functionality of the product [44]. These phenomena have the following features in common: Particles with anisotropic surface energy evolve on a substrate towards a shape with minimum surface energy. During the motion, particles may experience topological changes such as merging of two or more particles or splitting into several smaller parts. Understanding the interaction of a family of particles with anisotropic energies undergoing topological changes is essential to control the phenomena mentioned above. Similar problems appear in a number of other fields of applied science and engineering, such as cell biology or material science [69, 2, 71].

Formulation of the mathematical problem

To address the above phenomenon in mathematical terms, we consider a particle as a closed set P on a completely rigid substrate S surrounded by a vapour region V, see Figure i. Denoting Γ_{SP}, Γ_{SV} and Γ the interface between substrate–particle, substrate–vapor and particle–vapor regions, respectively, the total interfacial energy of this system is given by

$$E(\Gamma) = \int_{\Gamma} \gamma_{PV}\, ds + \int_{\Gamma_{SP}} \gamma_{SP}\, ds + \int_{\Gamma_{SV}} \gamma_{SV}\, ds, \tag{1}$$

where γ_{SP}, γ_{SV} and γ_{PV} signify the interface energies of the corresponding interfaces. There are several possible ways to model the evolution of such a particle towards a local minimum of the energy E. Here we adopt the most straightforward evolution law, namely the L^2-gradient flow. Since this flow does not preserve the enclosed volume, a constraint has to be imposed on the admissible function space. The resulting motion is then called the volume constrained *anisotropic mean curvature flow (AMCF)*. In general, it involves multiple phases, but in our model, the problem is simplified since one phase (the substrate) is fixed throughout the evolution. Still, it is necessary to handle the non-smoothness in the shape of the particle at the triple point where the three different phases meet.

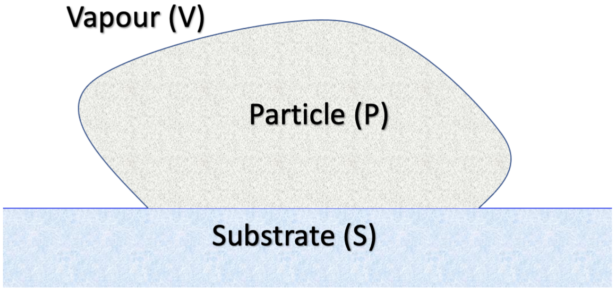

Figure i: Setup of the mathematical model of a particle evolving on a flat, rigid substrate.

Summary of mathematical methods and known results

The research on the simpler version of the problem, i.e., without obstacle and with constant interfacial energy γ_{PV}, has a long history. The total energy is then obtained by simply excluding the second and third terms in (1):

$$E(\Gamma) = \gamma_{PV} \int_{\Gamma} 1 \, dl, \tag{2}$$

and the corresponding L^2-gradient flow becomes the *mean curvature flow*.
In order to solve the flow equation, the interface Γ has to be represented in terms of a function. In the initial phases of analysis, explicit approaches were used, which included the graphical and parametric representation of the interface. Then the mean curvature flow leads to a system of nonlinear parabolic PDEs. In two dimensions, Gage et al. [37], and Grayson [42] proved the existence of a solution and its asymptotic convergence to a point, provided that the initial curve is smooth. In higher dimensions, the existence of solution was given by Huisken [45] with additional requirements on the initial surface, i.e., compactness and uniform convexity. The explicit approach is straightforward but cannot handle singularities in the evolution. For example, if the surface undergoes a topological change and splits into two disjoint parts, one function is no longer sufficient to describe them.

This led to considering the implicit method of interface representation. An important implicit method is the level set approach, which represents the interface as a level set of suitable function u. This approach leads to highly nonlinear, degenerate parabolic equations but allows for singularities; for example, pinch-off can be expressed by a smooth evolution of the level set function. To define the solution beyond singularities, several notions of weak solution were developed, one of the major examples being the theory of *viscosity solutions*. The existence and uniqueness of weak solution for level set based PDE is proved independently by Evans and Spruck [31] and Chen, Giga and Goto [17]. The above results were extended to volume constrained problems [68, 53] and to problems with orientation-dependent surface energy. From a mathematical perspective, there are two types of such anisotropies: smooth ones and crystalline, where equilibrium shape is a polytope. While the problem with smooth anisotropies tends to be a rather straightforward generalization of the isotropic problem [1], the lack of differentiability in the crystalline setting poses new challenges making it an active research area [50].

All of the above results describe the interface as a boundary of a single evolving set. Thus they cannot be used to address the multiphase problem where junctions, i.e., sets of points where three or more interfaces intersect, appear. The investigation of evolving triple junction started in Bronsard and Reitich [10] using theory of parabolic PDEs and was extended in several works [57, 52], but these results use the parametric approach and thus cannot handle topological changes. The first general result on the existence of MCF for networks was given by Kim and Tonegawa [49] in the framework of varifolds of geometric measure theory, resolving the question of possible triviality of the original Brakke's proof. Another important result from the viewpoint of this thesis is the convergence of a diffused approximation to this type of isotropic multiphase MCF given by Laux and Otto [55]. First results on the anisotropic multiphase problem appeared this year in [54], analyzing a tripod with smooth anisotropies and without singularities in the flow. The difficulty in dealing with the anisotropic case is the lack of uniform estimates and other basic tools, such as monotonicity formulas.

Obstacle problem: our contribution

The aim of this thesis is to deepen the understanding of the anisotropic multiphase problem in the setting allowing for topological changes, where rigorous mathematical analysis is still developing. As a starting point, numerical approximation of the problem is addressed. For the obstacle problem, the explicit approach was implemented by Wang et al. [70]. They use surface diffusion as the evolution law and implement a finite element scheme to investigate the resulting shapes of anisotropic particles. However, the explicit approach inherently cannot cope with possible topological changes unless their appear-

ance and nature are apriori known.
To resolve the question of topological changes, Xu et al. in [73] developed a numerical scheme based on the implicit approach. Namely, they solved the obstacle problem using level set approach, but their scheme pertains only to the isotropic energy case. The motivation of this work comes from the absence of methods for obstacle problems that could handle both anisotropic energies and topological changes.

To solve the obstacle problem with automatic handling of topological changes, we use the level set approach, which leads to a degenerate, non-linear PDE. We develop a thresholding method to solve this PDE in the case of obstacle problem. The thresholding method is based on a linearization of the original problem leading to an anisotropic diffusion problem, which can be solved by convolution of the characteristic function of a phase with a suitable convolution kernel. The original paper [59] introduces this method for isotropic two-phase problems where convolution is taken with the Gaussian kernel. The extension to the anisotropic case was theoretically addressed in [9, 25, 29], but systematical investigation of the numerical properties of the resulting kernels is still lacking.

We conclude the introduction by giving an outline of the thesis. Chapters 1 and 2 are dedicated to introduction to the problem and literature review. Chapter 1 presents isotropic two-phase problem, and Chapter 2 extend it to anisotropic energy—both chapters introduce the necessary background for the obstacle problem. Chapter 3 introduces the level set-based thresholding method to numerically solve governing PDEs of the flow. Chapter 4 survey the known convolution kernels and investigates their numerical properties. Finally, Chapter 5 constructs a new algorithm to solve the obstacle problem and analyzes its properties theoretically and numerically.

The first contribution of this work is a thorough investigation of convolution kernels through numerical comparison tests using different types of anisotropies, including crystalline ones. The objective is to assess the numerical behaviour of kernels in view of their application to multiphase or obstacle problems.

The second major contribution is the construction of a new thresholding algorithm for the numerical realization of multiphase anisotropic mean curvature flows. In particular, we rigorously prove the stability of the algorithm and study its numerical properties. This closes the gap between the works [70] and [73] and allows for simulations of obstacle problems involving topology changes, as demanded in applications. The results presented in chapters 4 and 5 of this thesis are based on the paper by S. Gavhale and K. Švadlenka [36].

Codes: All the codes generated during this research are available here and at the link https://github.com/siddharthgavhale/ThesisCodes

Chapter 1

Isotropic two-phase problem

We divide this chapter into two parts. The first part introduces the problem for isotropic energy without area constraint. We derive a mean curvature flow model for this specific energy and summarize known results on existence and properties of solutions. This leads to the topic of singularities. We present some examples and numerical results. In the second part, we add area constraint and follow the same content as in the first part.

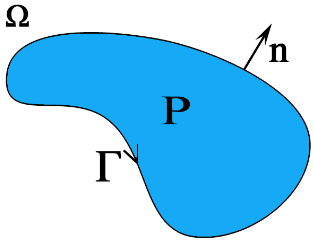

Figure 1.1: Single particle P with boundary Γ and outer normal $\boldsymbol{n}$

1.1 Isotropic energy without area constraint

1.1.1 Two-phase problem

Consider a free particle as a closed set $P \subset \mathbb{R}^2$ without substrate in a vapor, see Figure 1.1. The particle–vapor interface $\Gamma = \partial P$ has constant surface energy density $\gamma > 0$ and thus its surface energy can be written as

$$E(\Gamma) = \int_{\Gamma} \gamma \, dl. \tag{1.1}$$

We wish to investigate equilibrium shapes and L^2-gradient flow of the energy (1.1), also known as *mean curvature flow* (MCF). Without loss of generality we may set $\gamma = 1$. This choice of γ reduces the total energy (1.1) to

$$E(\Gamma) = \int_{\Gamma} 1 \, dl. \tag{1.2}$$

1.1.2 Mean curvature flow

We derive the evolution law for the L^2 gradient flow of the energy (1.2) starting from a smooth and closed curve

$$\Gamma(0) = \Gamma_0. \tag{1.3}$$

The flow is described by a one parameter family $\Gamma(t)$ of curves, where t represents time.

To derive the L^2 gradient flow of (1.2), we need the first varation of (1.2). To this end, consider arbitrary smooth function $\phi : \mathbb{R}^2 \longrightarrow \mathbb{R}^2$ and a perturbed curve $\Gamma_\epsilon = \{(x, y) + \epsilon\phi(x, y) \mid (x, y) \in \Gamma\}$. A calculation (see appendix A.3 for details) gives:

$$\frac{d}{d\epsilon} E(\Gamma_\epsilon)\Big|_{\epsilon=0} = \int_{\Gamma} \kappa \, (\boldsymbol{n} \cdot \phi) \;\; dl, \tag{1.4}$$

where $\boldsymbol{n}$ is the outer unit normal to interface Γ and κ is curvature. In two dimensions, curvature at $x \in \Gamma$ can be given as the inverse of the radius of the osculating circle at x. Next, consider the set of all possible normal velocities of Γ, i.e., $\mathcal{K}_\Gamma = \{V : \Gamma \to \mathbb{R} \mid V \in L^2(\Gamma)\}$ and a vector field $\phi : \mathbb{R}^2 \longrightarrow \mathbb{R}^2$ such that $V = \phi \cdot \boldsymbol{n}$ on Γ and take a perturbed curve as Γ_ϵ as above. Define L^2-inner product on $\mathcal{K}_\Gamma$ as,

$$\langle k_1, k_2 \rangle_{L^2} = \int_{\Gamma} k_1 k_2 \, dl \quad \text{for } \; k_1, k_2 \in \mathcal{K}_\Gamma.$$

The definition of the L^2-gradient ∇E of E and (1.4) give,

$$\langle \nabla E, V \rangle_{L^2} = \frac{d}{d\epsilon} E(\Gamma_\epsilon)\Big|_{\epsilon=0} = \int_{\Gamma} \kappa \, (\boldsymbol{n} \cdot \phi) \;\; dl = \int_{\Gamma} \kappa V \;\; dl \qquad \text{for all } V \in \mathcal{K}_\Gamma.$$

This leads to $\nabla E = \kappa$ and hence the L^2- gradient flow of the energy E is

$$V = -\kappa. \tag{1.5}$$

This equation represents mean curvature flow for isotropic surface energy, i.e., normal velocity is given by curvature. (1.5) is extended to higher dimension by replacing curvature by mean curvature. Here mean curvature is defined as the sum of principal curvatures. Detailed derivation of (1.5) in higher dimension is given in [22, 40].

1.1.3 Methods of representation of surfaces

In order to analyse mean curvature flow, there are several ways to represent an interface. Here, we focus on three approaches, namely, graphical, parametric, and level set approach.

Graphical representation

In the *graphical approach*, we assume that $\Gamma(t)$ can be written as a graph of suitable function:

$$\Gamma(t) = \{(x, u(x,t)) \mid x \in \Psi\},$$

where the function $u : \Psi \times [0, T) \to \mathbb{R}$ has to be found. Here $\Psi \subset \mathbb{R}^{d-1}$ is the projection onto a hyperplane of a domain Ω containing the curve. The unit normal is $\boldsymbol{n} = \frac{(\nabla u, -1)}{\sqrt{1+|\nabla u|^2}}$, thus curvature and velocity in normal direction are given as follows

$$\begin{aligned} \kappa(x, u(x,t)) &= \nabla \cdot \left(\frac{\nabla u(x,t)}{\sqrt{1 + |\nabla u(x,t)|^2}} \right), \qquad (x, u(x,t)) \in \Gamma(t), && (1.6) \\ V(x, u(x,t)) &= -\frac{u_t(x,t)}{\sqrt{1 + |\nabla u(x,t)|^2}}. && (1.7) \end{aligned}$$

Mean curvature flow (1.5) then reads

$$u_t(x,t) = \sqrt{1 + |\nabla u(x,t)|^2}\ \nabla \cdot \left(\frac{\nabla u(x,t)}{\sqrt{1 + |\nabla u(x,t)|^2}} \right), \quad \text{in } \Psi \times (0, T) \tag{1.8}$$

with suitable boundary condition and initial condition,

$$u(\cdot, 0) = u_0 \text{ in } \Psi. \tag{1.9}$$

Intuitively, graphical approach is the most straightforward one. It leads to a scalar nonlinear parabolic equation and directly computes the surface. However, this approach is largely restrictive since circumstances where the surface is not a graph appear often. Moreover, even if initial condition is a graph, it is possible that during evolution, it will not be a graph anymore. Further, if a curve is split into two or more parts, then graphical approach fails to handle such situations (so-called topological changes).

Parametric representation

In two dimensional *parametric approach*, an evolving interface $\Gamma(t)$ can be described by a smooth time-dependent vector function as follows:

$$\Gamma(t) = \{F(u,t) \mid F : S \times [0,T) \to \mathbb{R}^2\}$$

where $S = [0,1]$ is a fixed interval for the curve parameter. The unit tangential vector $\boldsymbol{t}$ is defined as $\boldsymbol{t} = \frac{\partial_u F}{|\partial_u F|}$, thus the unit normal vector $\boldsymbol{n}$ can be obtained by rotating the tangential vector by 90 degrees. Then the curvature κ is expressed as

$$\kappa = \boldsymbol{n}\,\frac{\partial_{uu}F}{|\partial_u F|^2}, \tag{1.10}$$

further, the normal velocity V is normal component of the time derivative of F

$$V = -\boldsymbol{n}\,\partial_t F. \tag{1.11}$$

With these normal velocity and curvature, the mean curvature flow (1.5) then reads

$$\partial_t F(u,t) = \frac{\partial_{uu}F(u,t)}{|\partial_u F(x,t)|^2}, \qquad (u,t) \in \Gamma(t) = F(u,t), \tag{1.12}$$

with periodic boundary condition and initial condition,

$$F(\cdot,0) \;\; = \;\; F_0. \tag{1.13}$$

The parametric approach can be extended to higher dimensions and requires solving $d+1$ parabolic equation in d space dimensions. Although it is more general than the graphical approach, being a direct approach, it still fails to handle topology changes.

Level set representation

The level set method was devised by S. Osher and J. A. Sethian in [62]. Later, several researchers worked on its mathematical analysis [31, 32, 33, 34, 37, 22]. We introduce level set method in general domain as follows:

Consider a domain $\Omega \subset \mathbb{R}^d$, which contains the initial surface. In the level set approach, $\Gamma(t)$ is represented as the 0-level set of a function $u \in C^{2,1}(\Omega \times [0,T))$, i.e.,

$$\Gamma(t) = \left\{ x \in \mathbb{R}^d | \; u(x,t) = 0 \right\}, \tag{1.14}$$

such that the gradient does not equal to zero on $\Gamma(t)$, i.e., $\nabla u(x,t) \neq 0$, where $x \in \Gamma(t)$. This representation of $\Gamma(t)$ leads to unit normal $\boldsymbol{n} = \pm \frac{\nabla u}{|\nabla u|}$. The sign depends on the choice of level set function, see Figure 1.2. All four plots represent a level set function of unit circle (in red colour), and show that outer normal is $\frac{\nabla u}{|\nabla u|}$ when level set function is chosen negative in the region enclosed by the curve. We use this setting in the sequel, thus curvature and velocity in normal direction are given as follows:

$$\kappa(x,t) \;=\; \nabla \cdot \left(\frac{\nabla u(x,t)}{|\nabla u(x,t)|} \right), \qquad (x,t) \in \Gamma, \tag{1.15}$$

$$V(x,t) \;=\; -\frac{u_t(x,t)}{|\nabla u(x,t)|}. \tag{1.16}$$

Mean curvature flow (1.5), along with (1.15) and (1.16) leads to the nonlinear parabolic partial differential equation

$$u_t(x,t) \;=\; |\nabla u(x,t)| \; \nabla \cdot \left(\frac{\nabla u(x,t)}{|\nabla u(x,t)|} \right), \quad \text{in } \Omega \times (0,T) \tag{1.17}$$

with suitable boundary condition and initial condition

$$u(\cdot,0) = u_0 \;\text{ in } \Omega. \tag{1.18}$$

Solution of (1.17) and (1.18) gives evolution of level sets of u by mean curvature flow.

Unlike the other approaches, level set method can handle topological changes automatically; since singularities in the evolution of a curve such as pinch off or merging can be described by a smooth evolution of corresponding level set function.

Level set approach increase the problem dimension by one, which is a drawback of this approach from the computational viewpoint. Note that the governing PDE is highly

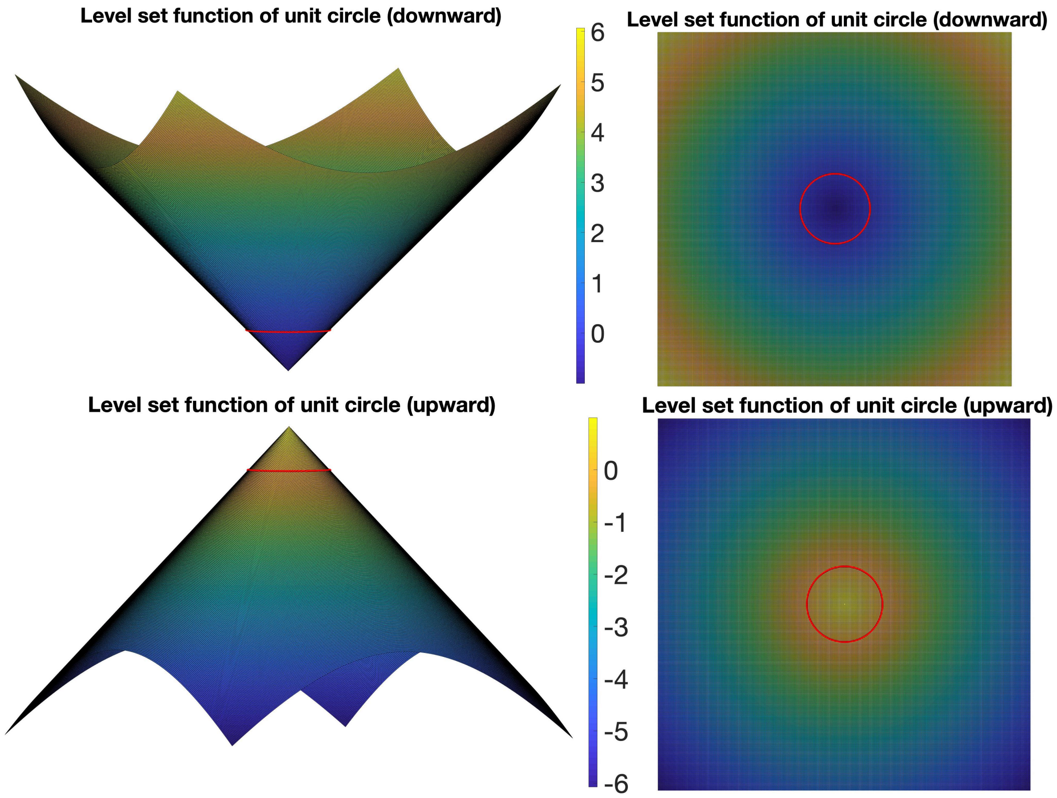

Figure 1.2: Level set function of unit circle: (top) normal with positive sign, (bottom) normal with negative sign.

nonlinear, degenerate, and singularities may occur during evolution. To obtain a solution beyond singularities, *viscosity solution framework* was developed by several researchers. The theory of viscosity solution is introduced by Crandall, Ishii and Lions in [20].

1.1.4 Existence of solution and properties

Gage et al [37] and Grayson [42] proved the existence of solution of the mean curvature flow, i.e., (1.5) for smooth initial condition (1.3) in the parametric setting. The following theorem states the existence of a solution and convergence of the curve to a point.

Theorem 1.1.1. *[22] If* $\Gamma_0 \subset \mathbb{R}^2$ *is a smooth embedded closed curve then smooth embedded solution of* (1.3) *and* (1.5) *exists on finite time interval* $[0, T^e)$*. Further, it shrinks to a point as time converges to* T^e*.*

Proof of this theorem is divided into two papers. Firstly, for a given convex Γ_0, Gage and Hamilton proved this outcome in [37]. After that, Grayson [42] proved that a smooth embedded closed curve remains smooth and embedded; moreover, it becomes convex in finite time.

The value T^e represents the extinction time of initial curve, i.e., the time when curve disappears. For higher dimension, existence of solution of MCF is given by Huisken [45] with additional requirement on initial surface as mentioned in following theorem,

Theorem 1.1.2. *[45] Let $d \geqslant 3$ and assume that $\Gamma_0 \subset \mathbb{R}^3$ is a smooth, compact and uniformly convex hypersurface. Then* (1.3) *and* (1.5) *have a smooth solution on a finite time interval $[0, T^e)$ and $\Gamma(t)$ converge to a point as time converges to T^e.*

The above theorem guarantees the solution of (1.3) and (1.5) provided that, the initial surface is convex, smooth and compact. For non-convex initial surfaces, the statement is not valid. For example, consider a dumbell shape in three dimensions as shown in Figure 1.3. Evolution of this surface by MCF develops a pinch-off singularity before it shrinks to two points [43], see right side of figure Figure 1.3.

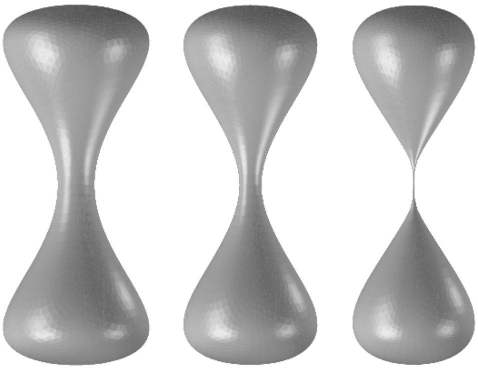

Figure 1.3: Evolution of dumbbell shape by mean curvature flow and singularity occurrence . This picture is taken from [22].

The above results hold only until singularities occur. Therefore, one need to consider the formulation of MCF in the form of (1.17). Note that (1.17) is a degenerate, nonlinear parabolic and not defined where the gradient of u vanishes; leading to failure of standard methods. Therefore, [17] and [31] independently develop existence and uniqueness theory for (1.17) and (1.18) within the framework of *viscosity solutions*. Deckelnick et al. [22] summarize the result of [17] and [31] in the following theorem:

Theorem 1.1.3. *[22] Assume $u_0 : \mathbb{R}^{d+1} \to \mathbb{R}$, which satisfy*

$$u_0(x) = 1, \qquad \textit{for } |x| \geqslant S,$$

for some $S > 0$. Then there exists a unique viscosity solution of (1.17) *and* (1.18)*, such that*

$$u(x,t) = 1, \qquad \textit{for } |x| + t > R,$$

for some $R > 0$ depending only on S.

We summarize basic properties of mean curvature flow. In two dimensions, any closed curve evolving under mean curvature flow becomes smooth and convex in finite time; further convex curve converges to a point in finite time. During the evolution by MCF, curve acquires a circular shape along with reducing the total area enclosed by the curve [37, 42]. MCF leads to parabolic partial differential equations for the function describing the shape of curve, i.e., normal velocity leads to time derivative and mean curvature leads to two spatial derivatives. Since second-order parabolic partial differential equations fulfil *maximum and comparison principles*, one can show that if one surface is contained in an other surface and both surfaces start evolving under mean curvature flow, then this situation remains the same throughout all time [27].

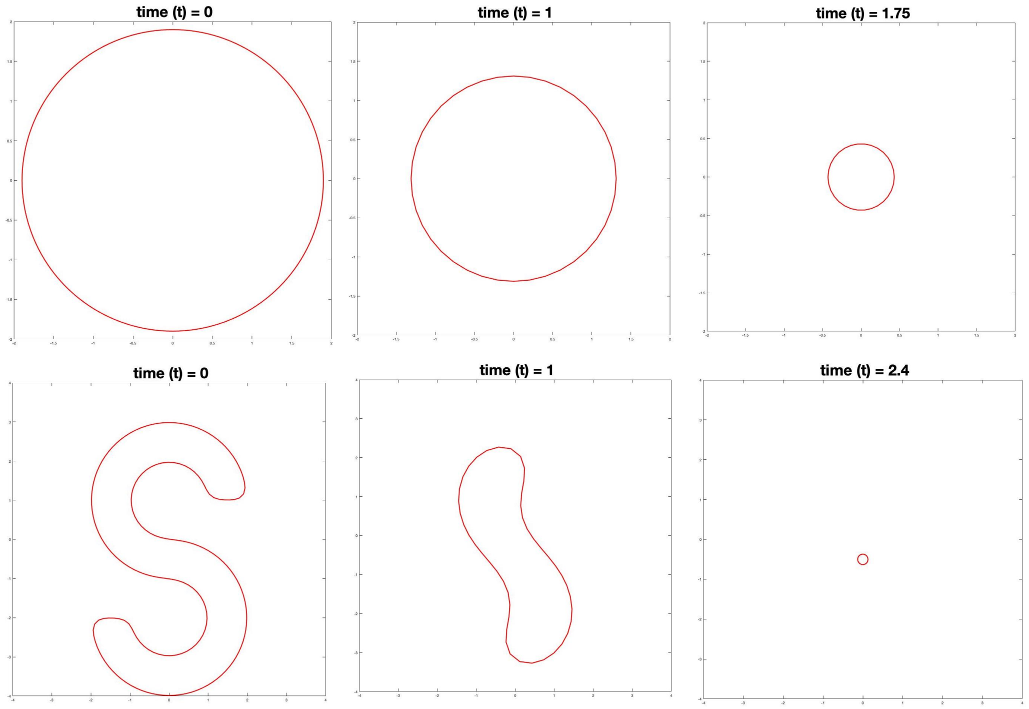

Figure 1.4: Evolution of closed curve by mean curvature flow. Results are obtained by thresholding method.

1.1.5 Examples

To demonstrate motion by mean curvature, we consider $\gamma = 1$ along with two different initial closed curves, i.e., circle as an example of convex curve and smooth S shape as example of a non-convex one, see Figure. 1.4. Both these curves converge to a point. In the case of a circle, this flow is self-similar, i.e., the curve is a circle at every time, only its radius decreases. S shape evolution is an example demonstrating the result, mentioned in theorem 1.1.1, i.e., smooth embedded closed curve becomes convex in finite time, and then it converges to a point.

1.1.6 Numerical methods

In this section, we outline basic numerical methods to solve the governing PDEs of evolution problem derived by parametric and level set approach in Section 1.1.3. We use a specific example of a shrinking circle for simple explanation. For a given circle Γ_0 with radius r_0, we are interested in finding a family of circular closed curves,

$$\Gamma(t) = \{(r(t)\cos\theta, r(t)\sin\theta) \mid \theta \in [0, 2\pi)\},$$

which is evolved by (1.5). Here $r(t)$ is the radius of the circle at time t, and $r(0) = r_0$.

Analytical solution

In this subsection, we derive analytical solution for the shrinking circle problem. Note that the normal velocity is given as $V = r^{'}(t)$ at every point and the curvature is inverse of the radius of osculating circle; therefore, in this case $\kappa = \frac{1}{r(t)}$. (1.5) then leads to the simple ODE $r^{'}(t) = -\frac{1}{r(t)}$. Solution of this ODE is $r(t) = \sqrt{r_0^2 - 2t}$, where $t \in [0, \frac{r_0^2}{2})$. Note that the extinction time $T^e = \frac{r_0^2}{2}$ and $\Gamma(t)$ shrinks to a point as t converges to T^e.

Front tracking method

In front tracking approach, we discretize initial surface into finite set of discrete points, calculate a discrete approximation of mean curvature at each point, and then move each point of the discretized surface by (1.5), until we reach singularity. During evolution, one can notice saturation of discretized points in regions of high curvature, so to avoid error accumulation, redistribution of points becomes essential. In Appendix A.6 we summarize one such known redistribution method for two-dimensional curves.

In shrinking circle problem, initial circle shrinks without changing shape; therefore, we do not need to worry about redistribution of points. For demonstration purpose, we start with a circle of radius two and $\gamma = 1$. The outcome of front tracking method is shown in Figure 1.5. The left plot shows the evolution of the circle at equal time intervals. We use 32 points to describe initial circle, and all those points are visible in the plot. The right side plot shows the analytical and numerical decrease in radius. According to analytical solution (black line), the circle should vanish at time $t = 2$, but front tracking solution moves slightly slower. One can reduce the error by using more points to discretize the initial condition.

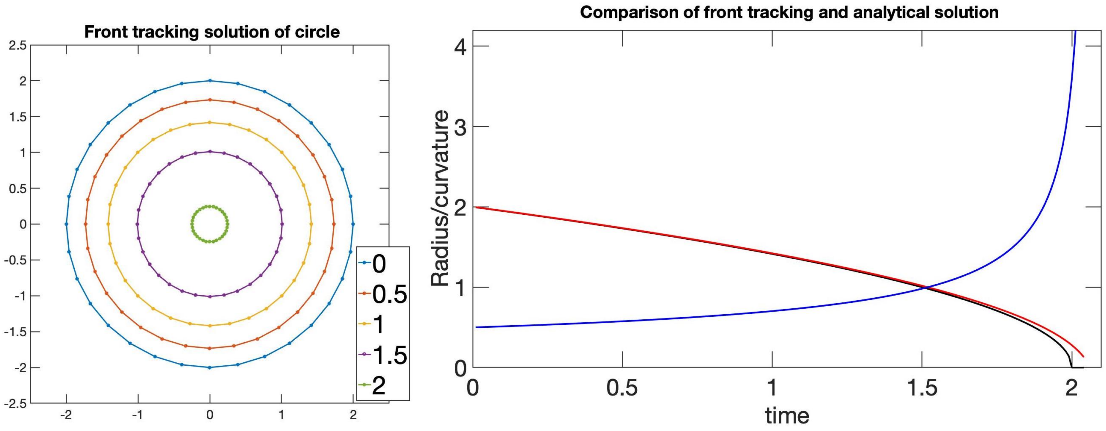

Figure 1.5: Mean curvature flow starting from circle. Results are obtained by front tracking approach. Left: Evolution of circle at equal time intervals. Right: Radius (red) and curvature (blue) at each time obtain by front tracking approach. Analytical radius is shown in black colour.

Numerical methods to solve level set based PDEs

There are several numerical methods available to solve the governing equation obtained by level set approach. One can think about direct methods, e.g., finite difference or finite element method. F. Catte, et al. in [13] and A. Oberman in [61] proposed finite difference schemes for the isotropic mean curvature motion PDE obtained by level set approach. Their scheme is monotone and convergent, but it is still hard to solve because it requires solving a system of non-linear equations.

Therefore, we use a more simple and easy to implement numerical method, namely, the thresholding method, that was first introduced in [59]. Details of the thresholding method are given in Chapter 3, together with several numerical tests. For demonstration purpose, we show two results obtained by thresholding method in Figure 1.4.

1.2 Isotropic energy with area constraint

Mean curvature flow does not preserve area A enclosed by the initial curve. Indeed, the derivative of area with respect to time is negative, i.e., $\frac{dA}{dt} \leqslant 0$ [37, 42]. Therefore, as a natural extension of the problem defined in Section 1.1, we consider a two-phase isotropic problem with area constraint. The setup for this problem is the same as in Section 1.1, except that we consider gradient flow in the set of curves with a given enclosed area. Note that the area enclosed by the closed curve Γ is given by

$$A = \frac{1}{2}\int_{\Gamma} (x, y) \cdot \boldsymbol{n}\, dl. \tag{1.19}$$

Suppose A_0 is the area of initial closed curve Γ_0. Since we are interested in minimum energy under area constraint, we use Lagrange multiplier method. Then the extended energy of this system is

$$\begin{aligned} E_\lambda(\Gamma) &= \int_{\Gamma} 1\, dl + \lambda\frac{1}{2}\int_{\Gamma} (x, y) \cdot \boldsymbol{n}\, dl \\ &= \int_{\Gamma} 1\, dl + \lambda\frac{1}{2}\int_{b}^{a} (g_1 g_2' - g_1' g_2)\, ds, \end{aligned} \tag{1.20}$$

where $\Gamma = \{g(s) = (g_1(s), g_2(s)) \mid s \in [a, b)\}$ and $g : [a, b] \to \mathbb{R}^2$ is differentiable and $g(a) = g(b)$.

1.2.1 Area preserving mean curvature flow

To derive the governing equation of area preserving mean curvature flow, we need the first variation of (1.20). Split E_λ into two part as follows,

$$E_1(\Gamma) = \int_{\Gamma} 1\, dl \quad \text{and} \quad E_2(\Gamma) = \lambda\frac{1}{2}\int_{b}^{a} (g_1 g_2' - g_1' g_2)\, ds.$$

First variation of $E_1(\Gamma)$ has been derived already in Section 1.1. Thus we are left with variation of $E_2(\Gamma)$, for which we use the same test unction ϕ as in the problem without area constraint. Then we have

$$\begin{aligned}
\frac{d}{d\epsilon}E_2(\Gamma_\epsilon)\Big|_{\epsilon=0} &= \lim_{\epsilon\to 0}\frac{\lambda}{2\epsilon}\int_b^a \Big[(g_1+\epsilon\phi_1)(g_2+\epsilon\phi_2)' - (g_1+\epsilon\phi_1)'(g_2+\epsilon\phi_2) \\
&\qquad -(g_1g_2' - g_1'g_2)\Big]ds \\
&= \lim_{\epsilon\to 0}\frac{\lambda}{2\epsilon}\int_b^a \left[\epsilon(g_1\phi_2' + g_2'\phi_1 - g_1'\phi_2 - g_2\phi_1') + \epsilon^2(\phi_1\phi_2' - \phi_1'\phi_2)\right]\, ds \\
&= \frac{\lambda}{2}\int_b^a \left[g_1\phi_2' + g_2'\phi_1 - g_1'\phi_2 - g_2\phi_1'\right]\, ds \\
&= \frac{\lambda}{2}\int_b^a \left[-g_1'\phi_2 + g_2'\phi_1 - g_1'\phi_2 + g_2'\phi_1\right]\, ds \qquad \text{integration by parts} \\
&= \lambda\int_b^a (g_2', -g_1')\cdot(\phi_1,\phi_2)\, ds \\
&= \lambda\int_b^a \frac{(g_2', -g_1')}{|g'|}\cdot(\phi_1,\phi_2)\,|g'|\, ds \\
&= \lambda\int_\Gamma -\boldsymbol{n}\cdot\phi\, dl. \qquad (1.21)
\end{aligned}$$

The above result along with (1.4) allows us to write

$$\begin{aligned}
\frac{d}{d\epsilon}E_\lambda(\Gamma_\epsilon)\Big|_{\epsilon=0} &= \frac{d}{d\epsilon}E_1(\Gamma_\epsilon)\Big|_{\epsilon=0} + \frac{d}{d\epsilon}E_2(\Gamma_\epsilon)\Big|_{\epsilon=0} \\
&= \int_\Gamma \kappa\,(\boldsymbol{n}\cdot\phi)\ \ dl - \int_\Gamma \lambda(\boldsymbol{n}\cdot\phi)\, dl \\
&= \int_\Gamma (\kappa-\lambda)(\boldsymbol{n}\cdot\phi)\, dl. \qquad (1.22)
\end{aligned}$$

To obtain equation of area preserving mean curvature flow we repeat the procedure leading to (1.5), and obtain the following form of area-preserving mean curvature flow,

$$V = -\kappa + \lambda. \qquad (1.23)$$

To find the exact value of Langrage multiplier λ, we utilise area preservation condition, i.e.,

$$\frac{dA(t)}{dt} = 0, \quad \text{where } A(t) = \frac{1}{2}\int_{\Gamma(t)} (x,y)\cdot\boldsymbol{n}\, dl.$$

$$
\begin{align*}
2\frac{dA}{dt} &= \frac{d}{dt}\int_{\Gamma(t)} (x,y)\cdot \boldsymbol{n}\, dl \\
&= -\frac{d}{dt}\int_a^b (g_1(s,t), g_2(s,t))\cdot\left(\frac{\partial g_2(s,t)}{\partial s}, \frac{-\partial g_1(s,t)}{\partial s}\right)\, ds \\
&= -\int_a^b \left[(g_1,g_2)\cdot\left(\frac{\partial^2 g_2}{\partial t\partial s}, \frac{-\partial^2 g_1}{\partial t\partial s}\right) + \left(\frac{\partial g_1}{\partial t}, \frac{\partial g_2}{\partial t}\right)\cdot\left(\frac{\partial g_2}{\partial s}, \frac{-\partial g_1}{\partial s}\right)\right]\, ds \\
&= -\int_a^b g_1\frac{\partial^2 g_2}{\partial t\partial s} - g_2\frac{\partial^2 g_1}{\partial t\partial s}\, ds + \int_\Gamma g_t\cdot\boldsymbol{n}\, dl \\
&= -\left. g_1\frac{\partial g_2}{\partial t}\right|_a^b + \int_a^b \frac{\partial g_1}{\partial s}\frac{\partial g_2}{\partial t}\, ds + \left. g_2\frac{\partial g_1}{\partial t}\right|_a^b - \int_a^b \frac{\partial g_2}{\partial s}\frac{\partial g_1}{\partial t}\, ds + \int_\Gamma g_t\cdot\boldsymbol{n}\, dl \\
&= -\int_a^b \left(\frac{\partial g_2}{\partial s}\frac{\partial g_1}{\partial t} - \frac{\partial g_1}{\partial s}\frac{\partial g_2}{\partial t}\right)\, ds + \int_\Gamma g_t\cdot\boldsymbol{n}\, dl \\
&= -\int_a^b \left(\frac{\partial g_1}{\partial t}, \frac{\partial g_2}{\partial t}\right)\cdot\left(\frac{\partial g_2}{\partial s}, \frac{-\partial g_1}{\partial s}\right)\, ds + \int_\Gamma g_t\cdot\boldsymbol{n}\, dl \\
&= 2\int_\Gamma g_t\cdot\boldsymbol{n}\, dl \\
&= 2\int_\Gamma V\, dl \qquad\qquad \text{by (1.23)} \tag{1.24} \\
&= 2\int_\Gamma (\kappa-\lambda)\, dl \\
&= 2\int_\Gamma \kappa\, dl\, - 2\lambda\int_g 1\, dl \tag{1.25}
\end{align*}
$$

$\frac{dA(t)}{dt} = 0$ then yields $\lambda = \frac{\int_\Gamma \kappa\, dl}{\int_\Gamma 1\, dl}$. Note that λ is the avarage mean curvature along the curve, we denote it by κ_{avg}. This concludes the form of area preserving mean curvature flow as,

$$V = -\kappa + \kappa_{\text{avg}}. \tag{1.26}$$

This equation represents are-preserving mean curvature flow for isotropic surface energy, i.e., normal velocity is given by the difference of curvature and average curvature. (1.26) can be extended to higher dimensions by changing curvature to mean curvature; there, it is known as volume-preserving MCF. Detailed derivation of (1.26) in higher dimension is given in [38].

1.2.2 Existence of solution and properties

Gage [38] provided solution for (1.26) in two-dimensional case. Existence of solution for area preserving mean curvature flow, i.e., (1.26) along with initial condition (1.3), for general dimension, is given in [46]:

Theorem 1.2.1. *[46] If the initial hypersurface $\Gamma_0 \subset \mathbb{R}^d$ is uniformly convex then the evolution equation* (1.26) *has a smooth solution $\Gamma(t)$ for all times $0 \leqslant t < \infty$ and $\Gamma(t)$'s converge to a round sphere enclosing the same volume as Γ_0 in the C^∞-topology as $t \to \infty$.*

The above theorem yields existence of global solution to area-preserving mean curvature flow. Further, the author of [46] showed that solution converges exponentially fast to a sphere provided the initial surface is uniformly convex and smooth.

For non-convex initial shapes, Theorem 1.2.1 does not tell anything. Escher and Simonett fill this gap in [26]. Authors of [26] proved the existence of a local solution to area-preserving mean curvature flow (in their paper, they called it averaged mean curvature flow) starting from non-convex initial hypersurfaces. Note that authors assume initial surface Γ_0 to be a compact, closed, connected, embedded hypersurface in $\mathbb{R}^d$ of class $C^{1+\beta}$. Further, they proved following corollary:

Corollary 1.2.2. *[26] Convexity is not necessary for global existence of the averaged mean curvature flow. More precisely, there are non-convex hypersurfaces Γ_0 such that the solution of averaged mean curvature flow with initial condition Γ_0 exists globally and converges exponentially fast to a sphere.*

During the evolution, singularities in the form of self-intersection of surface may occur; this fact precludes the existence of a global solution for all non-convex bodies. Elliott and Garcke provide an example in [24]. The existence of a global distributional solution is given by Mugnai et al. [53], authors adopt a variational approach to accomplish the task. Later, Takasao [68] proved the existence of a weak solution for volume-preserving mean curvature flow using the phase-field approach. His result ensures the solution beyond the singularities.

1.2.3 Examples

For demonstration, consider $\gamma = 1$ and two different initial curves, i.e., rectangle and an irregular shape, as shown in Figure 1.6. Black lines represent initial shape; on the other hand, red represent final shape in both plots. Blue lines are intermediate curves during evolution. For rectangular intial shape, blue lines are shown at equal time intervals. In both cases, the enclosed area is preserved, and initial curves converge to a circle, as stated in Theorem 1.2.1.

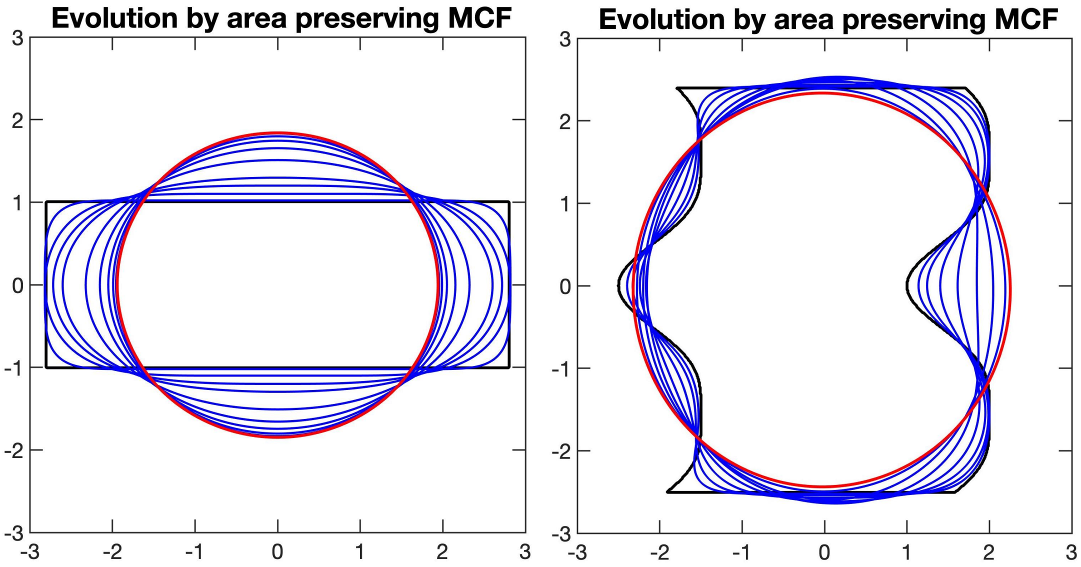

Figure 1.6: Evolution of closed curve by area preserving mean curvature flow. Results are obtained by thresholding method.

1.2.4 Numerical methods

Front tracking

Parametric approach can be solved numerically by front tracking method introduced in Section 1.1.6. The only difference is in the average curvature term, i.e., κ_{avg}. Note that discrete average curvature is nothing but a weighted sum of discrete curvatures at all discrete points.

Level set approach

Similarly to the problem without area-preservation, we can use direct methods to solve governing PDE. These approaches are difficult, as explained in Section 1.1.6. Therefore, to solve the governing PDEs numerically, we use the thresholding method mentioned in Section 1.1.6, with a modification to preserve the enclosed area. Details of thresholding method for area-preserving problem are given in Chapter 3. Here we only present an example of numerical simulation, see Figure 1.6.

Chapter 2

Anisotropic two-phase problem

In this chapter, we introduce the notion of anisotropy. We derive a mathematical model of anisotropic mean curvature flow in both the area-constrained and unconstrainted settings. Further, we summarize results regarding existence of solution and present several exmples.

2.1 Definition and classification of anisotropies

To describe surfaces with direction-dependent surface energy, we introduce the anisotropy function $\gamma : \mathbb{S}^{d-1} \to \mathbb{R}$. It is essentially defined for unit vectors, but for upcoming analysis, it is convenient to have it defined on the whole $\mathbb{R}^d$.

Therefore, throughout this work, we assume γ is 1-homogeneously extended to $\gamma : \mathbb{R}^d \longrightarrow [0, \infty)$ through

$$\gamma(x) = |x|\gamma\left(\frac{x}{|x|}\right), \qquad x \neq 0.$$

To ensure well-posedness of the two-phase energy, we assume γ is a convex function on $\mathbb{R}^d$. We now give definitions of some essential terminologies, i.e., unit ball, Wulff shape and Wulff envelope.

Definition 2.1.1. *For a given anisotropy γ, Frank diagram $\mathcal{F}_\gamma$ is defined as follows:*

$$\mathcal{F}_\gamma = \{p \in \mathbb{R}^d \mid \gamma(p) \leqslant 1\}. \tag{2.1}$$

Frank diagram is also known as γ-*unit ball* and denoted by B_γ . Note that it is a closed set. We denote its boundary by ∂B_γ. Several examples of Frank diagram are shown in

Figure 2.1

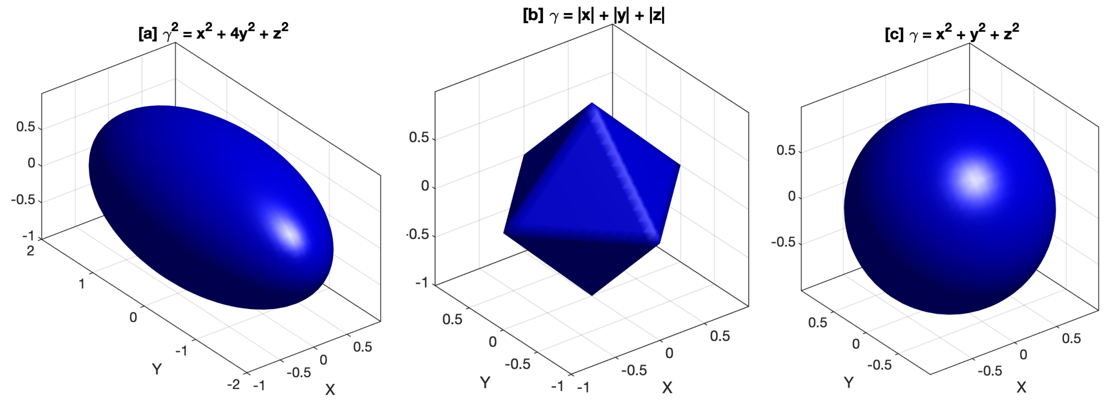
[a] $\gamma^2 = x^2 + 4y^2 + z^2$
[b] γ = |x| + |y| + |z|
[c] $\gamma = x^2 + y^2 + z^2$
Y
X
Y
X
Y
X

Figure 2.1: Examples of Frank diagram

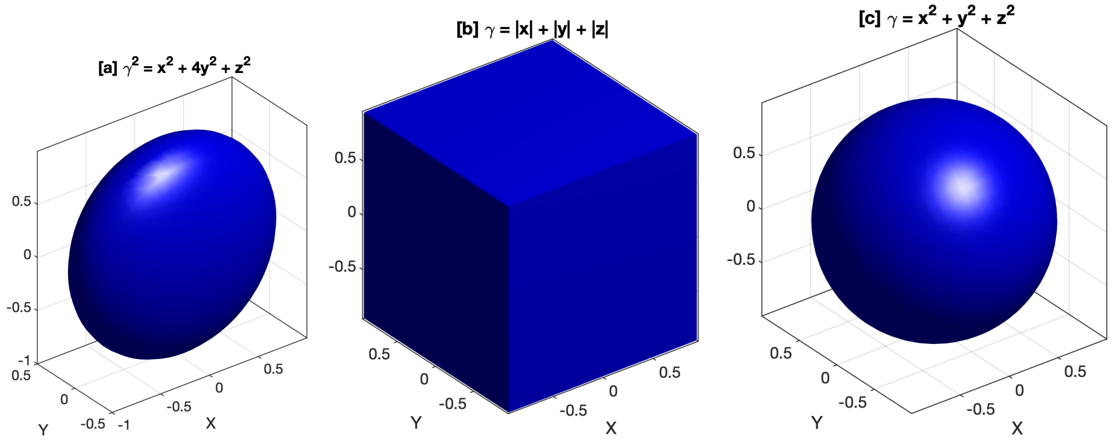
[a] $\gamma^2 = x^2 + 4y^2 + z^2$
[b] γ = |x| + |y| + |z|
[c] $\gamma = x^2 + y^2 + z^2$
Y
X
Y
X
Y
X

Figure 2.2: Examples of Wulff shape

For the next definition, we define the dual γ^o of γ as follows,

$$\gamma^o(\xi^o) = \sup_{\xi \in B_\gamma} \langle \xi^o, \xi \rangle,$$

where $\langle \cdot\, , \cdot \rangle$ denotes the inner product in $\mathbb{R}^d$.

Definition 2.1.2. *For a given anisotropy γ, if γ^o is the dual of γ, then the Wulff shape $\mathcal{W}_\gamma$ is defined as follows:*

$$\mathcal{W}_\gamma = \{\xi^o \in \mathbb{R}^d \mid \gamma^o(\xi^o) \leqslant 1\}.$$

It is hard to imagine the structure of Wulff shape from the above definition even for simple anisotropies. Therefore, we describe another method to construct Wulff shape in Appendix A.1. In Figure 2.2, we show several examples of Wulff shapes corresponding to anisotropies from Figure 2.1.

For next definition consider the unit outer normal $\boldsymbol{n}(x)$ at a point $x \in \Gamma$. Since the normal $\boldsymbol{n}$ is uniquely identified as $(\cos\theta, \sin\theta)$, where $\theta \in [-\pi, \pi)$ is the angle between $\boldsymbol{n}$ and the positive direction of y-axis measured clockwise from the y-axis, the function γ can be considered as a function of one variable θ, namely, $\gamma(\boldsymbol{n}(x)) = \gamma(\cos\theta(x), \sin\theta(x)) =: \tilde{\gamma}(\theta(x))$. In the subsequent text we will omit the tilde for simplicity.

Definition 2.1.3. *In two dimensions, Wulff envelope $\mathcal{W}^e_\gamma$ corresponding to anisotropy γ is the parametrized curve [12]:*

$$x(\theta) = -\gamma(\theta)\sin\theta - \gamma'(\theta)\cos\theta, \qquad y(\theta) = \gamma(\theta)\cos\theta - \gamma'(\theta)\sin\theta. \tag{2.2}$$

Denoting the boundary of Wulff shape by $\partial\mathcal{W}_\gamma$, we have $\partial\mathcal{W}_\gamma \subset \mathcal{W}^e_\gamma$. In Figure 2.3, blue colour shows Wulff shape and red curve represents Wulff envelope (2.2) for various anisotropies. Note that boundary of Wulff shape and Wulff envelope are identical for left and middle anisotropy in Figure 2.3, whereas, third anisotropy's Wulff boundary and Wulff envelope are not the same.

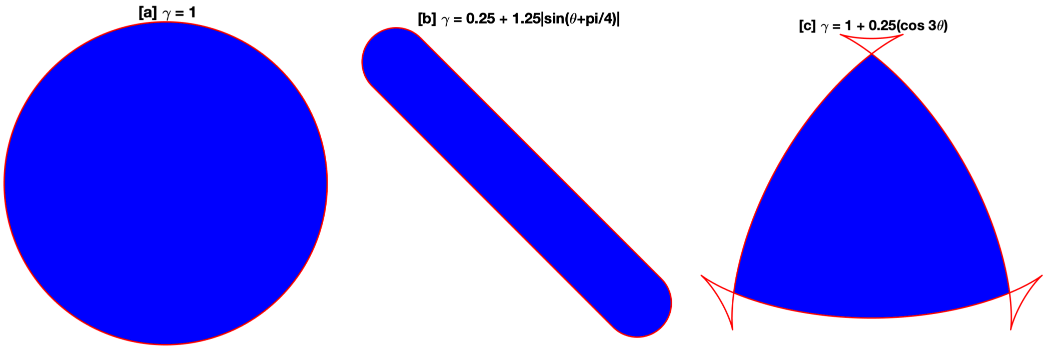

Figure 2.3: Difference between Wulff shape (blue) and Wulff envelope (red)

2.1.1 Classification of anisotropies

Smooth anisotropies $\gamma \in C^2$ are conventionally classified on the basis of the sign of surface stiffness, i.e., the quantity $\gamma(\theta) + \gamma''(\theta)$, as follows:

(A) *isotropic* : $\gamma =$ positive constant,

(B) *weakly anisotropic*: $\gamma(\theta) + \gamma''(\theta) > 0$ for all θ,

(C) *strongly anisotropic*: there is θ such that $\gamma(\theta) + \gamma''(\theta) \leqslant 0$, In isotropic case, as shown in Figure 2.3 [a], Wulff envelope is a circle whose radius is dependent on the magnitude of anisotropy γ. Notice that the isotropic case is a particular case of weak anisotropy. Wulff envelopes of weak anisotropies are identical to the boundary of Wulff shape [12], see Figure 2.3 [a,b]. On the other hand, strong anisotropies form *ears* by the Wulff envelope's self-intersection, see Figure 2.3 [c]. The outer part of these *ears* possesses negative surface stiffness, see Figure 2.4 , which shows the Wulff envelope for the anisotropy $\gamma = 1 + 0.2 \cos 5\theta$. Here red parts have negative surface stiffness. Numerous examples of anisotropies from literature [22, 9, 25, 30, 64] are gathered in Appendix A.4.

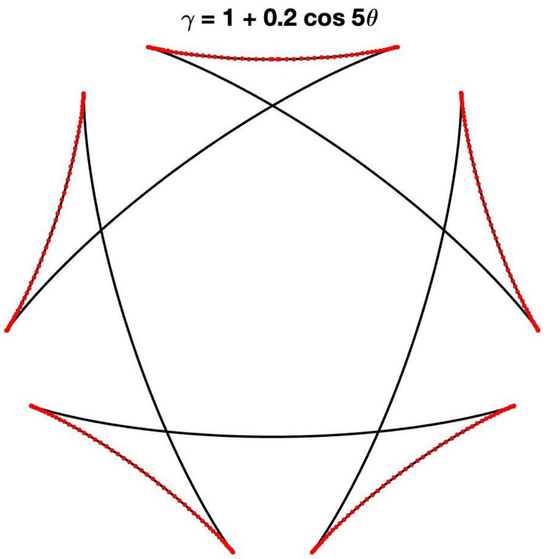

Figure 2.4: Wulff envelope of the strong anisotropy $\gamma = 1 + 0.2 \cos 5\theta$. Red colour shows regions with negative surface stiffness.

2.2 Anisotropic mean curvature flow

To introduce anisotropic mean curvature flow, we consider a simple two-phase evolution problem described below.

2.2.1 Two-phase problem

Consider a free particle as a closed set $P \subset \mathbb{R}^2$ without substrate in a vapor, see Figure 1.1. The particle–vapor interface $\Gamma = \partial P$ has general orientation-dependent energy (anisotropy) $\gamma : \mathbb{R}^2 \longrightarrow [0, \infty)$, i.e., $\gamma = \gamma(\boldsymbol{n}(x))$, where $\boldsymbol{n}(x)$ is the unit outer normal to P at a point $x \in \Gamma$. Hence the total interfacial energy of the particle reads

$$E(\Gamma) = \int_{\Gamma} \gamma(\boldsymbol{n})\, dl. \tag{2.3}$$

We wish to investigate equilibrium shapes and L^2-gradient flow of the energy (2.3), also known as *weighted mean curvature flow* (MCF).

One observes that (2.3) is a generalization of the isotropic energy, which is discussed in the previous chapter. 1-homogeneity and convexity of γ yields closed, convex and centrally symmetric B_γ. The strong convexity of B_γ is equivalent to the condition $\gamma^{''}(\theta)+\gamma(\theta) > 0$ for all θ, the proof of this statement is given in the following subsection.

Strong convexity of unit ball implies positive surface stiffness

Any $\xi \in \mathbb{R}^2$ can be written as $\xi = (r\cos\theta, r\sin\theta)$, where $r > 0, \theta \in [0, 2\pi)$. Note that B_γ is a level set of γ, moreover γ is one homogeneous. Using this property, we prove the following lemma.

Lemma 2.2.1. *$\xi \in \partial B_\gamma$ if and only if $r = \frac{1}{\gamma(\cos\theta, \sin\theta)} = \frac{1}{\gamma(\theta)}$.*

Proof. The statement readily follows using the 1- homogeneity property of γ. □

Lemma 2.2.2. *B_γ is strictly convex if and only if $\gamma^{''}(\theta) + \gamma(\theta) > 0, \forall\theta \in [0, 2\pi)$.*

Proof. ($\Rightarrow$) Let B_γ be a strictly convex set. Hence, the curvature of ∂B_γ is positive at all $\xi \in B_\gamma$. Consider polar form of $\xi = (\xi_1, \xi_2) = (r\cos\theta, r\sin\theta)$. The curvature κ is given by $\kappa = \frac{(\xi_1^{'}\xi_2^{''} - \xi_1^{''}\xi_2^{'})}{\sqrt[3]{(\xi_1^{'})^2 + (\xi_2^{'})^2}}$. Since curvature is positive, we deduce $\xi_1^{'}\xi_2^{''} - \xi_1^{''}\xi_2^{'} > 0$, which leads to

$$r^2 - rr'' + 2r'^2 > 0 \tag{2.4}$$

We know from Lemma 2.2.1 that $r = 1/\gamma(\theta)$; therefore, $r^{'} = \frac{-\gamma^{'}}{\gamma^2}$ and $r^{''} = \frac{2(\gamma^{'})^2}{\gamma^3} - \frac{\gamma^{''}}{\gamma^2}$. Plugging these values into (2.4) leads to the desired inequality, i.e., $\gamma^{''}(\theta) + \gamma(\theta) > 0$.

($\Leftarrow$) We prove this part by contradiction. Assume that the B_γ is not a convex set, then there exist at least one $\tilde{\xi} \in \partial B_\gamma$, which possesses negative curvature. Consider polar form of $\tilde{\xi} = (\tilde{\xi}_1, \tilde{\xi}_2) = (r\cos\tilde{\theta}, r\sin\tilde{\theta})$, where $\tilde{\theta}$ possesses at least one value in $[0, 2\pi)$. . The curvature κ is negative, we deduce $\tilde{\xi}_1^{'}\tilde{\xi}_2^{''} - \tilde{\xi}_1^{''}\tilde{\xi}_2^{'} < 0$, which leads to

$$r^2 - rr'' + 2r'^2 < 0. \tag{2.5}$$

Here, the setting is same as first part of this proof; therefore, we can use values of r and its derivatives to get final form of (2.5), i.e., $\gamma''(\tilde{\theta}) + \gamma(\tilde{\theta}) < 0$. □

2.2.2 Anisotropic mean curvature flow

We define anisotropic mean curvature by κ_γ by

$$\kappa_\gamma(x) = \nabla_\Gamma \cdot \boldsymbol{n}_\gamma(x), \qquad x \in \Gamma, \tag{2.6}$$

where $\boldsymbol{n}_\gamma$ denotes the Cahn-Hoffman vector on Γ, i.e.,

$$\boldsymbol{n}_\gamma(x) = \nabla\gamma(\boldsymbol{n}(x)), \qquad x \in \Gamma, \tag{2.7}$$

and the tangential gradient $\nabla_\Gamma \eta$ of a function η , which is differentiable in an open neighbourhood of Γ, is defined by

$$\nabla_\Gamma \eta = \nabla\eta - (\nabla\eta \cdot \boldsymbol{n})\, \boldsymbol{n}. \tag{2.8}$$

To derive the L^2 gradient flow of (2.3), i.e., anisotropic mean curvature flow, we need first varation of (2.3), which is derived in [22] using suitable perturbation function ϕ. Lemma 8.2 in [22] gives the following first variation:

$$\frac{d}{d\epsilon}E(\Gamma_\epsilon)\Big|_{\epsilon=0} = \int_\Gamma \kappa_\gamma(\boldsymbol{n}\cdot\phi)\, dl. \tag{2.9}$$

Definition of L^2 inner product and (2.9) lead to the following form of anisotropic mean curvature flow,

$$V = -\kappa_\gamma. \tag{2.10}$$

(2.10) is extended to higher dimensions by replacing anisotropic curvature with anisotropic mean curvature. Detailed derivation for higher dimension is presented in [22].

In the upcoming chapters, we focus on the general form of (2.10). It is known as weighted anisotropic mean curvature flow, and it is given by,

$$V = -\mu\kappa_\gamma, \tag{2.11}$$

where $\mu : \mathbb{R}^2 \to \mathbb{R}_+$ is called *mobility*. One can obtain (2.11) as the gradient flow corresponding to the inner product

$$\langle k_1, k_2 \rangle_\mu = \int_\Gamma \mu(\boldsymbol{n}) k_1 k_2 \, dl \quad \text{for } k_1, k_2 \in \mathcal{K}_\Gamma. \tag{2.12}$$

If mobility is equal to anisotropy ($\mu = \gamma$) then this special choice of mobility is known as *natural* mobility. If the initial condition of the evolution (2.11) is Wulff shape of anisotropy γ and μ is natural mobility, then the flow is self-similar, i.e., the Wulff shape shrinks to a point while preserving its shape [74], see for example, Figure 2.5 (left top).

2.2.3 Methods of representation of surfaces

Both the parametric and level set approaches are extended to anisotropic case [22]. It is evident that parametric approach does not handle topological changes in anisotropic mean curvature flow either, so that one can get the solution by using a parametric approach until singularities occur.

Level set approach

As described earlier, in the level set method $\Gamma(t)$ is expressed as a 0-level set of a smooth function u which is defined in a neighbourhood of $\Gamma(t)$ with non-zero gradient, i.e., $\Gamma(t) = \{x \in \mathbb{R}^d \mid u(x,t) = 0\}$ and $\nabla u(y,t) \neq 0$ where $y \in \Gamma(t)$, hence outer unit normal for u that is negative inside the curve is given by $\boldsymbol{n}(x,t) = \frac{\nabla u(x,t)}{|\nabla u(x,t)|}$. Then equation (2.10) in terms of u becomes a degenerate, nonlinear PDE.

Since we are looking for a solution beyond singularities, we need to consider *viscosity solution framework*. Thus existence of a solution in the next section is focused on solution of level set approach.

2.2.4 Existence of solution

The work on existence of solution of anisotropic mean curvature flow is an ongoing topic, especially for the crystalline problem. Within the framework of viscosity solution, the first global-in-time existence and uniqueness result for governing PDEs obtained by the level set approach is given by A. Chambolle, M.Morini and M.Ponsiglione in [15]. Their result is valid for arbitrary initial sets and for general (including crystalline) anisotropies, but it is restricted to natural mobility only, i.e., $\mu = \gamma$. Authors use standard parabolic comparison principle approach to prove uniqueness of solution.

Chambolle-Morini-Novaga-Ponsiglione generalized result of [15] in [16], by considering general mobilities. Authors adopt an approximation approach and proved the existence and uniqueness of weak solutions to anisotropic mean curvature flow, obtained as a limit of the viscosity solutions. Authors show that if $\gamma_n \to \gamma$, with γ_n smooth, and if $\mu_n \to \mu$, where μ_n is γ_n- regular *uniformly* with respect to n, then the corresponding viscosity level set solutions u_n converge locally uniformly to the unique distributional level set flow with anisotropy γ and (γ-regular) mobility μ.

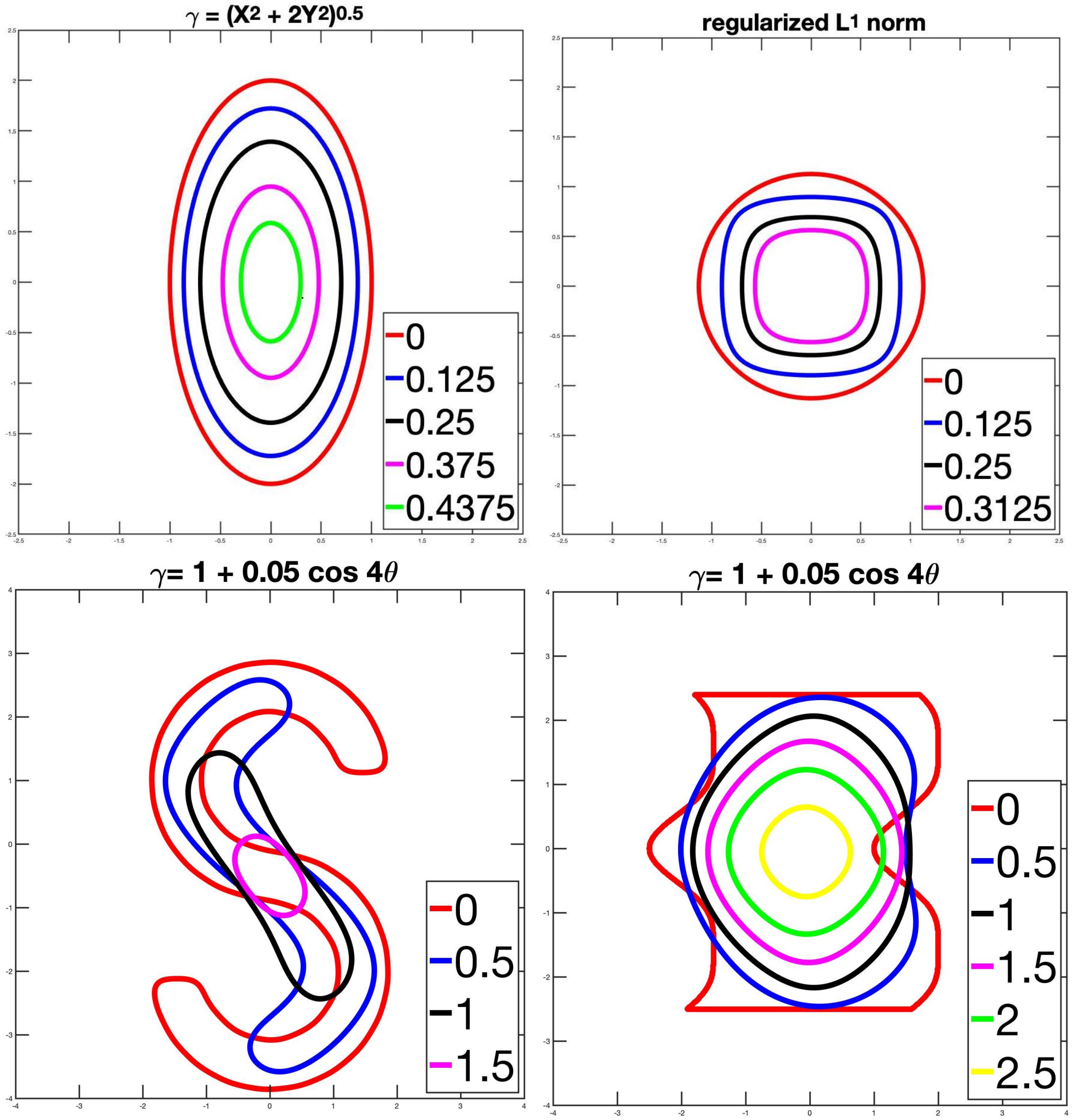

Figure 2.5: Evolution of closed curve by anisotropic mean curvature flow. Results are obtained by thresholding method.

2.2.5 Examples

To demonstrate evolution by AMCF, we select several anisotropies and initial shapes, see Figure 2.5. In each plot, numbers in the box indicate time.

- Top-left : anisotropy is $\gamma(x, y) = \sqrt{x^2 + 2y^2}$ and initial condition is the corresponding Wulff shape, i.e., ellipse.
- Top-right : initial curve is a circle and it is evolved by regularised l^1 anisotropy i.e., $\gamma(x, y) = \sqrt{\epsilon^2(x^2 + y^2) + x^2} + \sqrt{\epsilon^2(x^2 + y^2) + y^2}$.
- Bottom-left: anisotropy $\gamma(\theta) = 1 + 0.05 \cos 4\theta$ and smooth S-shape as initial condition
- Bottom-right : anisotropy $\gamma(\theta) = 1 + 0.05 \cos 4\theta$ and irregular shape as initial condition.

All the above curves converges to a point while asymptotically approaching to the Wulff shape of the corresponding anisotropy.

2.2.6 Numerical methods

Front tracking

Similar to the isotropic energy case, we can solve anisotropic mean curvature flow problem by using *front tracking approach*. The idea of front tracking approach is the same as mentioned in Section 1.1.6, except for a different formula of anisotropic curvature to be discretized. Again, we need to perform point redistribution during the evolution. Outline of the method presented in [66] is given in Appendix A.6.

Results obtained by implementing front tracking method from [66] are presented in Figure 2.6. In the left plot, we use anisotropy $\gamma = 1 + 0.1 \cos 3\theta$ and circle as initial condition. Evolution is shown at equal time intervals of size 0.5. We plot the corresponding Wulff shape (dotted black line); to show that the curve converges to a point while asymptotically approaching Wulff shape. A similar test is carried out using different anisotropy and different initial condition; see the right side plot. Namely, we use anisotropy $\gamma = 1 + 0.05 \cos 5\theta$, also known as 5-fold anisotropy, along with elliptical initial shape.

Since it is possible to obtain arbitrarily accurate approximations by increasing number

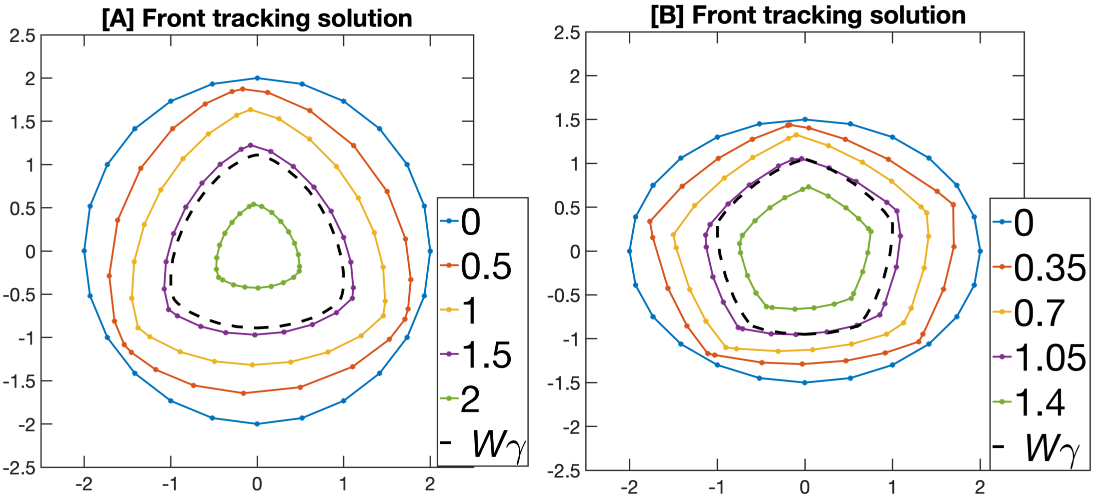

Figure 2.6: Results obtained by anisotropic front tracking approach. Left: Evolution of circular shape with anisotropy $\gamma = 1 + 0.1\cos 3\theta$. Right: Evolution of elliptic shape with anisotropy $\gamma = 1 + 0.05\cos 5\theta$.

of discrete points, the front tracking method is used to evaluate other numerical methods when analytical solution is not available. We do so in Section 4.2.

Numerical solution of level set equation

The finite element method is one of the direct methods to solve level set PDE. For example, a weak formulation of a (regularized) level set equation for anisotropic mean curvature motion was considered by Clarenz et al. in [19], where it is solved using a finite element scheme. Authors of [11] generalized the technique introduced in [19] to higher-order flows. These direct methods are hard to solve as already mentioned in Section 1.1.6.

To solve the governing PDEs obtained by level set approach numerically, we use thresholding method; details of which are given in Chapter 3. For demonstration, we show some results in Figure 2.5, which are obtained by implementing a thresholding scheme for anisotropic energy.

2.3 Anisotropic mean curvature flow with area constraint

Anisotropic mean curvature flow is congruous with mean curvature flow in the sense of area preservation, i.e., $\frac{dA}{dt} \leqslant 0$. Therefore, as a natural extension of the problem defined in Section 2.2.1, we consider a two-phase problem with area constraint. The setup for this problem is the same as in Section 2.2. Suppose A_0 is the area enclosed by initial curve Γ_0. Similar to isotropic case, we use Lagrange multiplier method to find minimum energy under area constraint of the extended energy

$$E_\lambda(\Gamma) = \int_\Gamma \gamma(\boldsymbol{n})\, dl + \lambda \frac{1}{2} \int_\Gamma (x, y) \cdot \boldsymbol{n}\, dl. \tag{2.13}$$

2.3.1 Anisotropic mean curvature flow with area constraint

To find minimum energy with area constraint, one needs first variation of (2.13). Calculations are almost identical to (1.21) and (2.9) leads to

$$\frac{d}{d\epsilon} E_\lambda(\Gamma_\epsilon)\Big|_{\epsilon=0} = \int_\Gamma (\kappa_\gamma - \lambda)(\boldsymbol{n} \cdot \phi)\, dl \tag{2.14}$$

To obtain equation of area preserving anisotropic mean curvature flow, we repeat the procedure, leading to (2.10) and obtain the following form of area-preserving mean curvature flow,

$$V = -\kappa_\gamma + \lambda. \tag{2.15}$$

To find the specific value of Lagrangian multiplier λ, we avail of area preservation condition, i.e., $\frac{dA}{dt} = 0$. With the help of calculation presented in Section 1.2.1, we get

$$\lambda = \frac{\int_\Gamma \kappa_\gamma\, dl}{\int_\Gamma 1\, dl}.$$

Note that λ is average anisotropic mean curvature along the curve, we denote it by κ_{avg}. This concludes the form of area preserving anisotropic mean curvature flow as,

$$V = -\kappa_\gamma + \kappa_{\text{avg}}. \tag{2.16}$$

Smilarly to Section 2.2.2, (2.16) is extended to higher dimensions by changing anisotropic curvature to anisotropic mean curvature; there, it is known as volume-preserving anisotropic MCF. Detailed derivation of (2.16) in higher dimensions is given in [1].

Similar to (2.11), we can change inner product definition to add mobility μ term; then, we can introduce area-preserving weighted mean curvature flow as follows:

$$V = -\mu\kappa_\gamma + \kappa_{\text{avg}}. \tag{2.17}$$

Here, value of avarage curvature is different than area-preserving anisotropic MCF and that is equal to $\kappa_{\text{avg}} = \frac{\int_\Gamma \mu\kappa_\gamma \, dl}{\int_\Gamma 1 \, dl}$. If we choose natural mobility in (2.17), and Wulff shape as initial condition, then there is no evolution. This fact is helpful to check the accuracy of numerical methods to solve (2.17).

2.3.2 Existence of solution and properties

The stationary solution of (2.17) is known from [72, 12] to be the Wulff shape of given anisotropy. In other words, Wulff shape is the shape that possesses minimum energy (2.13). Here, we are interested in both the evolution and stationary solution; therefore, knowing final solution is not sufficient.

For area-preserving weighted mean curvature flow, i.e., (2.17), [1] proved the existence of solution along with some properties for convex initial condition. The author extends the results of [46] from isotropic to anisotropic case. A key property is the preservation of convexity of initial convex shape as stated in the following proposition.

Proposition 2.3.1. *[1] If Γ_0 is smooth and strictly convex, then the solution of equation* (2.17) *with initial condition Γ_0 exists and is smooth and strictly convex for all positive times.*

Author also showed that convex solutions of (2.17) converge smoothly and exponentially fast to Wulff shape as $t \to \infty$.

The above result holds until singularity occurs. The existence of solution beyond singularities is given by Bellettini et al. [6], provided that the initial condition is compact and convex. Their result holds not only for smooth anisotropies but also for crystalline ones. The result of [6] extended to the non-convex setting by Kim et al. [50], where authors proved the global existence of volume-preserving mean curvature flow, particularly for the crystalline case.

2.3.3 Examples

For demonstration purpose, we use same anisotropies and initial shapes as mentioned in Figure 2.5. For details see Figure 2.7, where each initial shape is evolving and converging to respective Wulff shape. Table at bottom-right shows the time. In top-left plot, negligible evolution is observed because initial condition is Wulff shape and the difference between red and black lines is the error caused by numerical method.

2.3.4 Numerical methods

Similarly to previous cases, direct methods can give the desired solution, but one faces difficulties as mentioned in Section 1.1.6. We solve governing equations using thresholding method. Details of thresholding method for this flow is given in Chapter 3. In Figure 2.7, we demonstrate results obtained by implementing the thresholding method.

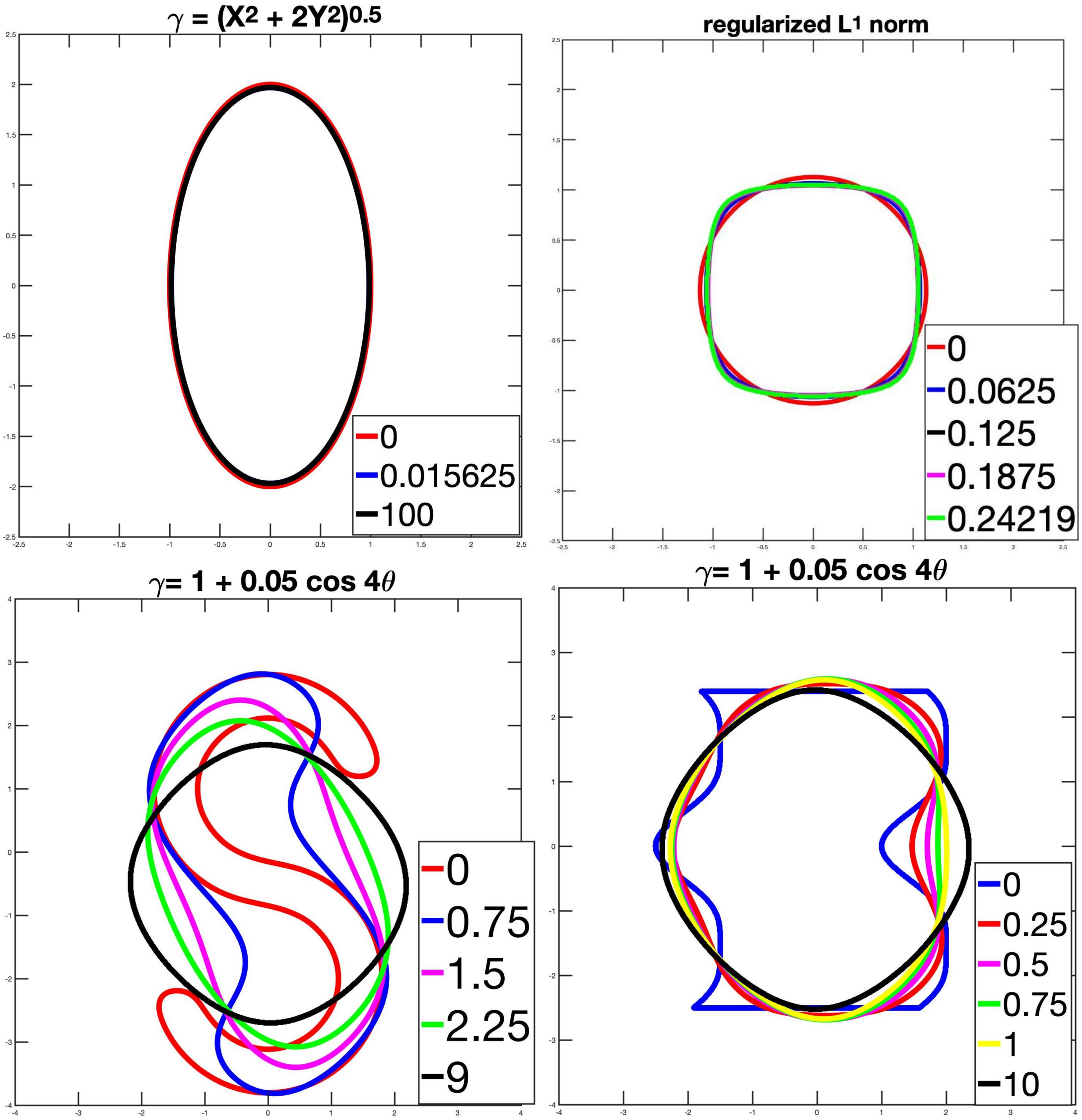

Figure 2.7: Evolution of closed curve by anisotropic mean curvature flow with area constraint. Results are obtained by thresholding method.

Chapter 3

Thresholding method

This chapter presents a numerical method for computing weighted mean curvature flow, that is based on the level set approach. We focus on the level set representation since our goal is to deal with topology changes. We discuss convergence of the algorithm and properties of convolution kernels, which are used to realize the anisotropic problem. For area-preserving mean curvature flow, we introduce two methods to preserve the enclosed area numerically.

3.1 Isotropic energy without area constraint

In this section, we introduce a numerical method to solve the evolution problem presented in Section 1.1. As we know from Section 1.1.3, there are different ways to represent interface and each choice of representation leads to different PDEs. Since our focus is on automatic handling of topological changes, we use the level set approach.

When we use level set representation, mean curvature flow (1.5) transform into a nonlinear, degenarated PDEs, i.e., (1.17). We rewrite (1.17) as follows:

$$u_t \;=\; |\nabla u| \;\nabla \cdot \left(\frac{\nabla u}{|\nabla u|}\right) = \sum_{i,j=1}^{d} \left(\delta_{ij} - \frac{u_{x_i} u_{x_j}}{|\nabla u|^2}\right) u_{x_i x_j}. \tag{3.1}$$

In two dimensions, (3.1) takes the following form

$$u_t - (u_{xx} + u_{yy}) + \frac{1}{|\nabla u|^2}\left(u_{xx}u_x^2 + u_{yy}u_y^2 + 2u_{xy}u_x u_y\right) = 0. \tag{3.2}$$

It is possible to solve (3.1) using direct methods, e.g. finite difference method, finite element method etc., but as already disicuss in Section 1.1.6, those approaches entail several complications.

As an alternative way to solve nonlinear PDEs, linearization is a common numerical approach. Linearization of PDE (3.1) leads to a heat type equation. This heat type equation can be solved with the help of convolution. One efficient numerical method to solve level set based mean curvature flow equation is introduced in [59]. It is called Bence-Merriman-Osher, or shortly BMO, algorithm. BMO algorithm is a diffusion generated motion scheme, where heat equation is solved with characteristic function of of the region enclosed by a closed curve as initial condition, and then updated curve is obtained by selecting a specific level set of the diffused function.

This scheme is efficient and straightforward because it repeats only two simple steps: convolution and thresholding, to get desired solution. In the convolution step, heat equation is solved by convolving a characteristic function and a convolution kernel G, which is positive, with unit mass, and radially symmetric. *Diffusion-generated* refers to the fact that convolution with the Gaussian kernel is equivalent to solving the diffusion equation [64]. Any kernel with the above-mentioned properties will work for the BMO scheme. In the original paper, authors used the Gaussian kernel, i.e.,

$$G(x) = \frac{1}{(4\pi)^{d/2}} \exp\left(\frac{|x|^2}{4}\right).$$

In thresholding step, we take a half-level set as updated position. Then go back to convolution step again and use updated position as initial condition. This scheme is summarised below:

Algorithm 1 BMO algorithm

Given a time step δt and a region $P^k \subset \mathbb{R}^d$ at time t_k, to get new region P^{k+1} at next time step $t_{k+1} = t_k + \delta t$, perform the following two steps:

$$\text{Convolution:} \qquad U^k = G_{\delta t} * 1_{P^k} \tag{3.3}$$

$$\text{Thresholding:} \qquad P^{k+1} = \left\{ x \mid \; U^k(x) \leqslant \frac{1}{2} \right\} \tag{3.4}$$

Here 1_{P^k} is the characteristic function of the set P^k and $G_{\delta t}(x) = \frac{1}{(\delta t)^{d/2}} G\left(\frac{x}{\sqrt{\delta t}}\right)$.

3.1.1 Convergence of the algorithm

Convergence of algorithm to (1.5) was empirical by numerical experiments presented in [59] and [63]. Barles and Georgelini [4] has given the convergence proof of algorithm with the help of using the comparison principle, which is endowed by the positivity of Gaussian. The variational formulation for Algorithm 1 was given in Esedoglu and Otto [28]. In particular, they showed the following functional

$$E_{\delta t}(\Gamma) = \frac{1}{\delta t} \int_{\Gamma} G_{\delta t} * 1_P \, dx \tag{3.5}$$

is a non-local approximation to lentgh energy, and is dissipated by the Algorithm 1 at every stepsize, regardless of time step. Thus (3.5) is is a Lyapunov functional for Algorithm 1, establishing its unconditional gradient stability [25].

Idea behind Algorithm 1

We explain the intuitive idea why algorithm 1 works to approximate mean curvature flow. To solve (3.1), consider the following function, called, sign distance function (SDF)

$$u(x) = \begin{cases} dist(x, \Gamma), & x \in \mathbb{R}^d \backslash (\Omega \cup \Gamma) \\ 0 & x \in \Gamma \\ -dist(x, \Gamma) & x \in \Omega \end{cases} \tag{3.6}$$

Here, $\Omega \subset \mathbb{R}^d$ is an open bounded set such that $\Gamma = \partial\Omega$. One example of SDF is given in Figure 1.2 (plots on the top). Note that 0-level set of SDF is the curve Γ, and $|\nabla u| = 1$ hold almost everywhere. If we plug in this value in (3.1) then we end up with the heat equation which can be solved through convolution with Gaussian kernel. However, since the solution deviates from the SDF, we need to restrict the time to a short interval, get a new SDF, and repeat this procedure. It turns out that a characteristic function can be used instead of SDF.

3.1.2 Numerical example

To illustrate the example of thresholding scheme, we perform a simple numerical test. Consider the shrinking circle problem from the Section 1.1.6.

To implement Algorithm 1, first, we fix rectangular domain $[-5, 5] \times [-5, 5]$. Note that the domain size is taken sufficiently large, so that the boundary will not influence the motion of the curve. Spatial variables are discretized on a rectangular grid with grid cells of size $dx \times dy$. We use square lattice with $dx = dy$. This setting of computational domain is the same for all numerical tests presented throughout this thesis. We solve convolution (3.3) using Fast Fourier Transform (FFT). First, we convert kernel and characteristic function into Fourier form and then take inverse Fourier transform of their product. After convolution step we check at each grid point if value of diffused function U^k is greater than $\frac{1}{2}$. If it is so, we change value to 1, otherwise to 0, obtaining P^{k+1}.

We start with initial radius $r_0 = 2$ and evolve circle by implementing Algorithm 1. Here we are looking for isotropic energy and circle is Wulff shape of given energy; therefore, circle preserves its shape during evolution, as demonstrated in left plot of Figure 3.1. We compare thresholding results with analytical result, derived in Section 1.1.6. Right side plot shows radius of circle at each time for thresholding (red) and analytical (black) solutions. Both results are very close throughout time, except near the extinction time.

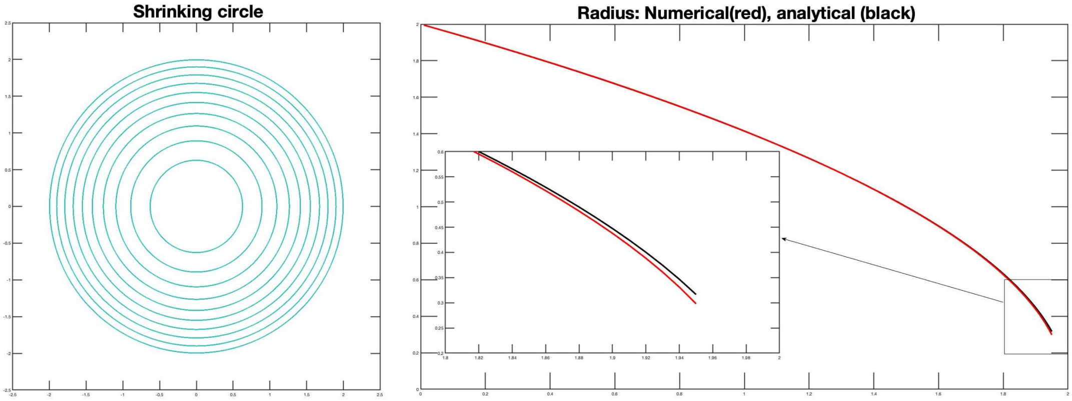

Figure 3.1: The initial radius is $r_0 = 2$, grid size $dx = 0.0048$ and timestep $\delta t = 0.01$. (Left) Evolution of circle by mean curvature flow at equal interval. (Right) Comparison between numerical and analytical radius of circle during evolution.

3.2 Isotropic energy with area constraint

In this section, we present a thresholding method to solve governing PDE of the level set approach to area-preserving MCF (1.26) introduced in Section 1.2. The additional area term demands a modification in thresholding step of Algorithm 1, namely, to preserve the area, we change the thresholding height from half-level set to appropriate thresholding height (say δ). Note that the appropriate thresholding height is not fixed during evolution, and we need to find it at each time step. We summarise the resulting scheme in general dimension as follows:

```
Algorithm 2 BMO algorithm with volume constraint
Given a time step $\delta t$ and a region $P^k \subset \mathbb{R}^d$ at time $t_k$, to get new region $P^{k+1}$ at next time step $t_{k+1} = t_k + \delta t$, perform the following two steps:
    Convolution:     $U^k = G_{\delta t} * 1_{P^k}$     (3.7)
    Thresholding:    $P^{k+1} = \{x \mid U^k(x) \leqslant \delta^k\}$     (3.8)
Here $\delta^k$ is chosen so that the volume of phase $P^{k+1}$ is equal to the volume of phase $P^0$.
```

All level sets of a solution to level set PDE move by mean curvature flow, so it should be reasonable to take a thresholding height different than $\frac{1}{2}$. History of finding thresholding height start with, Mascarenhas [58], who consider κ_{avg} as a constant (say a) in motion (1.26) and showed that $V = \kappa + a$ motion can be obtained by using following threhsolding height:

$$\frac{1}{2} - \frac{a}{2}\sqrt{\frac{\delta t}{\pi}}. \tag{3.9}$$

Later, Ruuth and Wetton [65] replace a by κ_{avg} and showed that flow (1.26) is possible by following thresholding height

$$\frac{1}{2} - \frac{\kappa_{avg}(t)}{2}\sqrt{\frac{\delta t}{\pi}}. \tag{3.10}$$

Algorithm 2 was intropduced in [65].

3.2.1 Convergence

Volume preserving mean curvature flow does not allow for a comparison principle. Therefore *conditional* convergence of a scheme introduced by Ruuth and Wetton [65], i.e., Algorithm 2 is proved by Laux and Swartz [56]. To prove the convergence, the authors set the following environment:

Denote the characteristic function of P^k at k-th time step by $\mathcal{X}^k$, and interpolate these functions piecewise constantly in time, i. e.,

$$\mathcal{X}^{\delta t}(t) = \mathcal{X}^k, \qquad \text{for } t \in [k\delta t, (k+1)\delta t).$$

Based on the result of [28], they defined the following approximation of energies

$$E_{\delta t}(\mathcal{X}) = \frac{1}{\sqrt{\delta t}} \int (1 - \mathcal{X}) G_{\delta t} * \mathcal{X} \, dx \tag{3.11}$$

for $\mathcal{X} : \mathbb{R}^d \to \{0, 1\}$. As $\delta t \to 0$, (3.11) converge to the perimeter functional

$$E(\mathcal{X}) = \frac{1}{\sqrt{\pi}} \int |\nabla \mathcal{X}|$$

with respect to L^1-topology. Esedoglu and Otto [28] proved the Γ convergence and its consequence of pointwise convergence of the functionals,

$$E_{\delta t}(\mathcal{X}) \to E(\mathcal{X}) \qquad \text{for any } \mathcal{X} \in \{0, 1\}. \tag{3.12}$$

At last, authors assume the following convergence of the energies, which is not guaranteed by the a priori estimates

$$\int_0^T E_{\delta t}(\mathcal{X}^{\delta t}) \, dt \to \int_0^T E(\mathcal{X}) \, dt \tag{3.13}$$

Based on above estimates, authors of [56] gave following convergence theorem:
Theorem 3.2.1. *Let $T < \infty$ and $\mathcal{X}^0 \in \{0, 1\}$ with $E(\mathcal{X}^0) < \infty$ and $\{\mathcal{X}^0 = 1\} \subset \mathbb{R}^d$. After passage to a subsequence, the functions $\mathcal{X}^{\delta t}$ obtained by Algorithm 2 converge to a function $\mathcal{X}$ in $L^1((0, T) \times \mathbb{R}^d)$. Under the convergence assumption* (3.13)*, $\mathcal{X}$ s a solution of the volume-preserving mean-curvature flow equation.*

3.2.2 Methods to find thresholding height δ

To find thresholding height, i.e., δ, we have proposed two methods, namely, *bisection* and *sorting*.

Bisection approach

To find thresholding height δ^k of the diffused function U^k at k-th iteration, consider an interval $[\delta_l^k, \delta_r^k]$, where $\delta_l^k = \min_{x \in \Omega} U^k(x)$ and $\delta_r^k = \max_{x \in \Omega} U^k(x)$. Compute the area V_l of the δ_l^k-level set of U^k. Do the same for δ_r^k to obtain V_r. Now set the mid-point $\delta_b^k = \frac{\delta_l^k + \delta_r^k}{2}$ and calculate the area V_b of the corresponding level set. There are two cases, (case I) if V_b is less than area of P^0, then assign $\delta_l^k = \delta_b^k$ and repeat the above process.

(case II) if V_b is greater than area of P^0, then assign $\delta_r^k = \delta_b^k$ and repeat the above process. If both these cases fail, it means we have reached the desired δ. This approach is summarised as follows:

Algorithm 3 Bisection approach to find thresholding height

Given an initial volume V_0 of phase P^0 and diffused function U^k at k-th iteration by (3.7), assign $\delta_l^k = \min_{x\in\Omega} U^k(x)$ and $\delta_r^k = \max_{x\in\Omega} U^k(x)$. Set $V_l = \{x \mid U^k(x) \leqslant \delta_l^k\}$ and $V_r = \{x \mid U^k(x) \leqslant \delta_r^k\}$. To get volume preserving thresholding height δ^k repeat the following steps:

$$(1)\,\text{Mean and volume:}\quad \delta_b^k = \frac{\delta_l^k + \delta_r^k}{2}; \qquad V_b = \{x \mid U^k(x) \leqslant \delta_b^k\} \tag{3.14}$$

(2) Bisection: · If $V_b < V_0$, set $\delta_l^k = \delta_b^k$ and go to step (1).

· If $V_b > V_0$, set $\delta_r^k = \delta_b^k$ and go to step (1).

· If $V_b = V_0$, set $\delta^k = \delta_b^k$ and terminate.

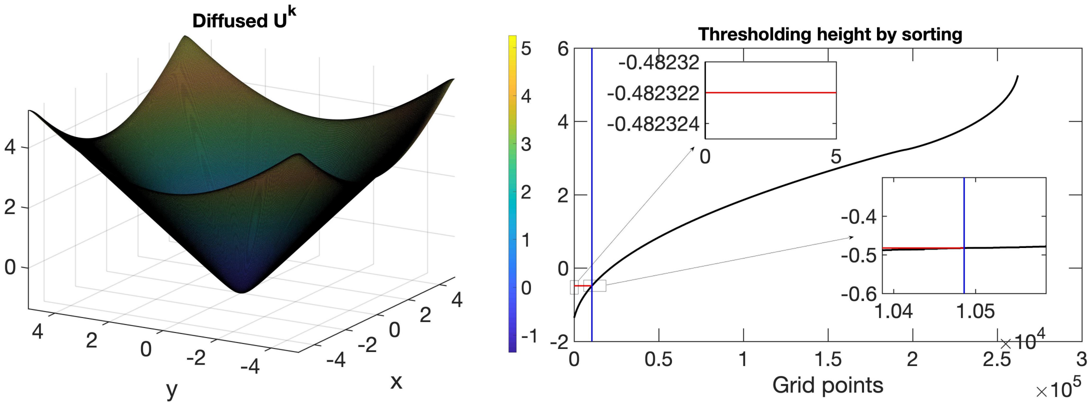

Figure 3.2: Sorting approach to find thresholding height

Sorting approach

Unlike bisection, sorting approach is a non-iterative way to find thresholding height.We explain the sorting approach using a specific example.

Suppose area enclosed by initial curve is A. First we discretize the computational domain using square grid, as explained in Section 3.1.2. Convert A into grid-area A_g, i.e., if dx is the side length of the grid then $A_g = A/dx^2$. Suppose diffused U^k is given by (3.7) at k-th iteration, as shown in left side plot of Figure 3.2. The algorithm to find δ^k takes the following steps:

- Sort the values of U^k at all grid-points in ascending order, and call this list *sortlist*. It is plotted using black line in right side plot of Figure 3.2.
- X-axis in this plot represents grid points number. Draw a line $X = A_g$ (blue line in the Figure) and find its intersection with *sortlist*.
- Y- coordinate of the intersection is the desired thresholding height δ^k.

We remark that the sorting approach cannot handle multiphase problems, i.e., three or more phases evolution problems. If the area of any two phases is different in a multiphase problem, then those phases need different thresholding heights to preserve their respective area. But in sorting approach, we take ascending order (*sortlist*) of the whole domain; thus, it becomes difficult to recognise which point belongs to which phase in the sortlist.

3.2.3 Numerical test

To scrutinize numerical performance of the scheme and juxtapose bisection and sorting approach, we consider a simple problem introduced in [67]. Take two circles with radii $r_1 = \sqrt{3}$ and $r_2 = 1.4$ as shown in top-left plot of Figure 3.3 (in red colour). We treat them as a single-phase and evolve by area-preserving mean curvature flow, which results in growth of the large circle. On the other hand, the smaller circle will shrink. For comparison between solution obtained by thresholding scheme and analytical solution, we implement Algorithm 2 until the radius of smaller circle reaches the "final time" 0.75. Note that the evolution of radii follows the equations

$$r_1' = \frac{-1}{r_1} + \frac{2}{r_1 + r_2}, \qquad r_2' = \frac{-1}{r_2} + \frac{2}{r_1 + r_2}.$$

We use Matlab's *ode113* function to solve the above system, which gives a precise approximation of analytical solution.

Evolution of the circles is depicted in left plot of Figure 3.3, where black lines show intermediate shapes and blue circles indicate final shape. The right plot shows agreement between the radius of both circles with their analytical values. Results obtained by thresholding method is almost identical to the analytical solution. We use bisection approach for this test. After that, we check thresholding height, i.e., δ at each time step using both sorting and bisection approach for the same test. Both these approaches give almost identical values, see left plot in Figure 3.4.

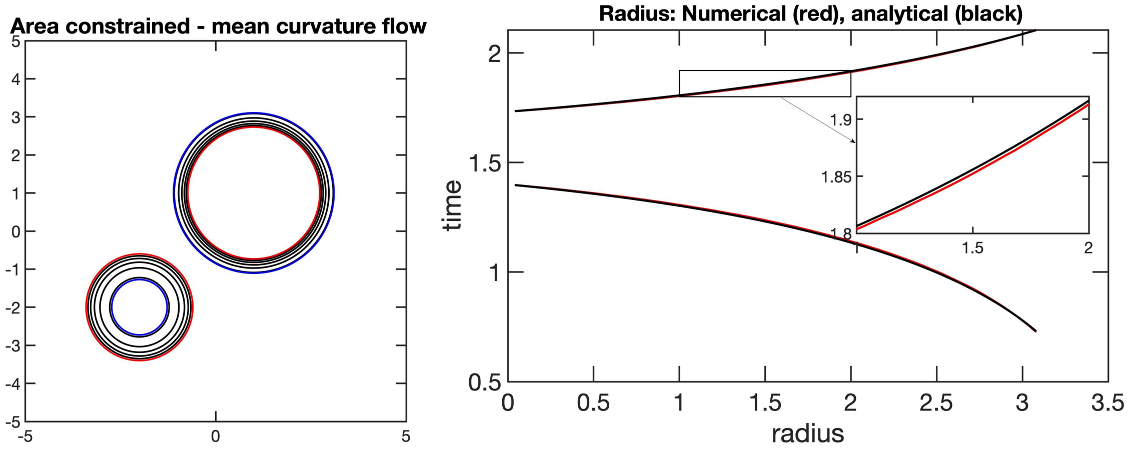

Figure 3.3: Evolution of two circles by MCF with initial radii $r_1 = \sqrt{3}$ and $r_2 = 1.4$ obtain by thresholding method with $dx = 0.0195$ and $\delta t = 0.04$. Left: numerical result, red: initial circle, blue: final shape at $t = 0.75$, black: intermediate evolution at equal time intervals. Right: comparison between the analytical and numerical radii of both circles.

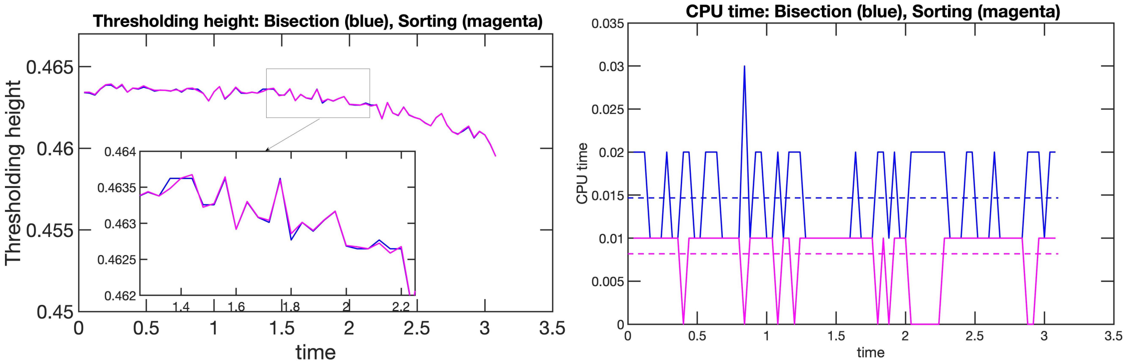

Figure 3.4: Left: value of thresholding height δ at each time step obtained by bisection (blue) and sorting approach (magenta). Right: CPU time to calculate thresholding height δ for bisection and sorting approach.

Since both approaches give the same δ, thus identical error; it is of interest to know which approach requires less computational time. The right plot in Figure 3.4 shows CPU time required for each time step in both approaches. The dotted lines show *mean time* of each approach. Here *mean time* means the sum of time required to find thresholding height at each iteration divided by the total number of iterations.

It is clear from the plot that *sorting* approach requires less time in this test. This outcome was expected since bisection method involves several iterations. Note that the difference of *mean time* between both approaches drastically increases for smaller values of dx. Therefore, we use sorting method for all upcoming area-preserving simulations.

3.3 Anisotropic case

We present thresholding method to solve evolution problem (2.11) introduced in Section 2.2.2. Recall that the original BMO uses the Gaussian convolution kernel to deal with the isotropic problem. Thresholding method can be extended to anisotropic energies by replacing Gaussian with a suitable kernel K [47]. This leads to the following algorithm:

Algorithm 4 Anisotropic two-phase BMO algorithm

Given a time step δt and a region $P^k \subset \mathbb{R}^d$ at time t_k, to get new region P^{k+1} at next time step $t_{k+1} = t_k + \delta t$, perform the following two steps:

$$\text{Convolution:} \qquad U^k = K_{\delta t} * 1_{P^k} \tag{3.15}$$

$$\text{Thresholding:} \qquad P^{k+1} = \left\{ x \mid \ U^k(x) \leqslant \frac{1}{2} \int_{\mathbb{R}^d} K(y)\,dy \right\} \tag{3.16}$$

Here 1_{P^k} is the characteristic function of the set P^k and $K_{\delta t}(x) = \frac{1}{(\delta t)^{d/2}} K\left(\frac{x}{\sqrt{\delta t}}\right)$.

To present existing results regarding the above algorithm, we need to assume the following regularity, decay and continuity properties conditions on kernel K [47]:

$$K(x) = K(-x), \qquad K(x) > 0, \tag{3.17}$$

$$\int_{\mathbb{R}^d} K(x)\,dx = 1, \qquad \int_{\mathbb{R}^d} |x|^2 K(x)\,dx < \infty, \tag{3.18}$$

$$\text{there exist } C > 0 \text{ and } p > d+1 \text{ such that } |K(x)| \leqslant \frac{C}{1+|x|^p}, \tag{3.19}$$

$$K(x) \in L^1(\mathbb{R}^d), \ xK(x) \in L^1(\mathbb{R}^d). \tag{3.20}$$

Further,

$$\lim_{\epsilon \to 0} \sup_{\mathcal{O} \in \mathbf{O}} \int_{\mathbb{R}^{d-1}} |K \circ \mathcal{O}(x', \epsilon g(x')) - K \circ \mathcal{O}(x', 0)| \ (1 + |x'|^2)\,dx' = 0, \tag{3.21}$$

for every map $g : \mathbb{R}^{d-1} \to \mathbb{R}^{d-1}$ of the form

$$g(x') = \langle Mx', x' \rangle + a,$$

where M is a $(d-1) \times (d-1)$ symmetric matrix and $a \in \mathbb{R}$, and $\mathbf{O}$ is the set of $(d-1) \times (d-1)$ orthogonal matrices.

For every $(d-1) \times (d-1)$ orthogonal matrix $\mathcal{O}$

$$\int_{\mathbb{R}^{d-1}} K \circ \mathcal{O}(x', 0)\, dx' > 0 \tag{3.22}$$

3.3.1 Convergence and stability of Algorithm 4

Convergence

The convergence of Algorithm 4 to the solution of governing PDE of anisotropic mean curvature flow proved in [47]. We give a shortened form of their convergence theorem as follows:

Theorem 3.3.1. *If kernel K satisfies* (3.17), (3.18), (3.19)*, and smoothness condition, i.e.,*

$$p \mapsto \int_{p^\perp} K(x)\, d\mathcal{H}^{d-1}(x), \;\; \textit{and}\; p \mapsto \int_{p^\perp} x_i x_j K(x)\, d\mathcal{H}^{d-1}(x) \;\; \textit{are continous on}\; \mathbb{S}^{d-1},$$

then Algorithm 4 converges as $\delta t \to 0$ to the viscosity solution of the equation

$$u_t = F(D^2 u, Du),$$

where,

$$F(M,p) = \left(\int_{p^\perp} K(x)\, d\mathcal{H}^{d-1}(x) \right)^{-1} \left(\frac{1}{2} \int_{p^\perp} \langle Mx, x \rangle K(x)\, d\mathcal{H}^{d-1}(x) \right),$$

for $p \in \mathbb{R}^d$ and M is a $d \times d$ symmetric matrix.

To prove the above theorem, authors of [47] used the comparison principle via positivity of kernel. Thus positivity of the kernel in physical domain becomes essential for convergence.

Anisotropy corresponding to kernel K

[25] showed the corresponding anisotropy and mobility represent by the given kernel in the form of proposition:

Proposition 3.3.2. *[25] Let K satisfy* (3.17) *and* (3.19)*. Assume that $\widehat{K}(n\xi)$, as a func-*

tion of ξ, is a Schwartz class for every $n \in \mathbb{S}^{d-1}$ then

$$\begin{aligned} \gamma_K(n) &= -\frac{1}{4\pi^2}\int_{\mathbb{R}} \frac{\widehat{K}(n\xi) - \widehat{K}(0)}{\xi^2}\, d\xi && (3.23) \\ 2\mu_K(n) &= \left(\int_{\mathbb{R}} \widehat{K}(n\xi)\, d\xi\right)^{-1} && (3.24) \end{aligned}$$

Since we use different definition of the Fourier transform, (3.23) and (3.24) formally differ from the original paper. For the proof of mobility (3.24) authors used the following definition of the mobility,

$$2\mu_K(n) = \left(\int_{n^\perp} K(x)\, d\mathcal{H}^{d-1}\right)^{-1}. \qquad (3.25)$$

Stability and motion by Algorithm 4

To prove unconditional gradient stability of Algorithm 4 Elsey-Esedoglu [25] use approximation of actual energy, i.e.,

$$E_{\delta t}(P, K) = \frac{1}{\sqrt{\delta t}} \int_{\mathbb{R}^d \backslash P} K_{\delta t} * 1_P\, dx. \qquad (3.26)$$

Similar to the isotropic version, (3.26) is a Lyapunov function for Algorithm 4. Unconditional gradient stability of Algorithm 4 is proved by [25] and restated in [30] in the form of the following proposition:

Proposition 3.3.3. *Let K satisy $K(x) = K(-x)$, $\int_{\mathbb{R}^d} K(x) > 0$ and* (3.19). *If $\widehat{K} \geqslant 0$, where $\widehat{K}$ is the Fourier transform of K, then for any time step size $\delta t > 0$, Algorithm 4 decreases the energy* (3.26) *at every time step.*

This proposition convey the importance of the positive Fourier transform $\widehat{K}$. The connection between approximate energy and anisotropy corresponding to the kernel is presented in [25] as following proposition:

Proposition 3.3.4. *[25] Let P is a compact subset of $\mathbb{R}^d$ with smooth boundary, kernel K satisfy* (3.17) *and* (3.19) *then*

$$\lim_{\delta t \to 0} E_{\delta t}(P, K) = \int_{\partial P} \gamma_K(n(x))\, d\mathcal{H}^{d-1}(x), \quad \textit{where } \gamma_K(n) = \frac{1}{2}\int_{\mathbb{R}^d} |n \cdot y| K(y)\, dy. \qquad (3.27)$$

Here, $n(x)$ denotes the unit normal at a point $x \in \partial P$.

Note that γ_K in the above proposition is equivalent to (3.23). After convergence and stability of algorithm, the natural question arises, does Algorithm 4 move interface with correct motion law. The answer of this question is given in Elsey and Esedoglu [25]; we summarise their result in two dimensions as follow:

Proposition 3.3.5. *One step of Algorithm 4 moves a smooth interface with the normal speed:*

$$V(x) = \mu_K(\boldsymbol{n}(x)) \left(\gamma_K''(\boldsymbol{n}(x)) + \gamma_K(\boldsymbol{n}(x))\right) \kappa, \tag{3.28}$$

to leading order in δt.

To summarise, the positive Fourier transform of the kernel K guarantees the stability of the algorithm. On the other hand, a positive kernel in the physical domain proves the convergence of the algorithm under additional regularity assumptions. But [25] showed that achieving these two conditions together is impossible for the anisotropies with *non-zonoid* Wulff shape. The fact presented in the following theorem.

Theorem 3.3.6 ([25])**.** *Threshold dynamics algorithm* (3.15) *and* (3.16) *with a positive kernel can approximate a given weighted mean curvature flow if and only if the Wulff shape corresponding to the anisotropy is a zonoid. Moreover, if the Wulff shape is not a zonoid then a positive convolution kernel cannot be found for any other anisotropy the Wulff shape of which is close enough in the Hausdorff metric.*

The above theorem is known as a *barrier theorem*, c.f. [25]. Since all the centrally symmetric shapes are a zonoid in two dimensions, the barrier theorem does not imply a strong restrictions on the class of anisotropies. On the other hand, in three dimensions barrier theorem becomes more restrictive. See Figure 3.5 for examples of non-zonoidal shapes in three dimensions. Crystalline anisotropy with regular octahedron is not zonoid, thus one can not find the kernel which is positive in the physical domain.

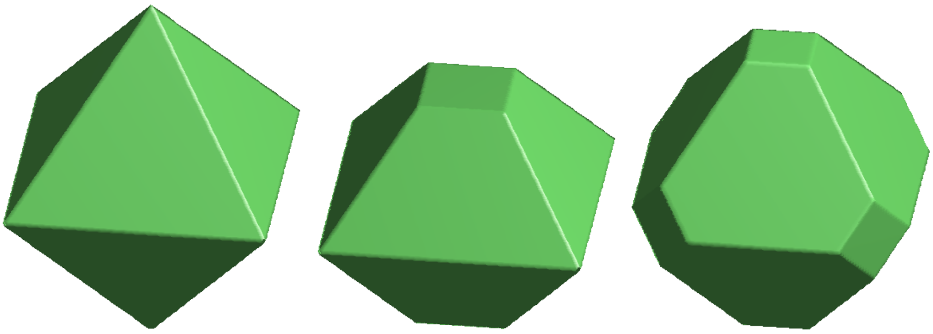

Figure 3.5: Examples of non-zonoidal shapes in three dimensions. This picture is taken from [25].

Chapter 4

Convolution kernels and their comparison

In this chapter, we address the question of how to construct kernels yielding the desired evolution. We review several kernels proposed in the literature and look into their properties, especially from the numerical point of view.

4.1 Convolution kernels

For a given kernel, the properties of the thresholding scheme transpire as presented in the previous chapter. Here we consider the inverse problem, i.e., finding a suitable kernel for a given anisotropy and mobility. Over the last two decades, various attempts have been made to solve this problem. The following subsections review the well known major kernels.

4.1.1 Bonnetier–Bretin–Chambolle kernel (BBC)

For a given anisotropy γ, the first notable, successful attempt to find a corresponding kernel was made in [9]. Authors construct the kernel so that the positivity of the kernel in the Fourier domain is always guaranteed.

The core idea behind their construction is as follow: consider a bounded closed set $P \subset \mathbb{R}^d$. Denote the Fourier transform of a function u by $\mathfrak{F}u$, and u is a solution which solves following parabolic equation:

$$\begin{aligned}\frac{\partial u}{\partial t}(x,t) &= \tilde{\Delta} u(x,t), \qquad t>0 \quad x \in \mathbb{R}^d, &(4.1)\\ u(x,0) &= 1_P(x). &(4.2)\end{aligned}$$

Where, operator $\tilde{\Delta}$ is defined by

$$\tilde{\Delta}(u) = \mathfrak{F}^{-1}\exp(-\mathfrak{F}(u)(2\pi\gamma(\xi))^2),$$

and can be seen as a linearization of anisotropic Laplacian, i.e., $(\nabla \cdot (\boldsymbol{n}_\gamma(\nabla u)\gamma(\nabla u)))$ in the Fourier space. At the end, they expressed solution u of (4.1) and (4.2) as a convolution product of 1_P and the desired anisotropic kernel

$$\widehat{K}(\xi) = e^{-4\pi^2\gamma^2(\xi)}. \tag{4.3}$$

With the help of (3.23), it can be confirmed that the BBC kernel yields the correct anisotropy; indeed, denoting by γ_K the anisotropy corresponding to kernel K, we have

$$\begin{aligned}\gamma_K(n) &= -\frac{1}{4\pi^2}\int_{\mathbb{R}} \frac{\widehat{K}(n\xi)-\widehat{K}(0)}{\xi^2}\,d\xi\\ &= -\frac{1}{4\pi^2}\int_{\mathbb{R}} \frac{e^{-4\pi^2\xi^2\gamma^2(n)}-1}{\xi^2}\,d\xi\\ &= \frac{1}{4\pi^2}\int_{\mathbb{R}} \frac{1-e^{-x^2}}{\frac{x^2}{4\pi^2\gamma^2(n)}}\,\frac{dx}{2\pi\gamma(n)}, \qquad \text{where } x = 2\pi\xi\gamma(n)\\ &= \frac{\gamma(n)}{2\pi}\int_{\mathbb{R}} \frac{1-e^{-x^2}}{x^2}\,dx\\ &= \frac{\gamma(n)}{\sqrt{\pi}}. &(4.4)\end{aligned}$$

Mobility μ_K associated to the BBC kernel can be derived using (3.24) as follows:

$$\begin{aligned}2\mu_K(n) &= \frac{1}{\int_{\mathbb{R}} \widehat{K}(n\xi)\,d\xi}\\ &= \frac{1}{\int_{\mathbb{R}} e^{-4\pi^2\xi^2\gamma^2(n)}\,d\xi}\\ &= \frac{2\pi\gamma(n)}{\int_{\mathbb{R}} e^{-x^2}\,dx}, \qquad \text{where } x = 2\pi\xi\gamma(n)\\ \mu_K(n) &= \sqrt{\pi}\gamma(n). &(4.5)\end{aligned}$$

Inspecting (4.5), one can notice that the mobility associated to the BBC kernel is fixed to the natural mobility and cannot be prescribed freely.

Since the kernel is always positive in the Fourier domain, Proposition 3.3.3 guarantees the stability of the thresholding scheme. On the other hand, the kernel may not satisfy (3.17) and (3.19) for some anisotropies, i.e., be negative in the physical domain, which prevents authors from giving rigorous proof of convergence.

For a given anisotropy γ, if B_γ is not ellipsoid, then the BBC kernel shows a slow decay rate. The slow decay rate arises for certain anisotropies because of singularity, which may appear at the origin of BBC kernel. The slow decay rate is a drawback of the BBC kernel, along with a lack of non-positiveness in the physical domain for some anisotropies, e.g., regularized crystalline anisotropy $\gamma(x, y) = |x| + |y|$.

We conclude BBC kernel by summarizing results. If anisotropy is strictly convex, then, using (4.3), it is possible to construct a kernel, which is positive in Fourier domain. The inverse Fourier transform of this kernel, i.e., physical form of the kernel, is nothing but a generalization of the Gaussian, which satisfies all the conditions mentioned in Proposition 3.3.3. Thus, the corresponding Algorithm 4 is stable. We summarise in the following theorem:

Theorem 4.1.1. *Let anisotropy γ be strictly convex. Then*
(i) there is a kernel K that is positive in Fourier domain. i.e., $\widehat{K} > 0$,
(ii) the corresponding thresholding algorithm decreases the approximated interfacial energy at every time step.

4.1.2 Elsey–Esedoglu kernels (EE)

In [25], authors construct a kernel, which is positive in both the physical as well as in the Fourier domain. The idea is to write the d-dimensional kernel as a weighted sum of smoothed one-dimensional Gaussians defined in a direction $\nu \in \mathbb{S}^{d-1}$ as

$$g_{\nu,\epsilon}(x) = \frac{1}{(4\pi)^{\frac{d}{2}}} \exp\left(-\frac{(x\cdot\nu)^2}{4}\right) \frac{1}{\epsilon^{d-1}} \exp\left(\frac{(x\cdot\nu)^2 - |x|^2}{4\epsilon^2}\right), \tag{4.6}$$

and solve (3.23) as well as (3.24) to obtain the correct weight function $\omega(\nu) : \mathbb{S}^{d-1} \to \mathbb{R}$, also called generating function. In the original paper, the mobility term contains an error; therefore, detailed derivation is demonstrated here. Fourier transform of (4.6) is given as follows:

$$\widehat{g}_{\nu,\epsilon}(\xi) = \exp\left(-4\pi^2(\xi\cdot\nu)^2\right)\exp\left(\epsilon^2 4\pi^2\left[(\xi\cdot\nu)^2 - |\xi|^2\right]\right). \tag{4.7}$$

The detailed derivation of (4.7) is given in Appendix A.7. Anisotropy corresponding to $g_{\nu,\epsilon}$ can be derived with the help of (4.7) and (3.23). In particular, for $n \in \mathbb{S}^{d-1}$ we have

$$\begin{aligned}
\gamma_{\nu,\epsilon}(n) &= \frac{1}{-4\pi^2}\int_{\mathbb{R}} \frac{\widehat{g}_{\nu,\epsilon}(n\xi) - \widehat{g}_{\nu,\epsilon}(0)}{\xi^2}\,d\xi \\
&= \frac{1}{-4\pi^2}\int_{\mathbb{R}} \frac{\exp(-4\pi^2(\nu\cdot n\xi)^2)\ \exp\left(4\pi^2\epsilon^2\left[(\nu\cdot n\xi)^2 - |n\xi|^2\right]\right) - 1}{\xi^2}\,d\xi \\
&= \frac{1}{-4\pi^2}\int_{\mathbb{R}} \frac{\exp(-\xi^2 4\pi^2\left[(\nu\cdot n)^2(1-\epsilon^2)+\epsilon^2\right]) - 1}{\xi^2}\,d\xi, \\
&= \frac{\sqrt{4\pi^2}\sqrt{(\nu\cdot n)^2(1-\epsilon^2)+\epsilon^2}}{-4\pi^2}\int_{\mathbb{R}} \frac{\exp(-h^2)-1}{h^2}\,dh \\
&= \frac{\sqrt{(\nu\cdot n)^2(1-\epsilon^2)+\epsilon^2}}{-2\pi}\left(-2\sqrt{\pi}\right) \\
&= \frac{1}{\sqrt{\pi}}\sqrt{(\nu\cdot n)^2(1-\epsilon^2)+\epsilon^2}.
\end{aligned} \tag{4.8}$$

Similarly, the mobility is computed from (3.24) as follows:

$$\begin{aligned}
\frac{1}{2\mu_{\nu,\epsilon}(n)} &= \int_{\mathbb{R}} \widehat{g}_{\nu,\epsilon}(n\xi)\,d\xi \\
&= \int_{\mathbb{R}} \exp(-4\pi^2(\nu\cdot n\xi)^2)\ \exp\left(4\pi^2\epsilon^2\left[(\nu\cdot n\xi)^2 - |n\xi|^2\right]\right)\,d\xi \\
&= \int_{\mathbb{R}} \exp(-\xi^2 4\pi^2\left[(\nu\cdot n)^2(1-\epsilon^2)+\epsilon^2|n|^2\right]\ d\xi \\
&= \int_{\mathbb{R}} \frac{\exp(-h^2)\,dh}{\sqrt{4\pi^2(\nu\cdot n)^2(1-\epsilon^2)+a\epsilon^2}}, \quad h = \xi\sqrt{4\pi^2(\nu\cdot n)^2(1-\epsilon^2)+a\epsilon^2} \\
&= \frac{\sqrt{\pi}}{2\pi\sqrt{(\nu\cdot n)^2(1-\epsilon^2)+\epsilon^2}} \\
\mu_{\nu,\epsilon}(n) &= \sqrt{\pi}\sqrt{(\nu\cdot n)^2(1-\epsilon^2)+\epsilon^2}.
\end{aligned} \tag{4.9}$$

As $\epsilon \to 0$, (4.8) and (4.9) converge to

$$\gamma_{\nu,\epsilon}(n) \to \frac{1}{\sqrt{\pi}}|\nu\cdot n| \quad \text{and} \quad \mu_{\nu,\epsilon}(n) \to \sqrt{\pi}|\nu\cdot n|, \text{ uniformly on } \mathbb{S}^{d-1}. \tag{4.10}$$

Denoting the cosine transform as $\mathcal{T}$ and taking sum over all directions $\nu \in \mathbb{S}^{d-1}$, we can write the desired surface tension as

$$\gamma(n) = \frac{1}{\sqrt{\pi}} \int_{\mathbb{S}^{d-1}} \omega(\nu)\, |\nu \cdot n|\, d\mathcal{H}^{d-1}(\nu) = \frac{1}{\sqrt{\pi}} \mathcal{T}\omega(\nu). \tag{4.11}$$

The generating function ω can be obtain by solving (4.11):

$$\omega = \sqrt{\pi}(\mathcal{T}^{-1}\gamma). \tag{4.12}$$

Note that $\mathcal{T}^{-1}$ is the inverse cosine transform and ω obtained by (4.12) will be positive as long as Wulff shape of the anisotropy γ is a zonoid [25, 8]. The corresponding kernel can then be written as

$$\begin{aligned} K_\epsilon(x) &= \int_{\mathbb{S}^{d-1}} \omega(\nu)\, g_{\nu,\epsilon}(x)\, d\mathcal{H}^{d-1}(\nu) \\ &= \int_{\mathbb{S}^{d-1}} \sqrt{\pi}(\mathcal{T}^{-1}\gamma)(\nu)\, g_{\nu,\epsilon}(x)\, d\mathcal{H}^{d-1}(\nu). \end{aligned} \tag{4.13}$$

(4.13) represents the general form of the kernel, which is positive in both the physical and Fourier domain. Corresponding mobility of (4.13) can be derived with the help of (3.24) as follows:

$$\begin{aligned} [\mu_\epsilon(n)]^{-1} &= 2\int_{\mathbb{R}} \widehat{K_\epsilon}(n\xi)\, d\xi \\ &= 2\int_{\mathbb{R}} \int_{\mathbb{S}^{d-1}} \sqrt{\pi}(\mathcal{T}^{-1}\gamma)(\nu)\, \widehat{g}_{\nu,\epsilon}(\xi)\, d\mathcal{H}^{d-1}(\nu)\, d\xi \\ &= 2\sqrt{\pi}\int_{\mathbb{S}^{d-1}} (\mathcal{T}^{-1}\gamma)(\nu) \left[\int_{\mathbb{R}} \widehat{g}_{\nu,\epsilon}(\xi)\, d\xi\right] d\mathcal{H}^{d-1}(\nu) \\ &= 2\sqrt{\pi}\int_{\mathbb{S}^{d-1}} (\mathcal{T}^{-1}\gamma)(\nu) \left[\frac{1}{2\sqrt{\pi}\sqrt{(\nu \cdot n)^2(1-\epsilon^2)+\epsilon^2}}\right] d\mathcal{H}^{d-1}(\nu) \quad \text{see (4.9)} \\ &= \frac{1}{\sqrt{\pi}} \int_{\mathbb{S}^{d-1}} (\mathcal{T}^{-1}\gamma)(\nu) \frac{\sqrt{\pi}}{\sqrt{(\nu \cdot n)^2(1-\epsilon^2)+\epsilon^2}}\, d\mathcal{H}^{d-1}(\nu) \\ &= \frac{1}{\sqrt{\pi}} \int_{\mathbb{S}^{d-1}} (\mathcal{T}^{-1}\gamma)(\nu) \frac{1}{\gamma_{\nu,\epsilon}}\, d\mathcal{H}^{d-1}(\nu), \quad \text{using (4.8)} \end{aligned} \tag{4.14}$$

As pointed out earlier, the original paper contains an error, and the above is the corrected formula.

The specific form of the two-dimensional kernel will be required for the upcoming analysis. To get the expression of the kernel in two dimensions, we simplify the generating function as follows,

$$\omega(\nu) = \sqrt{\pi}(\mathcal{T}^{-1}\gamma) = \frac{\sqrt{\pi}}{4}\left[\gamma''(\theta - \frac{\pi}{2}) + \gamma(\theta - \frac{\pi}{2})\right] = \frac{\sqrt{\pi}}{4}\,\text{stiff}\,(\theta), \tag{4.15}$$

where $\nu = (\cos\theta, \sin\theta)$ and we use 'stiff' as an abbreviation of the stiffness term, i.e., stiff$(\theta) = \gamma''(\theta - \frac{\pi}{2}) + \gamma(\theta - \frac{\pi}{2})$. (4.13) and (4.15) allow us to write two-dimensional form of the kernel as below,

$$\begin{aligned}
K_\epsilon(x) &= \int_{\mathbb{S}^1} \omega(\nu)\; g_{\nu,\epsilon}(x)\; d\nu, \\
&= \sqrt{\pi}\int_0^{2\pi} \frac{\text{stiff}(\theta)}{4}\; g_{\nu,\epsilon}(x)\; d\theta \\
&= \sqrt{\pi}\int_0^{2\pi} \frac{\text{stiff}(\theta)}{4}\;\frac{1}{4\pi\epsilon}\exp\left(\frac{-(x\cdot\nu)^2}{4}\right)\exp\left(\frac{(x\cdot\nu)^2 - |x|^2}{4\epsilon^2}\right)\; d\theta \\
&= \frac{1}{16\epsilon\sqrt{\pi}}\int_0^{2\pi} \text{stiff}(\theta)\;\exp\left(\frac{-((x,y)\cdot(\cos\theta,\sin\theta))^2}{4}\right) \\
&\qquad \exp\left(\frac{((x,y)\cdot(\cos\theta,\sin\theta))^2 - x^2 - y^2}{4\epsilon^2}\right)\; d\theta, \\
&= \frac{1}{16\epsilon\sqrt{\pi}}\int_0^{2\pi} \left[\gamma''(\theta - \frac{\pi}{2}) + \gamma(\theta - \frac{\pi}{2})\right] \\
&\qquad \exp\left(\frac{-(x\cos\theta + y\sin\theta)^2}{4}\right)\exp\left(\frac{-(x\sin\theta - y\sin\theta)^2}{4\epsilon^2}\right)\; d\theta. \qquad (4.16)
\end{aligned}$$

Similarly, the Fourier transform is

$$\begin{aligned}
\widehat{K}_\epsilon(\xi) &= \int_{\mathbb{S}^1} \omega(\nu)\; \widehat{g}_{\nu,\epsilon}(\xi)\; d\nu \\
&= \sqrt{\pi}\int_0^{2\pi} \frac{\text{stiff}(\theta)}{4}\; \widehat{g}_{\nu,\epsilon}(\xi)\; d\theta \\
&= \frac{\sqrt{\pi}}{4}\int_0^{2\pi} \text{stiff}(\theta)\;\exp(-4\pi^2(\nu\cdot\xi)^2)\;\exp\left(4\pi^2\epsilon^2\left[(\nu\cdot\xi)^2 - |\xi|^2\right]\right)\; d\theta \\
&= \frac{\sqrt{\pi}}{4}\int_0^{2\pi} \text{stiff}(\theta)\;\exp\left(-4\pi^2\left[(\nu\cdot\xi)^2)(1-\epsilon^2) + \epsilon^2|\xi|^2\right]\right)\; d\theta \\
&= \frac{\sqrt{\pi}}{4}\int_0^{2\pi} \left[\gamma''\left(\theta - \frac{\pi}{2}\right) + \gamma\left(\theta - \frac{\pi}{2}\right)\right] \\
&\qquad \exp\left(-4\pi^2\left[(\xi_1\cos\theta + \xi_2\sin\theta)^2(1-\epsilon^2) + \epsilon^2|\xi|^2\right]\right)\; d\theta. \qquad (4.17)
\end{aligned}$$

Thus, (4.16) and (4.17) give the desired form of the kernel in the respective domain. Corresponding mobility of the EE kernel is given by (4.14), and for the two-dimensional case one can simplify the mobility expression as follows,

$$\begin{aligned}
[\mu_\epsilon(n)]^{-1} &= 2\int_{\mathbb{R}} \widehat{K_\epsilon}(n\xi)\, d\xi \\
&= 2\int_{\mathbb{R}} \sqrt{\pi}\int_0^{2\pi} \frac{\text{stiff}(\theta)}{4}\, \widehat{g}_{\nu,\epsilon}(n\xi)\, d\theta\, d\xi \\
&= 2\sqrt{\pi}\int_0^{2\pi} \frac{\text{stiff}(\theta)}{4}\left[\int_{\mathbb{R}} \widehat{g}_{\nu,\epsilon}(n\xi)\, d\xi\right] d\theta \\
&= 2\sqrt{\pi}\int_0^{2\pi} \frac{\text{stiff}(\theta)}{4} \frac{1}{2\sqrt{\pi}\sqrt{(\nu\cdot n)^2(1-\epsilon^2)+\epsilon^2}}\, d\theta \qquad \text{derivation of (4.9)} \\
\mu_\epsilon(n) &= \left(\frac{1}{4}\int_0^{2\pi} \frac{\gamma''(\theta-\frac{\pi}{2})+\gamma(\theta-\frac{\pi}{2})}{\sqrt{(n_1\cos\theta+n_2\sin\theta)^2(1-\epsilon^2)+\epsilon^2}}\, d\theta\right)^{-1} \qquad (4.18)
\end{aligned}$$

Formula (4.18) indicates that the mobility depends on the regularising parameter ϵ.

In the thresholding algorithm, for the thresholding step, i.e., (3.16), area below the graph of the kernel is needed. To obtain area below the graph of the kernel, the Fourier form of the kernel, i.e., (4.17) can be taken into consideration. Indeed, it is obtained directly by putting $\xi = 0$ in (4.17), i.e.,

$$\widehat{K}(0) = \widehat{K}_\epsilon(0) = \frac{\sqrt{\pi}}{4}\int_0^{2\pi} \left[\gamma''\left(\theta - \frac{\pi}{2}\right) + \gamma\left(\theta - \frac{\pi}{2}\right)\right] d\theta. \qquad (4.19)$$

(4.19) guarantees that the area of the kernel does not change with the choice of ϵ.

EE kernel is positive in both physical domain and Fourier domain, hence proof of convergence and stability is achievable for fixed ϵ. On the other hand, from the practical viewpoint, the computational time required to construct the kernel is excessive because it demands integration at each grid point. Moreover, unchangeable mobility is another drawback of the EE kernel.

We conclude EE kernel section by summarizing the compatibility of a kernel with stability and convergence in the following theorem:

Theorem 4.1.2. *If γ is non-negative, even, strictly convex anisotropy and $\gamma(x) > 0$ for all $x \in \mathbb{R}^d$,*

(i) then the above construction gives a kernel, which is positive in Fourier domain; further, these kernels satisfy all the conditions required for stability of Algorithm 4, i.e., Proposition 3.3.3.

(ii) Further, if corresponding Wulff shape $\mathcal{W}_\gamma$ is a zonoid, then the construction of kernel, which is positive in physical domain, is possible. These kernels satisfy all the conditions

given in convergence theorem 3.3.1.

4.1.3 Esedoglu–Jacobs–Zhang kernel, positive in physical domain (EJZ)

Esedoglu, Jacobs and Zhang developed a most general form of kernels in [30]. The authors construct a positive kernel in the real domain for two and three dimensions. However, since in this work we focus on the two-dimensional problem, only details of the two-dimensional kernel are given below.

To begin with, let us introduce a few assumptions and terminologies. Spherical Radon transform $\mathcal{J}_s$ of an even function f is defined as

$$\mathcal{J}_s f(n) = \int_{\mathbb{S}^{d-1} \cap n^{\perp}} f(x)\, d\mathcal{H}^{d-1}(x).$$

Further, we define a compactly supported, smooth positive bump function $\eta : \mathbb{R} \to \mathbb{R}$ by

$$\eta(x) = \begin{cases} e^{\frac{-1}{x^2(x-2)^2}} & \text{if } x \in (0,2) \\ 0 & \text{otherwise,} \end{cases} \tag{4.20}$$

and its moments are denoted as

$$m_j = \int_0^2 x^j \eta(x)\, dx, \qquad j \in \mathbb{N}^+.$$

The authors proved the existence of a kernel as presented in the following proposition. Note that their kernel formula contains an error; therefore, we give a detailed proof.
Proposition 4.1.3. *[30] Let γ and μ satisfy*

- *B_γ is strongly convex and ∂B_γ is smooth,* (4.21)
- $\mu : \mathbb{S}^1 \to \mathbb{R}^+ \backslash \{0\}$, (4.22)

then, there exist a positive, smooth, compactly supported convolution kernel $K : \mathbb{R}^2 \to \mathbb{R}^+$ such that $\gamma_K = \gamma$ and $\mu_K = \mu$.

Proof. For a given kernel K, corresponding anisotropy γ_K and mobility μ_K can be given as (3.27) and (3.25). As done in [25], for $d = 2$, we considered a polar form of (3.25) and

(3.27), then use (4.12) to get the generating function and mobility in the following form,

$$\begin{aligned} \omega(n) &= \frac{1}{2}\int_0^\infty K(rn)\, r^d\, dr, \\ \frac{1}{2\mu(n)} &= \mathcal{J}_s \int_0^\infty K(rn)\, dr. \end{aligned} \tag{4.23}$$

Let the kernel K have a polar form

$$K(r,\theta) = \alpha(\theta)\cdot\eta(r\beta(\theta)), \tag{4.24}$$

where $\alpha, \beta : \mathbb{R} \to \mathbb{R}^+$ are π- periodic, smooth functions. Substitute (4.24) into (4.23) to get

$$\begin{aligned} 2\omega(\theta) &= \int_0^\infty \alpha(\theta)\cdot\eta(r\beta(\theta))\, r^d\, dr \\ \frac{\text{stiff}(\theta)}{2} &= \alpha(\theta)\int_0^\infty \eta(x)\left[\frac{x}{\beta(\theta)}\right]^d \frac{dx}{\beta(\theta)}, \qquad x = r\beta(\theta) \\ &= \frac{\alpha(\theta)}{\beta(\theta)^3}\int_0^\infty \eta(x)\, x^2\, dx = \frac{\alpha(\theta)}{\beta(\theta)^3}\int_0^2 \eta(x)\, x^2\, dx, \quad d = 2 \\ &= \frac{\alpha(\theta)}{\beta(\theta)^3} m_2. \end{aligned} \tag{4.25}$$

Similarly, for the second expression in (4.23),

$$\begin{aligned} \mathcal{J}_s^{-1}\left(\frac{1}{2\mu(\theta)}\right) &= \int_0^\infty \alpha(\theta)\cdot\eta(r\beta(\theta))\, dr \\ \frac{1}{2}\mathcal{J}_s^{-1}\left(\frac{1}{\mu(\theta)}\right) &= \alpha(\theta)\int_0^\infty \eta(x)\,\frac{dx}{\beta(\theta)} \\ \frac{1}{2}\cdot\frac{1}{2\mu(\theta-\pi/2)} &= \frac{\alpha(\theta)}{\beta(\theta)} m_0. \end{aligned} \tag{4.26}$$

Both (4.25) and (4.26) lead to the following solution,

$$\begin{aligned} \beta(\theta)^2 &= \frac{\alpha(\theta)}{\beta(\theta)}\frac{2m_2}{\text{stiff}(\theta)} \\ &= \frac{1}{4m_0\mu(\theta-\pi/2)}\cdot\frac{2m_2}{\text{stiff}(\theta)}, \\ &= \left[\frac{m_2}{2m_0}\cdot\frac{1}{\mu(\theta-\pi/2)\left[\gamma''(\theta-\frac{\pi}{2})+\gamma(\theta-\frac{\pi}{2})\right]}\right]^{\frac{1}{2}}.\beta(\theta) \end{aligned} \tag{4.27}$$

$$\begin{aligned}\alpha(\theta) &= \frac{\beta(\theta)}{4m_0\mu(\theta-\pi/2)} \\ &= \left[\frac{m_2}{32m_0^3}\cdot\frac{1}{\mu^3(\theta-\pi/2)\left[\gamma''(\theta-\frac{\pi}{2})+\gamma(\theta-\frac{\pi}{2})\right]}\right]^{\frac{1}{2}}. \qquad (4.28)\end{aligned}$$

(4.24), (4.27) and (4.28) give the desired output. □

Since the EJZ kernel is positive in the physical domain, the convergence of the algorithm is guaranteed. On the other hand, the kernel may be negative in the Fourier domain; thus, stability is uncertain. However, one can freely choose mobility during the kernel construction, which makes EJZ kernel the most general among all other kernels.

We conclude EJZ kernel section by summarizing the convergence result as follows:
Theorem 4.1.4. *If γ is non-negative, even, strictly convex anisotropy and $\gamma(x) > 0$ for $x \neq 0$, then the above construction gives a kernel in two dimensions, which is positive in the physical domain. Further, it satisfies all the conditions given in convergence theorem 3.3.1.*

4.1.4 Esedoglu–Jacobs–Zhang kernel, positive in Fourier domain (EJZ-F)

Authors of [30] developed another kernel in the same paper. To construct the kernel, they assume exponential form of the kernel and solve (3.23) and (3.24). The authors proved the existence of the kernel in the following proposition. Here too, we found an error; therefore, detailed derivation is presented.
Proposition 4.1.5. *[30] Let γ and μ satisfy* (4.21) *and* (4.22) *then, there exist a convolution kernel $K : \mathbb{R}^d \to \mathbb{R}$ in Schwartz class with $\widehat{K} \geqslant 0$ and a constant $c > 0$ such that $\gamma_K = \gamma$ and $\mu_K = c\mu$.*

Proof. The ansatz is,

$$\widehat{K}(\xi) = \frac{1}{2}\exp(-\zeta(\alpha(\xi))) + \frac{1}{2}\exp(-\zeta(\beta(\xi))), \qquad (4.29)$$

where $\zeta : \mathbb{R} \to \mathbb{R}$ is a positive, smooth and even function satisfying $\zeta(x) = 0$ if $|x| \leqslant 1$ and $\zeta(x) = x^2$ if $|x| \geqslant 2$ and $\alpha, \beta : \mathbb{R}^d \to [0, \infty)$ are one homogeneous functions. Desired kernel is derived by solving (3.23) and (3.24); therefore we substitute (4.29) in those equalities, which leads to the following;

$$\begin{aligned}
-4\pi^2\gamma(n) &= \int_{\mathbb{R}} \frac{\widehat{K}(n\xi) - \widehat{K}(0)}{\xi^2}\, d\xi \\
&= \int_{\mathbb{R}} \frac{\frac{1}{2}\exp^{-\zeta(\alpha(n\xi))} + \frac{1}{2}\exp^{-\zeta(\beta(n\xi))} - 1}{\xi^2}\, d\xi \\
&= \frac{1}{2}\int_{\mathbb{R}} \frac{\exp^{-\zeta(\alpha(n\xi))} - 1}{\xi^2}\, d\xi + \frac{1}{2}\int_{\mathbb{R}} \frac{\exp^{-\zeta(\beta(n\xi))} - 1}{\xi^2}\, d\xi \\
&= \frac{\alpha+\beta}{2}\int_{\mathbb{R}} \frac{\exp^{-\zeta(y)} - 1}{y^2}\, dy \\
8\pi^2\gamma(n) &= 4\pi(\alpha+\beta)S_2, \quad \text{where } S_2 = \frac{1}{4\pi}\int_{\mathbb{R}} \frac{1 - \exp^{-\zeta(y)}}{y^2}\, dy \\
b &= \alpha+\beta, \qquad \text{where } b = 2\pi\gamma(n)/S_2. \qquad (4.30)
\end{aligned}$$

Similarly, substitution of (4.29) in (3.24) results in

$$\begin{aligned}
\frac{c}{2\mu(n)} &= \int_{\mathbb{R}} \widehat{K}(n\xi)\, d\xi \\
&= \int_{\mathbb{R}} \frac{1}{2}\exp^{-\zeta(\alpha(n\xi))} + \frac{1}{2}\exp^{-\zeta(\beta(n\xi))}\, d\xi \\
&= \left(\frac{1}{2\alpha} + \frac{1}{2\beta}\right)\int_{\mathbb{R}} \exp^{-\zeta(y)}\, dy \\
&= 4\pi\left(\frac{1}{2\alpha} + \frac{1}{2\beta}\right)S_0, \quad \text{where } S_0 = \frac{1}{4\pi}\int_{\mathbb{R}} \exp^{-\zeta(y)}\, dy \\
a &= \left(\frac{1}{\alpha} + \frac{1}{\beta}\right), \qquad \text{where } a = \frac{c}{S_0 4\pi\mu(n)} \qquad (4.31)
\end{aligned}$$

(4.30) and (4.31) lead to a simple quadratic equation for α and β. Constant $c > 0$ has been introduced to ensure that the quadratic equation possesses real roots. Two solutions of the quadratic equation are

$$\alpha(n) = \frac{\pi}{S_2\sqrt{c}}\left(\sqrt{c}\gamma + \sqrt{c\gamma^2 - 8S_0S_2\mu\gamma}\right), \qquad (4.32)$$

$$\beta(n) = \frac{\pi}{S_2\sqrt{c}}\left(\sqrt{c}\gamma - \sqrt{c\gamma^2 - 8S_0S_2\mu\gamma}\right). \qquad (4.33)$$

We see that we need to take $c \geqslant 8S_0S_2\mu(n)/\gamma(n)$ for all n, so that α, β are real. □

This kernel is positive in the Fourier domain hence guarantees the stability of the corresponding algorithm.

Theorem 4.1.6. *If γ is strictly convex anisotropy then above construction gives a kernel in Schwartz class, which is positive in Fourier domain; further, these kernels satisfy all the conditions required for stability of Algorithm 4, see Proposition 3.3.3.*

EJZ-F kernel may change the sign in physical domain, and thus authors could not give the proof of convergence.

This kernel is a modification of BBC kernel [9] with the purpose of eliminating the singularity of the Fourier transform of BBC kernel which may appear at the origin for certain anisotropies, and thus improving decay properties of the kernel that are important for numerical efficiency. Moreover, the EJZ-F kernel allows for a free choice of mobility μ, unlike the BBC kernel. The corresponding mobility of the EJZ-F kernel differs by a factor c, i.e., we can obtain only a multiple of the desired mobility, but this has no impact on the solution as it only scales time.

4.2 Comparison of kernels

This section aims to investigate the properties of the kernels introduced above from the numerical point of view. The motivation comes from the fact that although the general theory of convergence and stability is presented in Chapter 3, there is no systematic comparison of the numerical performance of convolution kernels in the literature. This kind of analysis is important to decide which kernel is suitable for a particular problem/anisotropy; in particular, it will direct our choice of the kernel for the obstacle problem in the following chapter. Therefore we do a comparison analysis with the following criteria in mind:

- Behaviour of error and convergence order.
- Time required for computation.
- Ability to handle sharp corners.
- Evolution of non-convex shapes.

Regarding convergence order, its theoretical predicted value is one as shown in Proposition 3.3.5, and we confirm in our numerical tests that it is indeed so also practically. We choose a well behaved elliptic anisotropy to investigate the error, convergence order, and computational time. We use natural mobility, so that the solution is self-similar and analytical solution is available.

Further, to check the ability of the kernels to handle corners, we choose the crystalline anisotropy, where Wulff shape has sharp corners. To investigate the behaviour of the kernel with a non-convex shape, we start the evolution with an S-shaped initial condition and test the numerically obtained evolution against an accurate front tracking solution. The findings on properties of all kernels are summarized in tabular form.

We use Algorithm 4 (see Section 3.3) and its modified version for area-preserving flows to perform the above mentioned numerical tests. These algorithms consist of two essential steps, namely convolution and thresholding. In the numerical tests, the convolution $K_{\delta t} * 1_P$ is calculated with the help of Fast Fourier Transform (FFT), yielding

$$\widehat{U}^k = \widehat{K}_{\delta t} \widehat{1}_{P^k}, \tag{4.34}$$

and then taking the inverse transform to get U^k. Spatial variables are discretized on a rectangular grid with grid cells of size $dx \times dy$. In the thresholding step, the value at each grid point of the diffused function U^k is replaced with 0 or 1 to obtain numerical solution U^{k+1} at next time step.

If the value of U^k at a grid point is greater than half of the area under the kernel, then the value 1 is assigned, otherwise 0. This procedure of rearranging the values leads to a characteristic function, which becomes the input for the next time step. However, this simple thresholding approach leads to non-smooth behaviour of errors. To avoid this unwanted behaviour, the idea of sub-grid spatial accuracy is implemented in the numerical code; see Appendix A.5 for details.

4.2.1 Anisotropy with smooth Wulff shape

Here we perform the first comparison test to investigate the error, convergence order and computational time. All tests are carried out in two dimensions. To make this test fair, all the parameters, i.e., anisotropy, mobility, initial condition and final time, are taken identical for each kernel.

In order to satisfy the assumptions needed for convergence and/or stability of the thresholding scheme, we choose an elliptic anisotropy, i.e., $\gamma(x, y) = \sqrt{(ax)^2 + (by)^2}$ with $a = 2$, $b = 1$. Wulff shape corresponding to this anisotropy is given by $x^2 + \left(\frac{y}{2}\right)^2 = 1$.

One can easily observe that the selected anisotropy is one-homogeneous, and the corresponding Wulff shape is centrally symmetric, thus a zonoid.

We have the liberty to choose any mobility, except for BBC and EE kernels. BBC kernel has fixed natural mobility, i.e., $\mu = \gamma$, and therefore, we select natural mobility for all the kernels during the numerical tests. However, EE kernel's mobility is fixed to a different value and thus we need to treat this case separately.

We assigned the Wulff shape of the chosen anisotropy as initial condition. This particular choice of mobility and initial condition leads to the analytical solution, known as *self-similar solution* [74]. The setup of the test is summarized as follows:

$$\begin{aligned} &\text{anisotropy: } \gamma(x,y) = \sqrt{(2x)^2 + y^2}, && \text{mobility: } \mu = \gamma, \\ &\text{Wulff shape } \mathcal{W}_\gamma : x^2 + \left(\frac{y}{2}\right)^2 = 1, && \text{initial condition : } \Gamma_0 = \mathcal{W}_\gamma. \end{aligned} \tag{4.35}$$

Analytical solution

Analytical solution of this problem is known as *self-similar solution*, i.e., initial Wulff shape shrinks in size without changing its shape [74, 66]. Since the shape is preserved, the only task is to find the speed of the shrinking Wulff shape. Below, we derive the analytical solution.

Consider a Wulff envelope as $W_\gamma(\theta,t) = \eta(t)W_\gamma(\theta,0)$ and notice that by construction we have $W_\gamma(\theta,t) \cdot n(\theta) = -\gamma(\theta)$, where n is the unit normal. Moreover, the anisotropic curvature $(\gamma + \gamma'')\kappa$ is equal to 1 for the Wulff envelope $W_\gamma(\theta,0)$ and scales as $1/\eta(t)$ for $W_\gamma(\theta,t)$. Hence, normal velocity formula gives the following expression:

$$V = \partial_t W_\gamma \cdot n = \partial_t \eta(-\gamma) = \gamma(\gamma + \gamma^{''})\kappa = \gamma/\eta,$$

which leads to a simple ODE $\partial_t \eta = -1/\eta$. Solving the ODE for $\eta(t)$ with initial condition $\eta(0) = 1$, yields,

$$W_\gamma(\theta,t) = \sqrt{1-2t}\ \ W_\gamma(\theta,0), \qquad t \in (-\infty, \tfrac{1}{2}]. \tag{4.36}$$

The solution vanishes at time $t = \frac{1}{2}$; which is also known as extinction time. For the analysis, we evolve the initial Wulff shape until half time to extinction, i.e., $t = \frac{1}{4}$ and call this time "final time".

We present self similar solution based on (4.36) in Figure 4.1. Numbers in the inset indicate time. As announced earlier, ellipse is decreasing in size while preserving its shape.

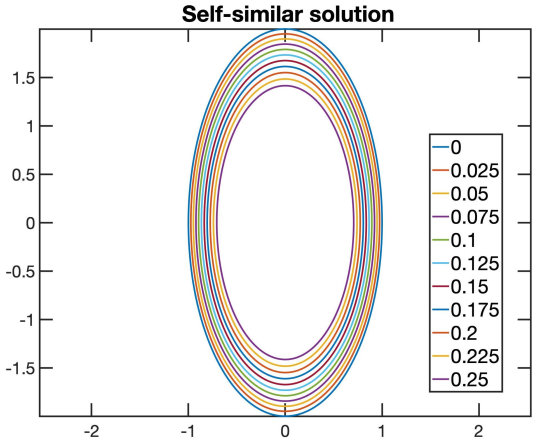

Figure 4.1: Self similar solution of the problem (4.35) given in Section 4.2.1

Front tracking solution

We have derived an analytical solution for the problem with natural mobility. However, EE kernel possesses a different mobility, i.e., (4.14) and, therefore, the above derived analytical solution does not apply to the EE kernel. Since the analytical solution for the mobility (4.14) is not available, we use an accurate numerical approximation of the analytical solution, known as *front tracking solution*, from [66], see Appendix A.6.

Error

For the convergence analysis, we chose the $L_t^\infty(L_x^1)$-norm to measure error. To understand the meaning of this error, we look at the error in two steps. In the first step, compute the spatial error by L^1-norm, i.e., the difference of the subgrid-accurate characteristic function of numerical solution and the subgrid-accurate characteristic function of the analytical solution at each time step, until the overall time reaches the final time, i.e., 0.25. In the second step, choose the maximum among those. The explicit definition of the error is given as,

$$L_t^\infty(L_x^1) \text{ norm} = L_t^\infty\left(\int \left|1_{U_A^k} - 1_{U^k}\right| dx\right) = \max_{t_k \in [0,0.25]}\left(\int \left|1_{U_A^k} - 1_{U^k}\right| dx\right), \quad (4.37)$$

where $1_{U_A^k}$ is subgrid-accurate characteristic function of the analytical solution at time t_k, and similarly 1_{U^k} is subgrid-accurate characteristic function of the numerical solution at timestep k. In the numerical tests, we noticed that the L^1-norm of the spatial errors increased with the time; therefore, the maximum over time was attained at the final time. Due to this fact, one can save the computation time by calculating errors near the final time only.

In the case of EE kernel, extinction time is different from 0.25 because of different mobility. Moreover, extinction time varies with the value of regularizing parameter, i.e., ϵ. We choose three different values of ϵ(namely, $0.01, 0.05$ and 0.1) to study the numerical behavior and determine the final time as an approximate half time to extinction.

Numerical results

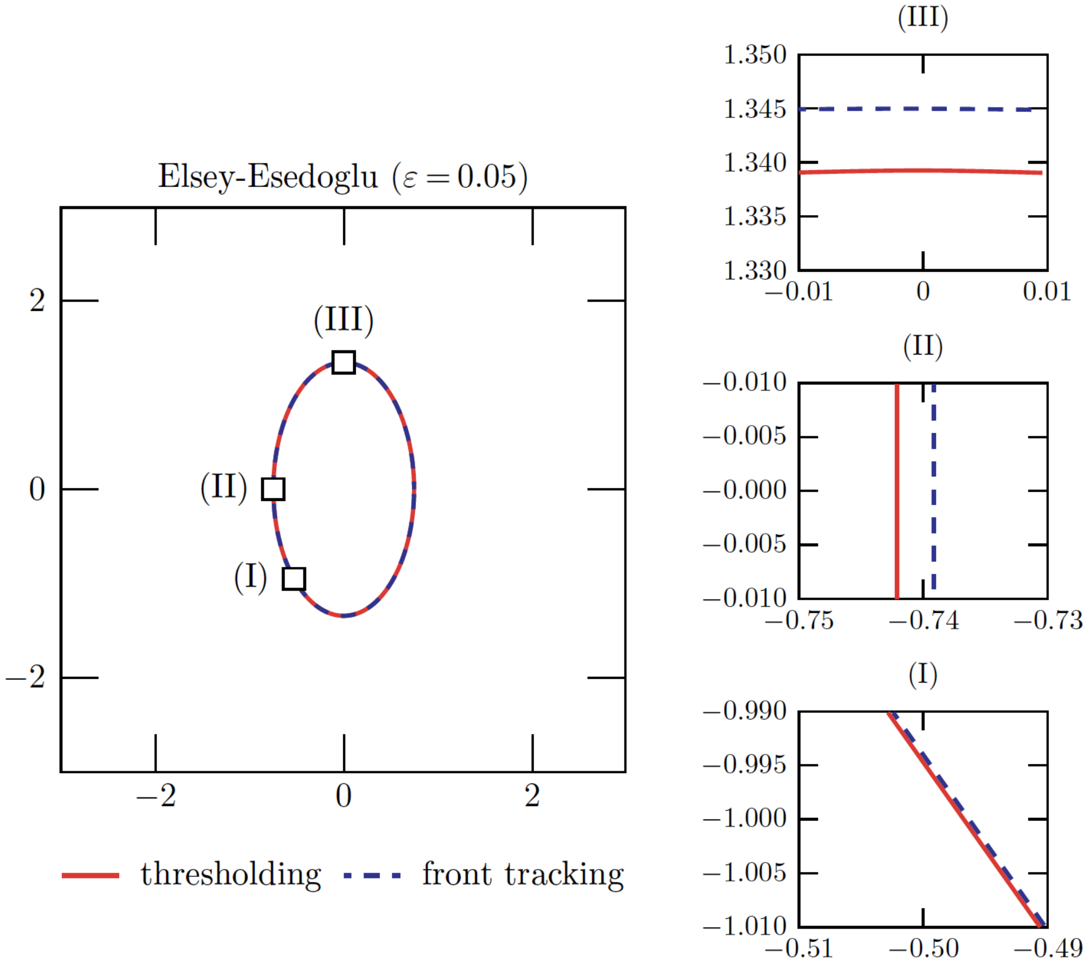

Figure 4.2: Figure on bottom right depicts the comparison with front-tracking solution at half-time to extinction

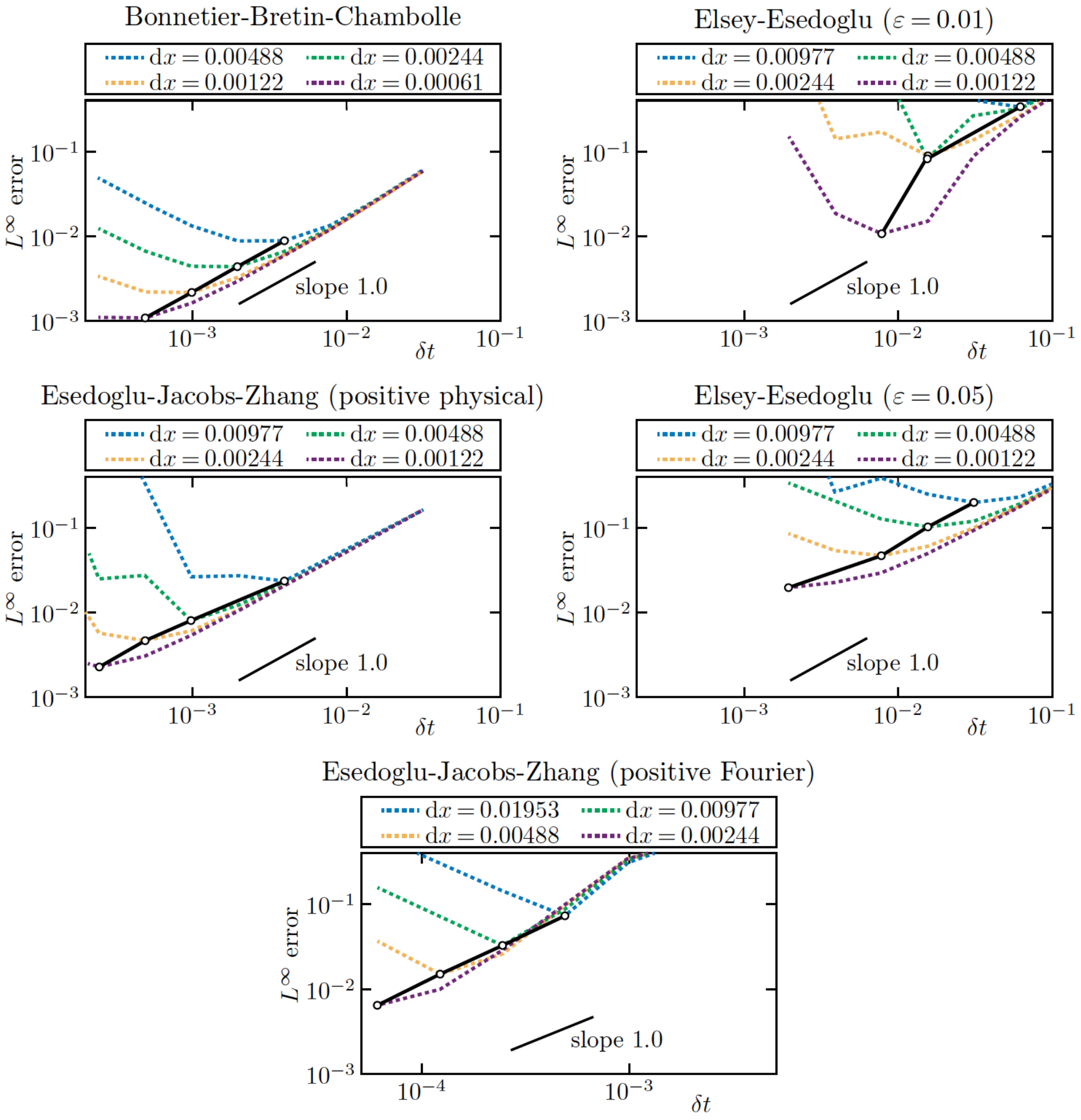

Figure 4.3: Log-log plots of the dependence of numerical error on time step δt for various mesh refinements dx and for each kernel. Black points indicate the optimal dx-δt pair for each value of dx.

For the numerical analysis, we evolve the Wulff shape of an elliptic anisotropy using Algorithm 4 until final time, i.e., half time to extinction. These computations were done using Matlab software on four cores of 3.7GHz Intel Xeon E5 processors of a Mac Pro workstation. The resulting errors, convergence rates and CPU times are presented in Table 4.1, Figures 4.2 and 4.3.

For all the kernels, first immediate observation is that the thresholding scheme possesses the expected (theoretical) first-order convergence order in time. This observation is made

Bonnetier-Bretin-Chambolle kernel ($dx = 0.00061$, $N = 2^{14}$)

Time step δt	0.03125	0.01562	0.00781	**0.00390**	0.00195	0.00097
L^∞-error	0.05836	0.02564	0.01207	**0.00589**	0.00297	0.00161
Convergence order	-	1.19	1.09	**1.04**	0.99	0.88
CPU time (min)	14	28	57	**113**	227	453

Esedoglu-Jacobs-Zhang kernel: positive in Fourier ($dx = 0.00061$, $N = 2^{14}$)

Time step δt	**0.00390**	0.00195	0.00097	0.00048	0.00024	0.00012
L^∞-error	**0.64610**	0.54342	0.35265	0.09938	0.02964	0.01246
Convergence order	**-**	0.25	0.62	1.82	1.75	1.25
CPU time (min)	**25**	47	95	191	382	760

Esedoglu-Jacobs-Zhang kernel: positive in physical ($dx = 0.00122$, $N = 2^{13}$)

Time step δt	0.01562	0.00781	**0.00390**	0.00195	0.00097	0.00048
L^∞-error	0.08137	0.04094	**0.02058**	0.01041	0.00540	0.00308
Convergence order	-	0.99	**0.99**	0.99	0.95	0.80
CPU time (min)	7	13	**26**	53	106	212

Elsey-Esedoglu kernel: $\varepsilon = 0.1$ ($dx = 0.00122$, $N = 2^{13}$)

Time step δt	0.12500	0.06250	0.03125	0.01562	0.00781	**0.00390**
L^∞-error	0.34198	0.20097	0.13425	0.10275	0.08994	**0.08240**
Convergence order	-	0.77	0.58	0.39	0.19	**0.13**
CPU time (min)	7	13	27	53	107	**213**

Elsey-Esedoglu kernel: $\varepsilon = 0.05$ ($dx = 0.00122$, $N = 2^{13}$)

Time step δt	0.12500	0.06250	0.03125	0.01562	0.00781	**0.00390**
L^∞-error	0.36138	0.17987	0.09401	0.05003	0.02953	**0.02281**
Convergence order	-	1.01	0.94	0.91	0.76	**0.37**
CPU time (min)	8	18	36	70	133	**265**

Elsey-Esedoglu kernel: $\varepsilon = 0.01$ ($dx = 0.00122$, $N = 2^{13}$)

Time step δt	0.12500	0.06250	0.03125	0.01562	0.00781	**0.00390**
L^∞-error	0.56472	0.25302	0.08831	0.01503	0.01067	**0.01866**
Convergence order	-	1.15	1.51	2.55	0.49	**-0.80**
CPU time (min)	10	20	41	84	166	**329**

Table 4.1: Results of numerical tests for selected mesh sizes dx and corresponding number of grid points N. Highlighted columns show results for the common value of $\delta t = 0.0039$.

based on the fact that for fixed mesh size dx, and corresponding optimal diffusion time δt (black circles in Figure 4.3), the line (see black line in Figure 4.3) joining these points points has slope close to one. Here, optimal diffusion time means the value δt, which gives the least error among all available δt. BBC and EJZ-F kernels are positive in the Fourier domain, and their convergence rate is slightly greater than one.

Further, the error shows a typical V-shape phenomenon, i.e., error decreases with decreasing time-step until it attains minimum, and then it increases for further smaller δt. The V-shape phenomenon occurs because, for sufficiently small δt, the thresholding algorithm cannot move the interface by more than a single grid cell. Thus, the interface gets stuck and does not properly evolve with time, yielding larger errors. Details about the V-shape phenomenon are explained in [60]. Overall performance of BBC and EJZ kernels are better than the EE and EJZ-F kernels. The highlighted grey columns in Table 4.1, represent results for fixed time step $\delta t = 0.0039$. BBC kernel gives the least error among all kernels. For the EE kernel, as explained in [25], numerical solution gets closer to analytical solution as regularizing parameter $\epsilon \to 0$.

To investigate the required computational time, we calculate the CPU time for each kernel as shown in Table 4.1. BBC kernel is dominating the CPU time criteria by showing the least numbers among all kernels. Note that the CPU time presented in the table does not include time required for kernel construction. This is important for EE kernel, whose construction demands integration at each grid point, hence leading to significantly larger CPU times. If one considers the kernel construction time too, the CPU time comparison would be biased. Moreover, it is computationally more efficient to have an explicit form of Fourier transform of the kernel since it saves one FFT calculation in (4.34).

On the other hand, although the EJZ kernel is given in the physical domain, it is still effective in terms of CPU time. The convergence order of EE kernel strongly depends on the regularization parameter ϵ. We observed that for each choice of ϵ, there is a value in time step δt below which the convergence order starts deteriorating (see EE kernel with different values of ϵ in Table 4.1). Further, EE kernels are time-consuming in terms of construction because they demand a convolution at each grid point.

Upon investigating CPU time, errors, the time required to construct the kernel, and behaviour of convergence order, we conclude that the BBC kernel outperforms the other kernels.

4.2.2 Non-convex initial condition

In the previous test, we used a convex initial condition. It is of interest to investigate the behaviour of the thresholding method and kernels when nonconvex initial condition is

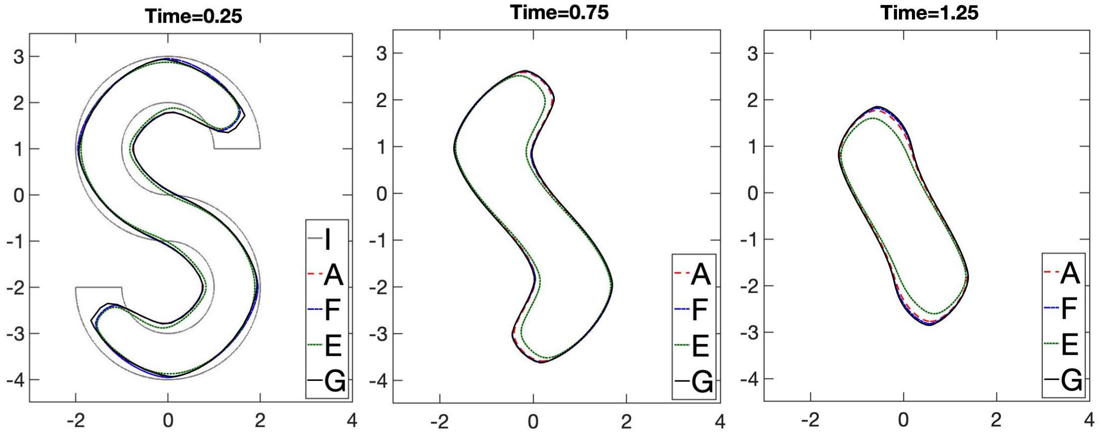

Figure 4.4: Results of applying the thresholding method to S-shaped nonconvex initial condition. Here $dx = 0.0012$ and $\delta t = 0.000488$. **A**: BBC kernel, **E**: EJZ kernel (positive in Fourier domain), **F**: EJZ kernel (positive in physical domain), **G**: Front tracking solution, **I**: Initial shape.

prescribed. We carried out a test with an S-shaped initial condition, see 'I' in Figure 4.4 (left).

The setup for this test is the same as previous test except for anisotropy and initial condition. We choose four-fold weakly anisotropy $\gamma(\theta) = 1 + 0.05 \cos 4\theta$ with natural mobility, i.e., $\mu = \gamma$ and initial condition is S-shaped. Mobility of EE kernel is fixed and not equal to natural mobility; therefore, EE kernel is excluded from this test. Numerical solutions obtained for each kernel were compared against an accurate approximation of the analytical solution obtained by the anisotropic front-tracking method with automatic point redistribution [66]. The front tracking method is the same as the one used in the previous section. In the front tracking, we used 102 points to discretize the curve.

Scrutinizing numerical solutions with front tracking solutions at different times (see Figure 4.4) leads to the conclusion that all three kernels, i.e., BBC, EJZ and EJZ-F show an excellent agreement with the front tracking solution.

4.2.3 Crystalline anisotropy

So far, we have investigated the numerical behaviour of kernels for smooth anisotropies. However, one type of anisotropy is critically important from the application perspective, namely, the crystalline anisotropy. Recall that anisotropy is called crystalline if the corresponding Wulff shape is a polytope. We perform a comparison test on crystalline anisotropy. The prime objective of this test is to see the effect of each kernel at the corners of the polytope. In order to avoid shrinking of the solution and thus be able to observe the evolution at corners, we changed the original thresholding algorithm so that the new algorithm preserves the area of initial condition. Details of the changes are explained in the following subsection.

Area constraint algorithm

To prevent shrinking in the algorithm, one can follow section 3.2, which deals with the volume-preserving isotropic case. The volume constraint demands change in the thresholding step in the original algorithm, i.e., Algorithm 4, which is then updated as follows:

Algorithm 5 Anisotropic BMO algorithm with volume constraint

Given a time step δt and a particle region $P^k \subset \mathbb{R}^d$ at time t_k, to get new region P^{k+1} at next time step $t_{k+1} = t_k + \delta t$, perform the following two steps:

$$\text{Convolution:} \qquad U^k = K_{\delta t} * 1_{P^k} \tag{4.38}$$

$$\text{Thresholding:} \qquad P^{k+1} = \left\{x \mid \; U^k(x) \leqslant \delta^k\right\} \tag{4.39}$$

Here δ^k is chosen so that the area of phase P^{k+1} is equal to the area of phase P^0.

Numerical test

To scrutinize the behaviour at the corners, consider a crystalline anisotropy $\gamma(x, y) = |x| + |y|$, which gives the square as Wulff shape. Set circle as an initial condition and evolve it by area-preserving anisotropic mean curvature flow according to Algorithm 5 until no change is observed between subsequent time steps. We are interested to see the effect at the corners of the numerical equilibrium shape; therefore, any value of mobility is okay for the task. BBC kernel has natural mobility, and we fixed the natural mobility for EJZ kernel and EJZ-F kernel too. As already mentioned, EE kernels have their own fixed mobility, i.e., (4.14).

For EE kernel, we considered three different regularizing parameters ϵ, as in Section 4.2.1. On the other hand, EJZ kernel requires smooth anisotropy. Therefore, we regularize the original anisotropy as follows,

$$\gamma(x, y) \approx \gamma_\delta(x, y) = \sqrt{\delta^2 + x^2} + \sqrt{\delta^2 + y^2} \quad \text{where, } \delta = 0.01.$$

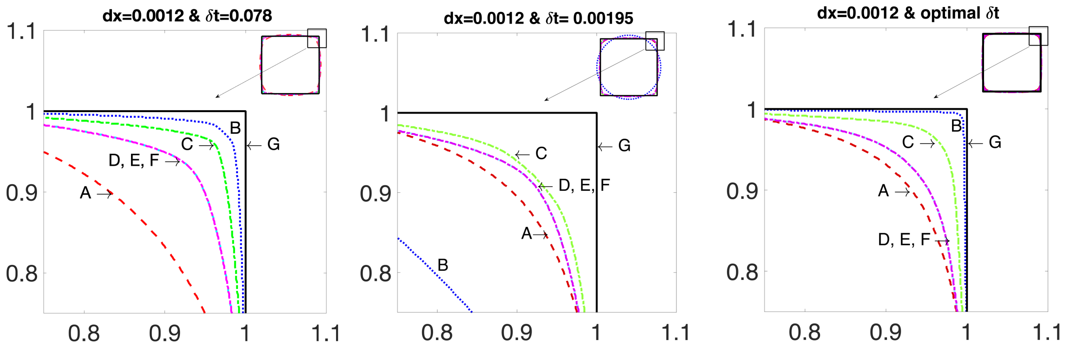

Figure 4.5: Capability of thresholding kernels to approximate crystalline Wulff shapes. **A**: BBC kernel, **B**: EE kernel ($\epsilon = 0.01$), **C**: EE kernel ($\epsilon = 0.05$), **D**: EE kernel ($\epsilon = 0.1$), **E**: EJZ kernel (positive in Fourier domain), **F**: EJZ kernel (positive in physical domain), **G**: Exact solution.

After implementing Algorithm 5, we obtain numerical results, depicted in Figure 4.5. The whole solution is shown in the top-right corner, and a zoom-in in the centre to clearly see one of the corners. Since Wulff shape is symmetric, it is enough to look at one corner only. All the figures have the same space grid size dx. The left and middle plots show the result for fixed dx–δt pair. The right-side figure shows the result for the optimal value of δt chosen for each kernel; therefore, δt has a different value for each kernel. Here, optimality means that δt gives the least error for the given dx.

One can immediately observe that all the kernels smooth out the corners, but BBC kernel's smoothening is excessive. We tried different anisotropy with octagon as a Wulff shape to confirm the excessive smoothening behaviour of BBC kernel. We also noticed the same problem in that example; hence, it becomes clear that the BBC kernel is not an ideal choice for crystalline anisotropies. On the other hand, EE kernel shows the opposite behaviour to BBC kernel. EE kernel gives better and better results as regularising parameter ϵ converges to zero; a fact already mentioned in [25].

Surprisingly, both EJZ and EJZ-F kernel gave almost identical results, and their performance lies in between EE and BBC kernel. Moreover, EE kernel with a comparatively large regularizing parameter $\epsilon = 0.1$ gives the same result as EJZ and advantage of EJZ-F kernel is that it does not have a singularity at the origin like the BBC kernel for the chosen anisotropy, thus EJZ-F is expected to yield better results than BBC kernel. Both EJZ and EJZ-F kernels give the same result, while the time to construct the EJZ-F kernels is slightly greater than its counterpart. On the other hand, the Fourier form of EJZ-F kernel saves one step in the convolution, as mentioned earlier, leading to a supremacy of the EJZ-F kernel. One can also notice that refinement of time step δt does not necessarily lead to a better result since the interface may ”get stuck” for small δt. It can be observed by checking the left and middle figure for the EE kernel with $\epsilon = 0.01$.

4.2.4 Summary of kernel comparison

Kernel	**BBC**	**EE**	**EJZ**	**EJZ-F**
positive in physical domain?	may not	yes	yes	may not
positive in Fourier domain?	yes	yes	may not	yes
Mobility	Natural mobility ($\mu = \gamma$)	Fixed mobility see (4.14)	Can be chosen freely	Can be chosen freely

Limitations

BBC	• Excessive smoothening leads to mishandling of crystalline anisotropies. • Slow decay rate for anisotropies not having ellipsoid as Wulff shape. • Kernel may change sign in the physical domain. • Mobility is fixed to natural mobility.
EE	• Regularizing parameter ϵ has significant influence on the outcome. • Kernel construction (computationally) very expensive. • Mobility is fixed to an unnatural form.
EJZ-F	• Kernel may change sign in the physical domain.
EJZ	• Kernel may change sign in the Fourier domain.

Table 4.2: Summary of properties of four types of kernels.

Chapter 5

Obstacle problem

This chapter introduces the obstacle problem as a natural extension of the two-phase case to a three-phase case, where one phase, i.e., the substrate, is fixed. The additional phase gives rise to triple junction points, i.e., points where three interfaces meet. Since these points change position during the evolution and also the boundary condition is time-dependent, finding a solution to the three-phase problem becomes a non-trivial problem.

One fixed phase with two deformable phases is one of physical interpretations to considering (solid) particle in vapour on a fixed substrate. Thus, obstacle problems have many real-life applications; for example, in coating techniques such as thermal spraying, it is important to predict the dynamics of spreading of impinging particles [7]. Likewise, in the manufacturing of nanopatterned substrates, the precise control of the size and location of forming nanoparticles is essential to boost the functionality of the product [44].

In this chapter, first, we present details of problem setup. Then a thresholding scheme is developed to solve the evolution problem, and numerical properties of each kernel (presented in the previous chapter) are checked via various numerical tests. Finally, a modified scheme is proposed to improve the accuracy at contact points.

5.1 Formulation of the problem

Consider a particle P on a rigid substrate S surrounded by a vapour region V, where P, S, V are taken as closed sets (see Figure 5.1). The objective is to study the evolution of the particle and its equilibrium shape. Therefore we choose a bounded domain $\Omega \subset \mathbb{R}^d$

that is large enough so that there is no contact between particle and boundary of the domain, and thus no influence on the evolution of the particle.

We introduce some more notation. Denote the upper part of the domain as $\Omega^{\text{up}} := P \cup V = \overline{\Omega \backslash S}$. Three interfaces are present in the system, i.e., $\Gamma_{SP} = S \cap P, \Gamma_{SV} = S \cap V$ and $\Gamma = \Gamma_{PV} = P \cap V$, which represent the interface between substrate–particle, substrate–vapor and particle–vapor, respectively. Surface energies of each interface are denoted by γ_{SP}, γ_{SV} and γ_{PV}, respectively.

Throughout the evolution, γ_{SP} and γ_{SV} are assumed to be constant along Γ_{SP} and Γ_{SV}, respectively. On the other hand, the particle–vapor interface has orientation-dependent energy, i.e., $\gamma_{PV}(x) = \gamma(\boldsymbol{n}(x))$, where $\boldsymbol{n}$ is the outer normal to P at a point $x \in \Gamma_{PV}$. We consider also a polar form of γ_{PV} to simplify the derivations by identifying $\boldsymbol{n}$ as $(\cos\theta, \sin\theta)$, where $\theta \in [-\pi, \pi)$ is the angle between $\boldsymbol{n}$ and the y-axis. Identifying $\boldsymbol{n}$ as unique function of θ allows to consider γ as a function of one variable θ, namely, $\gamma(\boldsymbol{n}(x)) = \gamma(\cos\theta(x), \sin\theta(x)) =: \tilde{\gamma}(\theta(x))$. For the sake of simplicity, tilde will be dropped in the ensuing text. We assume that throughout the evolution, the substrate

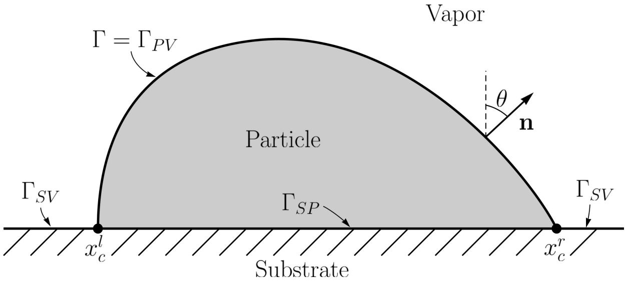

Figure 5.1: Setup and notation: a particle on a flat, rigid substrate.

$\Gamma_S = \Gamma_{SP} \cup \Gamma_{SV}$ is fixed. The contact points, also known as free boundary points, i.e., x_c^l and x_c^r may move due to the deformation of Γ. The only constraint is the area A of particle region P, i.e., during the evolution, A is preserved. Hence the problem setup leads to the total interfacial energy,

$$E(\Gamma) = \int_{\Gamma} \gamma_{PV}\, ds + \int_{\Gamma_{SP}} \gamma_{SP}\, ds + \int_{\Gamma_{SV}} \gamma_{SV}\, ds, \tag{5.1}$$

and area constraint $|P| = A$. Local minima of this energy yield equilibrium shapes of particle P.

5.1.1 Equilibrium shape

The authors in [3] define equilibrium shapes for two-dimensions as those curves Γ at which the first variation with respect to area-preserving normal perturbations and arbitrary tangential perturbations of Γ vanishes, and show that this is equivalent to the following two conditions:

$$\kappa(x)\left(\gamma''(\theta(x)) + \gamma(\theta(x))\right) = C \qquad \text{a.e. } x, \tag{5.2}$$

$$\gamma(\theta)\cos\theta - \gamma'(\theta)\sin\theta + \gamma_{SP} - \gamma_{SV} = 0 \qquad \theta = \theta_c^l, \theta_c^r. \tag{5.3}$$

Here $\kappa(x)$ is the curvature of Γ at a given point x, C is a constant determined from the area of particle, and θ_c^l, θ_c^r are the angles at the left and right contact points, respectively. For isotropic surface energy (γ = constant), (5.3) reduces to the well-known Young's equation, and thus we call (5.3) the *anisotropic Young's equation*, cf. [70].

Authors of [3] define *stable equilibrium* as those curve Γ satisfies the relation: for all $\rho > 0$, there exists $\epsilon_0 > 0$, such that when $|\epsilon| < \epsilon_0$, the following relation always holds:

$$E(\Gamma) \leqslant E(\Gamma^\epsilon) \leqslant E(\Gamma) + \rho. \tag{5.4}$$

Where Γ^ϵ denotes Γ with normal perturbations of size ϵ and arbitrary tangential perturbations. A necessary condition for stability is

$$\gamma''(\theta(x)) + \gamma(\theta(x)) \geqslant 0 \qquad \text{a.e. } x. \tag{5.5}$$

When γ satisfies this condition for all θ, equilibrium shapes can be obtained using the Winterbottom construction [71], which essentially truncates the Wulff shape corresponding to the anisotropy γ at a suitable height determined by the participating surface energies γ_{SP} and γ_{SV}, see Appendix A.2 for the details of Winterbottom construction.

5.1.2 Evolution problem

The aim is to numerically analyze evolution of particles towards equilibrium in two dimensions. In order to do that, we select one of the simplest evolution laws, namely the L^2-gradient flow of the energy (5.1), which is usually called the *weighted mean curvature flow*. In the simple case of one particle undergoing no topology change, there are only two contact points, and a standard derivation analogous to (5.2)–(5.3) (see Section 2.2 for details) yields the following evolution problem:

$$V_\perp(x) = -\mu(\theta(x))\kappa(x)\left(\gamma''(\theta(x)) + \gamma(\theta(x))\right) + C, \tag{5.6}$$

$$\gamma(\theta)\cos\theta - \gamma'(\theta)\sin\theta + \gamma_{SP} - \gamma_{SV} = 0 \qquad \theta = \theta_c^l, \theta_c^r, \tag{5.7}$$

where $V_\perp$ is the outward normal velocity of the interface, the positive function μ is the mobility of this interface and C is a constant. Notice that the sign of $\gamma'' + \gamma$ is again important here, since when $\gamma''(\theta) + \gamma(\theta)$ is negative for some angles θ, equation (5.6) becomes backwards parabolic and thus ill-posed. Therefore, we consider weak anisotropies only.

The problem (5.6)-(5.7) is a special case of the multiphase anisotropic mean curvature flow, where (5.7) corresponds to the condition that has to hold of triple junctions. The investigation of evolving triple junction started in Bronsard and Reitich [10] using theory of parabolic PDEs and was extended in several works [57, 52], but these results use the parametric approach and thus cannot handle topological changes. The first general result on the existence of MCF for networks was given by Kim and Tonegawa [49] in the framework of varifolds of geometric measure theory, resolving the question of possible triviality of the original Brakke's proof. Another important result from the viewpoint of this thesis is the convergence of a diffused approximation to this type of isotropic multiphase MCF given by Laux and Otto [55]. First results on the anisotropic multiphase problem appeared this year in [54], analyzing a tripod with smooth anisotropies and without singularities in the flow.

5.2 Derivation and stability of numerical scheme

Here we develop and analyze a thresholding algorithm for the motion of anisotropic interfaces on obstacle. The proposed scheme can handle topological changes automatically. When topology changes occur, such as merging and splitting of particles, equation (5.6) still holds for smooth parts of Γ away from singularities but it is not anymore possible to describe the evolution fully using simple formulas such as (5.6)–(5.7). Here we develop a numerical scheme that automatically deals with topology changes.

We are interested in the evolution of particle by L^2 gradient flow of (5.1), while preserving area. To do so, first we derive the thresholding algorithm and prove its stability. We closely follow the ideas in [28] and [73] for the isotropic case. According to (3.27), the total energy (5.1) can be approximated by

$$E_{\delta t}(P) = \frac{1}{\sqrt{\delta t}} \int_{\Omega} \left(1_P K_{\delta t} * 1_V + \gamma_{SP} 1_P G_{\delta t} * 1_S + \gamma_{SV} 1_S G_{\delta t} * 1_V\right) dx, \tag{5.8}$$

where K is a suitable kernel representing the anisotropy γ_{PV}. The function K is assumed to be symmetric, sufficiently smooth and (integrally) positive definite on Ω, i.e.,

$$\int_{\Omega} K(x,y)u(x)u(y)\, dx\, dy \geqslant 0 \qquad \text{for any } \ u \in L^1(\Omega).$$

Recall that all kernels introduced in Section 4.1 satisfy these conditions if the Wulff shape corresponding to the anisotropy $\gamma = \gamma_{PV}$ is centrally symmetric, convex and smooth. Since the surface tensions γ_{SP} and γ_{SV} are constant, Gaussian kernel $G_{\delta t}$ is used for the approximation of the corresponding surface energies [59]. Note that since the substrate does not deform, the evolution of the vapor region V is fully determined by that of the particle region P, which is why the approximate energy is written only as a function of P. In the sequel, this dependence will be equivalently expressed by the corresponding characteristic functions: $u = 1_P$, $1_V = 1_{\Omega^{\mathrm{up}}} - u$, i.e., we will write $E(u)$ to mean $E(P)$, where $u = 1_P$. Recall that $\Omega^{\mathrm{up}} = \overline{\Omega \backslash S}$ is the part of the domain Ω occupied by particle and vapor. Thus, we can rewrite (5.8) as follows

$$E_{\delta t}(u) = \frac{1}{\sqrt{\delta t}} \int_{\Omega} \left(u K_{\delta t} * (1_{\Omega^{\mathrm{up}}} - u) + \gamma_{SP} u G_{\delta t} * 1_S + \gamma_{SV} 1_S G_{\delta t} * (1_{\Omega^{\mathrm{up}}} - u)\right) dx,$$

We wish to minimize above expression among characteristic functions $u = 1_P$ with a given integral $\int_{\Omega} 1_P\, dx = A$, which form a non-convex set. In the following lemma, this is relaxed to a mathematically more amenable convex constraint, by allowing u to take any value between 0 and 1.

Lemma 5.2.1. *If the kernel K is smooth and positive definite, $\mathcal{L}(u)$ is a linear functional and α, β are non-negative real numbers, then to minimize $\alpha E_{\delta t}(u) + \beta \mathcal{L}(u)$ over the non-convex set*

$$\mathcal{B} = \{u \in BV(\Omega^{up})|\ u(x) \in \{0,1\} \text{ a.e. } x \in \Omega^{up},\ \int_{\Omega^{up}} u\, dx = A\}$$

is equivalent to the minimization of the same functional over the convex set

$$\mathcal{K} = \{u \in BV(\Omega^{up})|\ u(x) \in [0,1] \text{ a.e. } x \in \Omega^{up},\ \int_{\Omega^{up}} u\, dx = A\}.$$

Here BV denotes the space of functions with bounded variation.

Proof. The existence of minimizers in both $\mathcal{B}$ and $\mathcal{K}$ can be proved by the direct method when the kernel K is smooth. Since $\mathcal{B} \subset \mathcal{K}$, it is enough to prove that if $\tilde{u} \in \mathcal{K}$ is a minimizer of $\alpha E_{\delta t}(u) + \beta \mathcal{L}(u)$ in $\mathcal{K}$ then $\tilde{u} \in \mathcal{B}$. This is clear when $\alpha = 0$ since the minimizer of a linear functional over a convex set must belong to the boundary of the set.

For $\alpha > 0$, we use contradiction. Assuming $\tilde{u} \notin \mathcal{B}$, we deduce the existence of a measurable set $Z \subset \Omega^{\text{up}}$ with positive measure and of a constant $c \in (0, \frac{1}{2})$ such that

$$0 < c < \tilde{u}(x), \quad 1_{\Omega^{\text{up}}}(x) - \tilde{u}(x) < 1 - c < 1 \qquad \forall x \in Z.$$

We partition the set Z into two disjoint subsets Z_1 and Z_2 of equal measure $|Z|/2$, and define $u^t = \tilde{u} + t1_{Z_1} - t1_{Z_2}$. Note that $\int_\Omega u^t\, dx = \int_\Omega \tilde{u}\, dx = A$, and that $0 \leqslant u^t \leqslant 1$ holds for $t \in (0, c)$, so $u^t \in \mathcal{K}$ for such t. Hence, direct computation yields

$$\begin{aligned}
\frac{d^2}{dt^2}\left(\alpha E_{\delta t}(u^t) + \beta \mathcal{L}(u^t)\right) &= \alpha \frac{d^2}{dt^2} E_{\delta t}(u^t) + \beta \frac{d^2}{dt^2}\mathcal{L}(u^t) \\
&= \alpha \frac{d^2}{dt^2} E_{\delta t}(u^t) \\
&= \frac{\alpha}{\sqrt{\delta t}} \frac{d^2}{dt^2} \int_\Omega \Big(u^t K_{\delta t} * \left(1_{\Omega^{\text{up}}} - u^t\right) + \gamma_{SP} u^t G_{\delta t} * 1_S \\
&\qquad\qquad + \gamma_{SV} 1_S G_{\delta t} * \left(1_{\Omega^{\text{up}}} - u^t\right)\ dx, \\
&= \frac{\alpha}{\sqrt{\delta t}} \int_{\Omega^{\text{up}}} \frac{d}{dt} u^t K_{\delta t} * \frac{d}{dt}(-u^t)\, dx \\
&= \frac{-\alpha}{\sqrt{\delta t}} \int_{\Omega^{\text{up}}} (1_{Z_1} - 1_{Z_2}) K_{\delta t} * (1_{Z_1} - 1_{Z_2})\, dx.
\end{aligned}$$

Due to positive definiteness of the kernel K, this value is negative, which implies that $\tilde{u} = u^t|_{t=0}$ cannot be a minimizer. □

The above lemma implies that, the minimization of (5.8) can be done over the relaxed set $\mathcal{K}$ without changing the result. We solve this minimization problem by iterations. Assume we have an approximation $u^k \in \mathcal{B}$, where k is step number during iteration. Energy functional $E_{\delta t}(u)$ linearized at the point u^k reads

$$E_{\delta t}(u) = E_{\delta t}(u^k) + \mathcal{L}(u - u^k, u^k) + \text{higher order terms}$$

where

$$\begin{aligned}
\mathcal{L}(v, u^k) = \frac{1}{\sqrt{\delta t}} &\int_{\Omega^{\text{up}}} v \left(K_{\delta t} * (1_{\Omega^{\text{up}}} - u^k) + \gamma_{SP} G_{\delta t} * 1_S\right)\, dx \\
&- \frac{1}{\sqrt{\delta t}} \int_{\Omega^{\text{up}}} v \left(K_{\delta t} * u^k + \gamma_{SV} G_{\delta t} * 1_S\right)\, dx.
\end{aligned}$$

The idea then is to minimize the linearized functional:

$$\min_{u \in \mathcal{K}} \mathcal{L}(u, u^k), \tag{5.9}$$

and take the minimizer as an improved approximation u^{k+1} to the minimizer of $E_{\delta t}$. Lemma 5.2.1 guarantees that the solution of (5.9) belongs to $\mathcal{B}$. The following lemma shows that (5.9) can be solved by a simple thresholding.

Lemma 5.2.2. Write $\mathcal{L}(v, u^k)$ as $\int_{\Omega^{\text{up}}} v\phi^k \, dx$, where

$$\phi^k(x) = \frac{1}{\sqrt{\delta t}} \left(K_{\delta t} * (1_{\Omega^{\text{up}}} - 2u^k) + (\gamma_{SP} - \gamma_{SV}) G_{\delta t} * 1_S \right),$$

and let

$$P^{k+1} = \{x \in \Omega^{\text{up}} | \ \phi^k(x) < \delta^k\} \quad \text{and} \quad V^{k+1} = \Omega^{\text{up}} \backslash P^{k+1},$$

where δ^k is chosen in such a way that the area of the particle is preserved, i.e., so that $\int_{\Omega^{\text{up}}} 1_{P^{k+1}} \, dx = A$. Then $u^{k+1} = 1_{P^{k+1}}$ is a solution to (5.9).

Proof. We wish to prove $\mathcal{L}(u^{k+1}, u^k) = \min_{u \in \mathcal{K}} \mathcal{L}(u, u^k)$, which is, by Lemma 5.2.1, equivalent to

$$\mathcal{L}(u^{k+1}, u^k) \leqslant \mathcal{L}(u, u^k) \qquad \forall u \in \mathcal{B}.$$

Every element of $\mathcal{B}$ looks like $u = 1_R$ a. e. for some open set $R \subset \Omega$ such that $|R| = A$. Denote $D_1 = R \backslash P^{k+1}$ and $D_2 = P^{k+1} \backslash R$. Due to the area constraint, D_1 and D_2 satisfy $|D_1| = |D_2|$. Note that

$$\begin{aligned} &\phi^k(x) \geqslant \delta^k \quad \forall x \in D_1 \subset \Omega^{\text{up}} \backslash P^{k+1} \qquad \text{and} \\ &\phi^k(x) < \delta^k \quad \forall x \in D_2 \subset P^{k+1}. \end{aligned}$$

Using these inequalities we calculate

$$\begin{aligned} \mathcal{L}(u^{k+1}, u^k) - \mathcal{L}(u, u^k) &= \int_{\Omega^{\text{up}}} (u^{k+1} - u)\phi^k \, dx = \int_{D_1} (-\phi^k) \, dx + \int_{D_2} \phi^k \, dx \\ &\leqslant \int_{D_1} (-\delta^k) \, dx + \int_{D_2} \delta^k \, dx = \delta^k(-|D_1| + |D_2|) = 0, \end{aligned}$$

reaching the desired conclusion.

□

We arrive at the thresholding Algorithm 6.

Algorithm 6 Evolution of anisotropic particle on substrate

Given phases P^k, $V^k \subset \Omega^{\text{up}}$ at time $t_k = k \cdot \delta t$, to get new phases P^{k+1} and V^{k+1} at next time step $t_{k+1} = (k+1)\delta t$, perform the following two steps:

$$\begin{aligned} &\text{Convolution :} \quad \phi^k(x) = \tfrac{1}{\sqrt{\delta t}} \left(K_{\delta t} * (1_{\Omega^{\text{up}}} - 2u^k) + (\gamma_{SP} - \gamma_{SV}) G_{\delta t} * 1_S \right), \\ &\text{Thresholding:} \quad P^{k+1} = \left\{ x \in \Omega^{\text{up}} | \ \phi^k(x) < \delta^k \right\}, \quad V^{k+1} = \Omega^{\text{up}} \backslash P^{k+1}. \end{aligned}$$

Here δ^k is chosen so that the area of phase P^{k+1} is equal to the area A of phase P^k.

Next we show that this algorithm is stable, that is, the total energy $E_{\delta t}(P^k)$ is a non-increasing function of k.

Theorem 5.2.3. Set $u^k = 1_{P^k}$ for $k = 0, 1, 2, ...$, where P^k is obtained in Algorithm 6. Then

$$E_{\delta t}(u^{k+1}) \leqslant E_{\delta t}(u^k) \qquad \text{for all } \ k = 0, 1, 2, \dots \ \text{ and all } \ \delta t > 0. \tag{5.10}$$

Proof. Definitions of $E_{\delta t}$ and $\mathcal{L}$ and Lemma 5.2.2 yield

$$E_{\delta t}(u^k) - \frac{1}{\sqrt{\delta t}} \int_{\Omega^{\text{up}}} \left(u^k K_{\delta t} * u^k + \gamma_{SV} G_{\delta t} * 1_S \right) dx = \mathcal{L}(u^k, u^k) \geqslant \mathcal{L}(u^{k+1}, u^k). \tag{5.11}$$

Furthermore,

$$\begin{aligned} \mathcal{L}(u^{k+1}, u^k) = E_{\delta t}(u^{k+1}) - \frac{1}{\sqrt{\delta t}} \int_{\Omega^{\text{up}}} \Bigg(& u^{k+1} K_{\delta t} * u^k + u^k K_{\delta t} * u^{k+1} \\ & - u^{k+1} K_{\delta t} * u^{k+1} + \gamma_{SV} G_{\delta t} * 1_S \Bigg) dx \end{aligned} \tag{5.12}$$

Gathering (5.11) and (5.12) leads to

$$E_{\delta t}(u^{k+1}) \leqslant E_{\delta t}(u^k) + \mathcal{Y}, \tag{5.13}$$

where

$$\begin{aligned} \mathcal{Y} &= \frac{1}{\sqrt{\delta t}} \int_{\Omega^{\text{up}}} \left(u^{k+1} K_{\delta t} * u^k + u^k K_{\delta t} * u^{k+1} - u^{k+1} K_{\delta t} * u^{k+1} - u^k K_{\delta t} * u^k \right) dx \\ &= -\frac{1}{\sqrt{\delta t}} \int_{\Omega^{\text{up}}} (u^{k+1} - u^k) K_{\delta t} * (u^{k+1} - u^k) \, dx \\ &\leqslant 0. \end{aligned} \tag{5.14}$$

(5.13) and (5.14) finish the proof of the theorem. □

The convergence of Algorithm 6 to the L^2-gradient flow of the energy E as $\delta t \to 0+$ was proved in [55] in the isotropic setting without obstacle but remains open for the anisotropic case and for the problem with obstacle.

5.3 Numerical results

In this section, we carry out numerical tests using smooth four-fold anisotropy by implementing the new thresholding scheme. We check the agreement between analytical and numerical results of each kernel by investigating their respective errors and contact angles. In short, we try to justify our numerical scheme by showing consistent results with the analytical solution. As an output, we also determine which kernel is suitable for the numerical realization of the obstacle problem.

Evolving particle on substrate is a three-phase problem and thus a new issue that was not present in the two-phase setting of Section 3.3 is the realization of correct contact angles at the triple point where the three phases meet. Therefore, in numerical tests, besides the error measuring the discrepancy in the shape of the interface, we focus on the quality with which thresholding Algorithm 6 approximates the exact contact angles. Moreover, we investigate all kernels which are introduced in Section 4.1, to find a suitable kernel for obstacle problems. The evaluation is carried out based on the stationary solution of the area-preserving anisotropic mean curvature flow on obstacle.We obtain the analytical solution by *Winterbottom construction* (see Appendix A.2) and exact contact angles by solving anisotropic Young equation (5.3).

5.3.1 Error analysis

We use the same setup for error and triple point analysis. We fix the computation domain as $\Omega = [-5, 5] \times [-5, 5]$. The size of the domain is sufficiently large; so that, it will not influence the evolution of the particle. The region below $y = 0$ represents the flat substrate. The square $[-1.25, 1.25] \times [0, 2.5]$ is initial shape of the particle. We select four-fold anisotropy $\gamma(\theta) = 1 + 0.05 \cos 4\theta$; moreover particle-substrate and substrate-vapour anisotropies are set to $\gamma_{SP} = 1.5$ and $\gamma_{SV} = 1$, respectively. The corresponding equilibrium solution is obtained using *Winterbottom construction*. Winterbottom solution is depicted in solid black line in Figure 5.2. We will calculate the error after particle

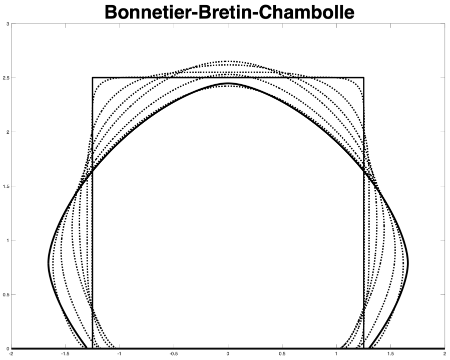

Figure 5.2: Evolving particle on substrate with anisotropies $\gamma = 1 + 0.05\cos 4\theta$, $\gamma_{SP} = 1.5$ and $\gamma_{SV} = 1$. Evolution of particle by BBC kernel at times $0, 10\delta t, 25\delta t, 50\delta t, 192\delta t$ and $672\delta t$, for $dx = 0.0024$ and $\delta t = 0.0078$; solid line represents analytical solution.

reaches numerically stable solution, i.e., when no change occurs between two subsequent time steps. We chose natural mobility, except EE kernel, to keep the obstacle problem consistent with the kernel comparison tests of Section 4.2. We evolve the initial square particle by implementing Algorithm 6 while preserving area of the particle. To preserve the area, we use the sorting approach, see Section 3.2.2. Implementation of sorting approach is possible because the substrate is fixed; thus, technically obstacle problem becomes a two-phase area-preserving problem in the sense of area preservation. To preserve the area, we sort the values of ϕ^k (see convolution step in Algorithm 6) at each grid point. Then we find the correct thresholding height δ^k by selecting first A_{grid} grid points from the accending sorted list, where A_{grid} is area of initial particle in terms of grid points. We implemented Algorithm 6 for each kernel using several combinations of spatial mesh size dx and time step δt and measured the error. For the obstacle problem, the definition of error is slightly different from the previous chapter. Here error is the set difference of the analytical and numerical solution, divided by the area of particle. Hence, the error can be written as follows:

$$\text{error} = \frac{|1_{P_A} - 1_P|}{A}, \tag{5.15}$$

where 1_{P_A} is characteristic function of analytical solution obtain by *Winterbottom construction*, 1_P is a characteristic function of numerical solution, and A is the area of the initial shape.

We report the obtained results in Figure 5.3. After inspecting results for all four kernels, we observe EJZ kernel shows the least compatibility with the stationary solution, giving the weakest convergence order. Moreover, during simulation, we observe oscillating behaviour near the numerical stationary solution. We remark that the non-monotone jumpy behaviour of the error may also be caused by the absence of subgrid accuracy improvement in these simulations. However, the irregular behaviour of the EJZ error seems to be inherent to the kernel itself, as already hinted at in [30].

On the other hand, EJZ-F kernel shows jumpy behaviour in error. The exact reason for this irregular behaviour of EJZ-F kernel is not known. In the original paper [30], authors already pointed out the incompatibility of EJZ-F kernels to deal with multiphase problems.

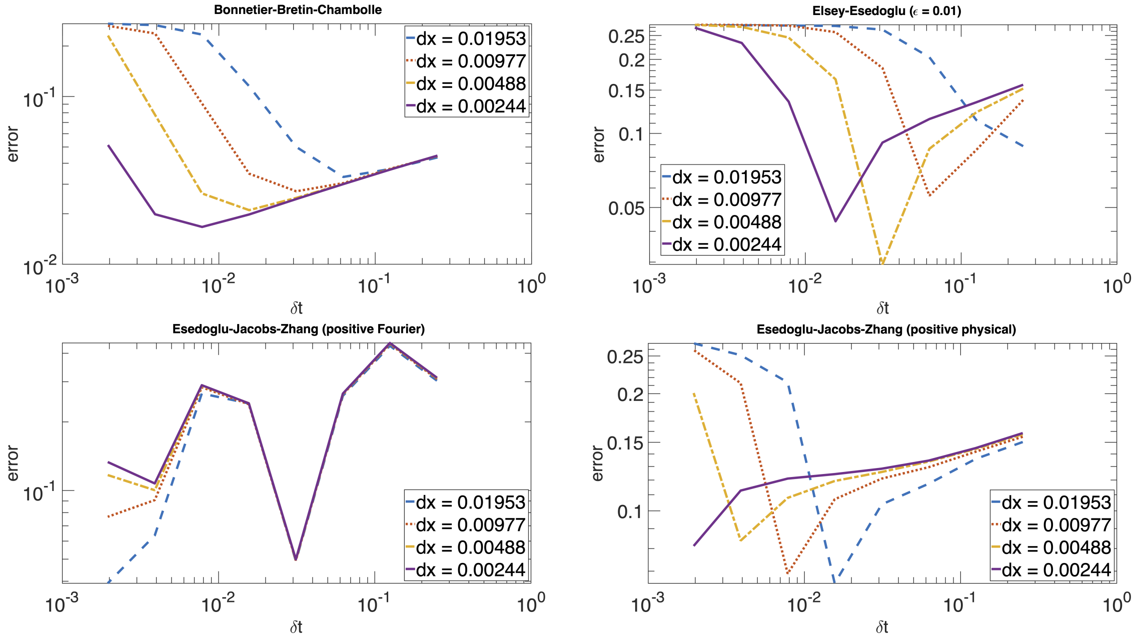

Figure 5.3: Evolving particle on substrate with anisotropies $\gamma = 1 + 0.05\cos 4\theta$, $\gamma_{SP} = 1.5$ and $\gamma_{SV} = 1$. All four figures show log-log plots of the dependence of relative error in shape on time step δt for various spatial mesh resolutions dx.

EE kernel shows a reasonable convergence rate compared to the other kernels, but error size is quite significant. This could be due to oscillatory behaviour observed for most of dx–δt combinations in the numerical solution obtained by EE kernels near the stationary state. Similar to a two-phase case, we also notice the effect of the regularizing parameter ϵ in the obstacle problem. Each choice of the ϵ gives a certain limit of a diffusion time δt, beyond which, a distorted solution is observed. This fact can be observed by inspecting $dx = 0.0048$ and $dx = 0.00244$ in top-right plot in Figure 5.3. We chose $\epsilon = 0.01$, since this choice of ϵ gives better results, as we noticed in the numerical tests in Section 4.2.

Surprisingly, BBC kernel shows the best performance among all kernels, despite the fact that it was invented first, while other kernels are devised as its improvement. BBC kernel shows a consistent convergence rate, and the size of the error is least compared to other kernels. After inspecting error, convergence rate, and time to construct the kernel, we conclude that BBC kernel is the desired kernel for the obstacle problem.

5.3.2 Contact point analysis

In this section, we analyze the numerical contact points, which are obtained after implementing thresholding scheme. Numerical contact angles are obtained by fitting a linear function to several points representing numerical interface near the substrate, excluding points in the immediate vicinity of the substrate. The dependence of resulting values of contact angles on the range of points selected for fitting is negligible, as long as the fitting points do not extend too far from the substrate. Since symmetry is preserved by the scheme, we present contact angle at the left triple point only.

We investigate the consistency of numerical contact angle with analytical solution, i.e., solution of the anisotropic Young equation (5.3). We solve (5.3) by using Matlab's inbuilt function *fzeros*, which uses bisection and interpolation methods to obtain roots of nonlinear functions, see left plot in Figure 5.4. The analytical value of a contact angle is 2.223 radian, which is 127.36 degree.

Calculation of numerical contact angle

To obtain numerical contact angle, we use the linear regression method via Matlab's *polyfit* function. We derive contact angle in three steps as follows:

First, we need a set of points (say, $\{\mathcal{P}_i\}$) which represent the particle near triple point. Here, $\{\mathcal{P}_i\}$ means the places where the interface of particle intersect with grid lines (horizontal, vertical or both). In our problem, we chose points up to a distance of 0.2 from the substrate. Note that we exclude few points adjacent to triple point because the thresholding scheme does not precisely approximate motion near triple point. This is due to the fact that dynamics near triple points occur on the different scale of diffusion time compared to the rest of the interface [28]. We use the interpolation method to capture points $\mathcal{P}_i$ on the interface, see right plot in Figure 5.4.

In the second step, we adopt linear regression. The line $Y = mX + c$ is fitted through $\{\mathcal{P}_i\}$. To do so we use the inbuilt function of Matlab software, namely, *polyfit*. The *polyfit* solve $Vp = y$ system for polynomial p, where V is Vandermonde matrix whose elements

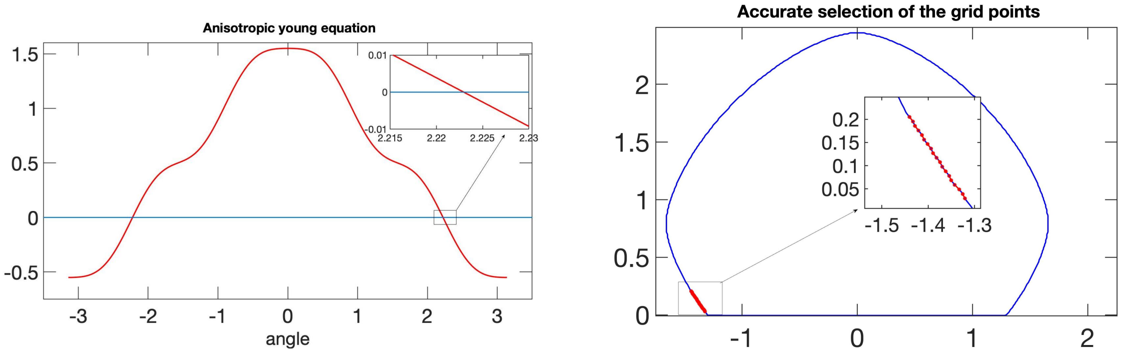

Figure 5.4: Anisotropy: $\gamma = 1 + 0.05 \cos 4\theta$, $\gamma_{SP} = 1.5$ and $\gamma_{SV} = 1$. Left: $f(\theta) = \gamma(\theta)\cos\theta - \gamma'(\theta)\sin\theta + \gamma_{SP} - \gamma_{SV}$ versus θ. Right: calculation of numerical contact angle; blue: numerical stable solution, red: selected points on the interface to evaluate contact angle.

come from $\{\mathcal{P}_i\}$. At last, we obtain the contact angle by simply taking $\arctan$ of the slope m. Note that the domain of the tan inverse is $[-\pi/2, \pi/2]$; therefore, the angle has to be changed by $\pm\pi$ according to necessity.

Numerical analysis of contact angle

In this subsection, we investigate the behaviour of triple points. We obtain the contact angles for each kernel. The results are presented in the Figure 5.5. As mentioned earlier, we present results for one triple point only because of symmetry.

After inspection, we notice that EJZ kernel shows a feeble response to actual triple point value. A possible reason for such contact angle is the oscillatory behaviour near the stationary solution. On the other hand, EJZ-F kernel shows jumpy behaviour in contact angle, which may be caused by the absence of subgrid accuracy improvement. However, the irregular behaviour of the EJZ-F kernel seems to be inherent to the kernel itself, as already hinted in [30].

EE kernel shows consistent performance like convergence analysis tests in Section 5.3.1 and Section 4.2.1. We set regularizng parameter to $\epsilon = 0.01$. However, the difference between analytical and numerical contact angles is quite significant. This could be due to oscillatory behaviour observed for most of $dx - \delta t$ combinations in the numerical solution obtained by EE kernels near the stationary state.

BBC kernel shows the best and consistent performance among all these kernels, and we can confirm this fact by inspecting the left-top plot in Figure 5.5. For each choice of dx, we can find δt such that the contact angle is close to analytical value. In order to compare

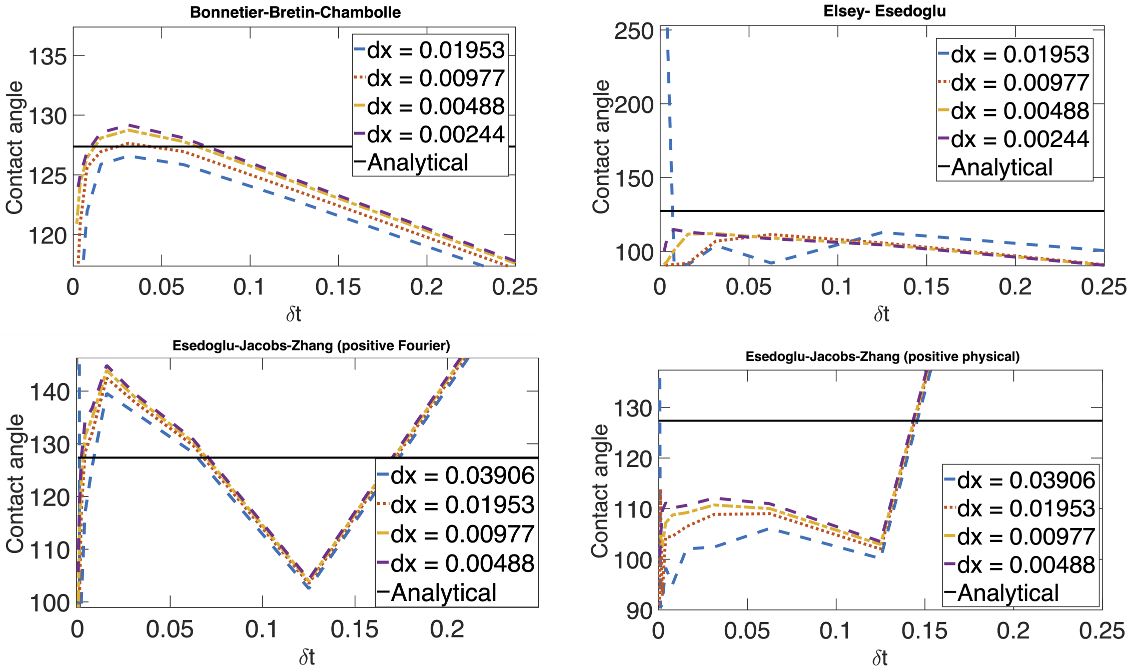

Figure 5.5: Evolving particle on substrate with anisotropies $\gamma = 1 + 0.05\cos 4\theta$, $\gamma_{SP} = 1.5$ and $\gamma_{SV} = 1$. All four figures show the contact angle value at the stable numerical solution on time step δt for various spatial mesh resolutions dx for all four kernels.

all kernels, we plot contact angles obtained by each kernel for fixed $dx = 0.0098$, see Figure 5.6. This plot clearly shows the dominance of BBC kernel.

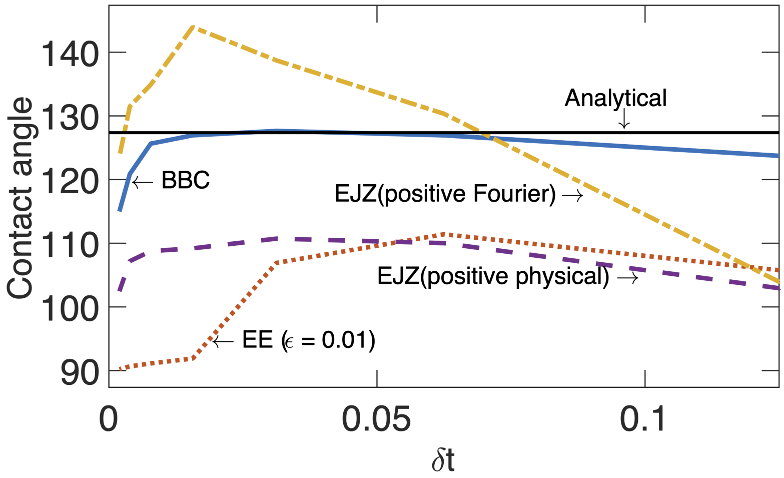

Figure 5.6: Evolving particle on substrate with anisotropies $\gamma = 1 + 0.05\cos 4\theta$, $\gamma_{SP} = 1.5$ and $\gamma_{SV} = 1$. Numerical contact angle versus time step δt for $dx = 0.0098$.

If we consider error, convergence order, contact angle, time to construct the kernel and computation time, then BBC kernel outperforms all other kernels. In the next section, we upgrade our numerical scheme for better accuracy of contact angles. Since BBC showed better results than other kernels, we use BBC kernel for the upcoming section.

5.4 Modified algorithm to improve contact angle

In this section, we modify Algorithm 6 to get more accurate contact angle. According to Theorem 5.2.3, the thresholding algorithm decreases total energy over a time, irrespective of a choice of δt. However, when space is discretized, smaller δt does not necessarily entail improved quality of the approximation. For a given space discretization, thresholding scheme approximates the evolution of particle provided that the diffusion timestep is sufficiently large.

As discovered in Section 4.2.1 the optimal δt for a given dx is of the order dx. On the other hand, the dynamics near triple points is known to occur on the scale of $\sqrt{\delta t}$ [28]. Consequently, to get an accuracy of order δt including triple points, one would need to take a spatial mesh of size δt^2, so that stagnation of interfaces is avoided. This problem was addressed in [73] by introducing time step scaling. The authors start with a relatively large time step δt ($2dx$, to be exact) and compute the evolution until the interface does not evolve anymore. Then the time step is decreased, e.g., by halving, and the evolution, especially around triple points, is refined. Since the interfaces away from junctions are already in their right position when the time step halving starts, the stagnation phenomenon has smaller impact on the outcome.

The paper [73] introduced time step halving for obstacle problems with the isotropic energy. We extend their method to obstacle problems with anisotropic energy. Further, unlike original paper, we started with various time steps and studied the output's behaviour. Extension of this idea leads to Algorithm 7, where new parameter $\tau > 0$ is introduced to evaluate the difference between two solutions at consecutive time steps. If the set difference of two consecutive solutions is greater than τ, then algorithm behaves like Algorithm 6; but when it is less than τ, we halve the timestep and go back to the convolution step. The new parameter τ has a direct impact on numerical stable shape. In Algorithm 7, if we choose $\tau = 0$ then modified algorithm is identical to Algorithm 6, and it does not improve the accuracy of contact angles.

For numerical analysis, the whole setup and parameters are the same as Section 5.3.1, including the definition of the error, the method to find error, the method to calculate contact angle, etc. We only change surface energies as follows: $\gamma(\theta) = 1 + 0.05\cos(4\theta + 8)$, $\gamma_{SP} = 1$ and $\gamma_{SV} = 1.1$. We chose these anisotropies because the corresponding stable shape is tilted, thus leading to different contact angles on both ends. We obtain stable solution using *Winterbottom construction*, see Figure 5.7. Note that stable shape has one corner close to substrate. As pointed out in the previous section, BBC kernel tends to smooth out the corners. Therefore, we can expect large error in left contact angle.

Algorithm 7 Evolution of anisotropic particle on substrate (modified algorithm)

Given initial phases P^0, $V^0 \subset \Omega^{\text{up}}$, time step δt^0 and a threshold τ, to generate phases P^{k+1} and V^{k+1} at time steps $t_{k+1} = t_k + \delta t^k$, $k = 0, 1, 2, \ldots$, set $P^* = P^0$ and repeat the following steps:

$$\text{Convolution}: \quad \phi^k(x) = \frac{1}{\sqrt{\delta t^k}} \left(K_{\delta t^k} * (1_{\Omega^{\text{up}}} - 2u^k) + (\gamma_{SP} - \gamma_{SV}) G_{\delta t^k} * 1_S \right),$$

$$\text{Thresholding:} \quad P^{k+1} = \left\{ x \in \Omega^{\text{up}} | \ \phi^k(x) < \delta^k \right\}, \quad V^{k+1} = \Omega^{\text{up}} \backslash P^{k+1}.$$

Time scaling: · If $|P^k - P^{k+1}| > \tau$, set $\delta t^{k+1} = \delta t^k$ and go to next convolution step.
· If $|P^k - P^{k+1}| \leqslant \tau$ and $|P^* - P^{k+1}| \geqslant \tau$, set $\delta t^{k+1} = \delta t^k/2$, $P^* = P^{k+1}$, and go to next convolution step.
· If $|P^k - P^{k+1}| \leqslant \tau$ and $|P^* - P^{k+1}| < \tau$, terminate.

Here δ^k is chosen so that the area of phase P^{k+1} is equal to the area A of phase P^0.

During simulation, we found that values of τ close to 0 help to get better contact angles. At the same time, too small a value of τ deteriorates the overall results. On the other hand, large value of τ leads to a wrong contact angle; hence, we need a moderately small value for the τ. Our analysis found that $\tau = 0.0001A$ is good choice for error and contact angle improvement, where A represents particle's area. Any choice of τ less than $0.0001A$ is either damaging overall error or contact angle, depending on the pair of $dx - \delta t$.

We expect to get better results from the modified algorithm; therefore, it is necessary to compare results obtained by Algorithm 7 and Algorithm 6. We perform a series of numerical tests with the help of setup mentioned above and BBC kernel. Results obtained by both algorithms are presented in Figure 5.7 and Table 5.1.

After inspecting the numerical results, we notice the superiority of modified algorithm over regular algorithm. As expected, both error and contact angles improved in the modified version. In fact each choice of δt shows better agreement with the analytical solutions in the modified version. Note that initial δt should be sufficiently large to avoid stagnation effect.

Surprisingly, computational time required for the modified algorithm is less than the original algorithm, even though modified algorithm gives better results. We see this time

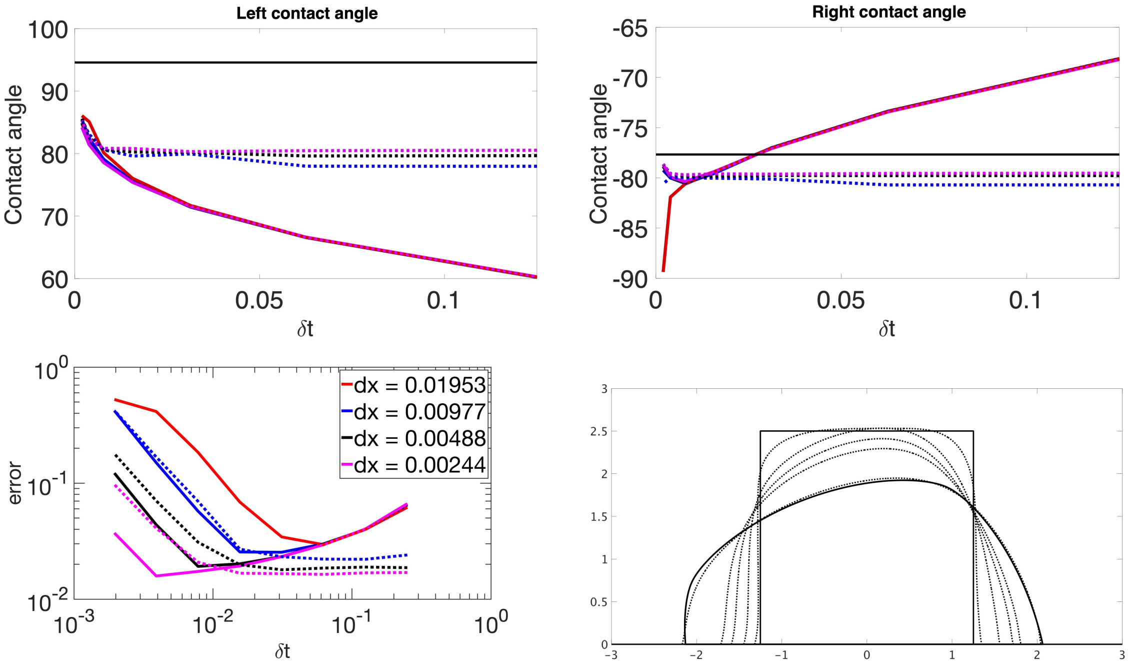

Figure 5.7: Analysis of Algorithm 7 modified for contact angle improvement (dotted lines) in comparison to the original Algorithm 6 (solid lines). A tilted four-fold anisotropy $\gamma(\theta) = 1 + 0.05\cos(4\theta + 8)$, and $\gamma_{SP} = 1$, $\gamma_{SV} = 1.1$ are adopted. Figures on top show the obtained contact angles, where the black lines signify the analytical contact angles $94.58°$ (left), $-77.67°$ (right). Figures in the second row show log-log plots of error in shape for several values of dx, and the computed evolution of particle at times $0, 10\delta t, 50\delta t, 100\delta t, 150\delta t$ and $616\delta t$, with $dx = 0.0024$ and $\delta t = 0.0078$ (here solid line represents analytical stationary solution).

Time step δt	Error in area	C.A. (left)	C.A. (right)	CPU time
0.2500	0.0163 [0.0670]	81.15 [51.87]	-79.03 [-60.34]	54 [18] min
0.1250	0.0161 [0.0404]	81.15 [60.30]	-79.40 [-68.23]	50 [51] min
0.0625	0.0158 [0.0297]	81.23 [66.64]	-79.06 [-73.45]	58 [69] min
0.03125	0.0157 [0.0234]	80.85 [71.54]	-79.49 [-77.08]	79 [102] min
0.01562	0.0161 [0.0192]	80.87 [75.40]	-79.54 [-79.40]	119 [190]min

Table 5.1: Contrast between modified Algorithm 7 and original Algorithm 6 [shown in brackets]. Here $dx = 0.00122$, and the correct contact angles are $94.58°$ (left) and $-77.67°$ (right).

difference because of the termination criteria in respective algorithms. In the modified algorithm, repetitive time halving decreases time step δt to such value, where interface does not move at all; this results in the termination of the code. On the other hand, original algorithm performs convolution-thresholding steps until interface does not move by at least one grid point. In other words, the original algorithm moves interface slowly but steadily over a more extended period.

Modified algorithm does not give a smaller error than error given by optimal δt in original algorithm. This may be because of the stagnation of interface away from contact points. In conclusion, if we consider error, contact angles and computational time, then modified algorithm outperforms original algorithm.

5.5 Topological changes

The ability of handling topological changes automatically is a major advantage of level set methods. Most of previous work on obstacle problem uses explicit representation of the interface, i.e., front-tracking or finite elements, which requires an extra ad-hoc numerical surgery when particles merge or split.

Here we present two examples of simulations involving topology change of particles moving on substrate, namely splitting and merging. In order to devise an experiment that leads to splitting, we consider a patterned substrate, where the effective surface tension $\gamma_S^{\text{split}} := \gamma_{SP} - \gamma_{SV}$ depends on the position on the substrate. For simplicity, we use an analogous pattern γ_S^{merge} for the merging simulation. Specifically, we set

$$\gamma_S^{\text{split}}(x) = \begin{cases} \gamma_{S_2} = 2 & \text{for } x \in (-0.5, 0.5) \\ \gamma_{S_1} = 0 & \text{otherwise} \end{cases},$$

$$\gamma_S^{\text{merge}}(x) = \begin{cases} \gamma_{S_2} = -0.1 & \text{for } x \in (-0.5, 0.5) \\ \gamma_{S_1} = 0 & \text{otherwise.} \end{cases}$$

In the thresholding algorithm, when computing the convolution $G_{\delta t} * 1_S$, these values are extended to the substrate region as constants in the normal direction, as shown in Figure 5.8, that is, we replace $(\gamma_{SP} - \gamma_{SV})G_{\delta t} * 1_S$ by $\gamma_{S_1} G_{\delta t} * 1_{S_1} + \gamma_{S_2} G_{\delta t} * 1_{S_2}$. We consider two-fold anisotropy $\gamma(\theta) = 1 + 0.3\cos(2\theta + \pi)$ and set up the initial condition as a rectangle for the splitting experiment and as two right-angled triangles at distance 0.4 apart for the merging experiment (see solid lines in Figure 5.8). We used time step $\delta t = 0.0039$ and spatial grid size $dx = 0.0024$.

As shown in Figure 5.8, in the splitting simulation particle split into two parts at 26th time step, and after that these parts were treated as two different particles with their own preserved areas. In the merging simulation, two particles attached at 50th time step and from 51st time step on the algorithm treated them as a single particle with area equal to the sum of areas of initial particles. Note that detecting the connectivity of particles cannot be avoided if one wants to preserve the area of each particle separately. Thanks to

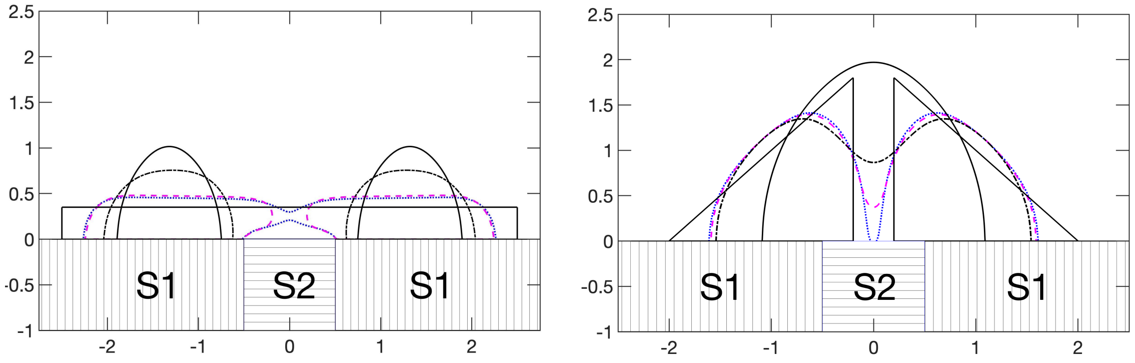

Figure 5.8: Evolutions undergoing topological change for $\gamma = 1 + 0.3\cos(2\theta + \pi)$ and $dx = 0.0024$, $\delta t = 0.0039$. The initial and final shape are shown in black solid line. (Left) Splitting with $\gamma_{S_1} = 0, \gamma_{S_2} = 2$, intermediate lines showing evolution at times $25\delta t, 28\delta t, 70\delta t$. (Right) Merging with $\gamma_{S_1} = 0, \gamma_{S_2} = -0.1$, intermediate lines showing evolution at times $49\delta t, 55\delta t, 75\delta t$.

the symmetry of the initial configuration in our simulations, it was algorithmically easy to detect the time when topology change occurred. However, to detect topology changes happening in the evolution of a general initial configuration of particles, one needs to include a connectivity check at every time step of the algorithm. A disadvantage of the algorithm is that due to the diffusion step, two particles sense each other even before they actually attach. This may be physically correct but the mesh size (and consequently also the time step) have to be chosen small enough to resolve or satisfactorily approximate the physically correct ”sensing distance”.

Chapter 6

Conclusions and future work

6.1 Conclusions

In this thesis, we developed a stable thresholding scheme for obstacle problems, which can handle topological changes and approximate anisotropic mean curvature flow, and proved its stability unconditional. Before dealing with the obstacle problem, we surveyed known convolution kernels used in thresholding scheme since there is no systematic comparison of the numerical performance available in literature. For the basic two-phase problem, we perform comparison tests with the following criteria in mind: • Behaviour of error and convergence order. • Time required for computation. • Ability to handle sharp corners. • Evolution of non-convex shapes.

Theoretically, first-order convergence in time is predicted, and our numerical analysis confirmed this fact. Differences were observed regarding the numerical performance of kernels. Elsey-Esedoglu kernel shows good agreement with the analytical result but its mobility is fixed, and its construction demands substantial computational time. Esedoglu-Jacobs-Zhang kernels lead to moderate error and demand decent time for construction. Bonnetier-Bretin-Chambolle kernel gives expected convergence order and has least error among all kernels, at least for the tested anisotropy. On the other hand, this kernel smoothes out corners, hence is not recommended for crystalline anisotropies.

On the other hand, for the three-phase obstacle problem, although all kernels are able to approximate the correct solution to some extent, it was found that each of the kernels has certain drawbacks: Esedoglu-Jacobs-Zhang kernels lead to large errors, Elsey-Esedoglu kernels show spurious oscillations, while Bonnetier-Bretin-Chambolle kernel excessively smooths out sharp corners.

6.2 Future work

(I) We are going to address the issues mentioned in the previous section. First, we will study the motion of triple junction and then numerically realize its anisotropic motion by establishing a robust scheme. To the end, we will consider three curves with one end attached to domain boundary, and another end is a junction. This setting will help us to understand the motion of triple junction.

(II) Based on the results of (I), we will further extend the scheme to the multiphase case, where two or more particles are attached and have anisotropic interfacial energy. We are expecting to develop a scheme for the volume-preserving case, too.

(III) We are planning to construct the algorithm in three dimensions, which can handle evolution of any number of particles with automatic handling of topological changes and preserving volume. Currently, we are working on the same problem but in two dimensions.

(IV) Since all the existing kernels have some drawbacks, we will work on constructing a new convolution kernel. We are expecting that the new kernel will not have the issues, which are present in current kernels.

Appendix A

Appendix

A.1 Construction of Wulff shape

To contrive simpler form of a Wulff shape, we assume that the anisotropy γ is positively one homogeneous i.e., $\gamma(\alpha x) = |\alpha|\gamma(x)$ where $\alpha \in \mathbb{R}\backslash\{0\}$ and $x \in \mathbb{R}^d$.

$$\begin{aligned}
\mathcal{W}_\gamma &= \{\xi^o \in \mathbb{R}^d \mid \gamma^o(\xi^o) \leqslant 1\} \\
&= \{\xi^o \mid \sup_{\xi \in B_\gamma} \langle \xi^o, \xi \rangle \leqslant 1\} \\
&= \{\xi^o \mid \langle \xi^o, \xi \rangle \leqslant 1, \quad \forall \xi \in \partial B_\gamma\} \\
&= \{\xi^o \mid \langle \xi^o, \frac{\xi}{\gamma(\xi)} \rangle \leqslant 1, \quad \forall \xi \in \mathbb{R}^d\}, \qquad \gamma\text{is 1-homogenous} \\
&= \{\xi^o \mid \langle \xi^o, \xi \rangle \leqslant \gamma(\xi) \quad , \forall \xi \in \mathbb{R}^d\} \\
&= \{\xi^o \mid \langle \xi^o, \boldsymbol{n} \rangle \leqslant \gamma(\boldsymbol{n}), \quad \forall \boldsymbol{n} \text{ unit}\} \qquad \boldsymbol{n} = \frac{\xi}{|\xi|} \\
&= \bigcap_{\boldsymbol{n} \,:\, \|\boldsymbol{n}\|=1} \{\xi^o \mid \langle \xi^o, \boldsymbol{n} \rangle \leqslant \gamma(\boldsymbol{n}\} \\
&= \bigcap_{\boldsymbol{n} \,:\, \|\boldsymbol{n}\|=1} \{\xi^o \mid |\xi^o| \cos\phi \leqslant \gamma(\boldsymbol{n}\}.
\end{aligned} \tag{A.1}$$

Where ϕ is angle between $\boldsymbol{n} \in \mathbb{S}^{d-1}$ and ξ^o. Probably, the easiest way to foresee (A.1) is the following; for fix $\boldsymbol{n}$ find the set $H(\boldsymbol{n}) = \{\xi^o \mid \langle \xi^o, \boldsymbol{n} \rangle \leqslant \gamma(\boldsymbol{n})\}$. $H(\boldsymbol{n})$ is a half plane whose boundary passes through the point $(\gamma(\boldsymbol{n}) \cdot \boldsymbol{n})$ and perpendicular to $\boldsymbol{n}$. Each $\boldsymbol{n}$ yields one $H(\boldsymbol{n})$, and taking the intersection of all such $\{H(\boldsymbol{n})\}_i$ sets, determines the Wulff shape. See Fig. 2.2 for some examples of Wulff shapes.

A.2 Winterbottom construction

For free particle, Wulff shape is equilibrium solution and as mentioned earlier, for weak anisotropy its boundary can be given as:

$$\mathcal{W}_\gamma^e = (x(\theta), y(\theta)), \quad \theta \in [-\pi, \pi)$$

where $x(\theta) = -\gamma \sin\theta - \gamma^{'} \cos\theta,\ y(\theta) = \gamma\cos\theta - \gamma^{'}\sin\theta$. Equilibrium solution for obstacle problem is proposed in [71] by Winterbottom. We can obtain equilibrium shape of particle on *flat* substrate by using the so-called Winterbottom construction.

Suppose particle possesses anisotropic surface energy γ. To obtain equilibrium shape, first plot Wulff shape and then cut the Wulff shape parallel to $x-$axis at $y = \gamma_{sp} - \gamma_{sv}$. Denote $\gamma_{sp} - \gamma_{sv}$ by σ to simplify upcoming equations. This yields a paramatrization of boundary of equilibrium shape E_s as follows:

$$E_s = (x_w(\theta), y_w(\theta)),$$

where $x_w(\theta) = -\gamma\sin\theta - \gamma^{'}\cos\theta,\ y_w(\theta) = \gamma\cos\theta - \gamma^{'}\sin\theta - \sigma$ and $\theta \in [\theta_l, \theta_r]$. Note that $y_w(\theta)$ is identical to anisotropic Young equation (5.3). Hence it guarantees that contact angle obtained by Winterbottom construction will be identical to analytical contact angle.

Normalized equilibrium shape

The area of equilibrium shape obtained by Winterbottom method is different from the actual area (initial area of particle, i.e., A); therefore, we need a normalized equilibrium shape.

Denote the area of equilibrium shape obtained by Winterbottom method as A_w, then

$$A_w = \frac{1}{2}\int_{\theta_l}^{\theta_r} x_w y_w^{'} - y_w x_w^{'} d\theta \pm A_T = \frac{1}{2}\int_{\theta_l}^{\theta_r} \gamma(\gamma + \gamma^{''})\, d\theta \pm A_T \tag{A.2}$$

where, $A_T = |x_r - x_l|(\sigma/2)$ is area of a triangle whose vertices are contact points and Wulff point. Wulff point is nothing but the centre of Wulff shape. When Wulff point lies above the substrate, then A_T acquires minus sign in (A.2). On the other hand, if Wulff point lies below substrate, then sign change to positive. We use area term to normalize parametric form of equilibrium shape as follows:

$$x_w^n(\theta) = \sqrt{\frac{A}{A_w}}\Big(x_w(\theta)\Big), \;\; y_w^n(\theta) = \sqrt{\frac{A}{A_w}}\Big(y_w(\theta)\Big). \tag{A.3}$$

In this thesis, we use (A.3) for all numerical tests, whenever necessary.

A.3 First variation: Isotropic two phase problem

Define $\Gamma = \{g(s) = (g_1(s), g_2(s)) \,|\, s \in [a, b)\}$ and $g : [a, b] \to \mathbb{R}^2$ is differentiable and $g(a) = g(b)$. Then first variation of energy is given by

$$\begin{aligned}
\frac{d}{d\epsilon}E(\Gamma_\epsilon)\big|_{\epsilon=0} &= \lim_{\epsilon\to 0}\frac{1}{\epsilon}(E(\Gamma_\epsilon) - E(\Gamma)) \\
&= \lim_{\epsilon\to 0}\int_a^b \frac{1}{\epsilon}(|(g+\epsilon\phi)^{'}| - |g^{'}|)\,ds \\
&= \lim_{\epsilon\to 0}\int_a^b \frac{1}{\epsilon}\frac{|(g+\epsilon\phi)^{'}|^2 - |g^{'}|^2}{|(g+\epsilon\phi)| + |g^{'}|}\,ds \\
&= \lim_{\epsilon\to 0}\int_a^b \frac{1}{\epsilon}\frac{|g^{'}|^2 + \epsilon^2|\phi^{'}| + 2\epsilon g^{'}\cdot\phi^{'} - |g^{'}|^2}{|(g+\epsilon\phi)| + |g^{'}|}\,ds \\
&= \lim_{\epsilon\to 0}\int_a^b \frac{\epsilon|\phi^{'}| + 2g^{'}\cdot\phi^{'}}{|(g+\epsilon\phi)| + |g^{'}|}\,ds \\
&= \int_a^b \frac{(g^{'}\cdot\phi^{'})}{|g^{'}|}\;ds \\
&= \int_a^b \left(\frac{g^{'}}{|g^{'}|}\right)\cdot\phi^{'}\;ds \\
&= \left(\frac{g^{'}}{|g^{'}|}\right)\phi|_a^b - \int_a^b \left(\frac{g^{'}}{|g^{'}|}\right)^{'}\cdot\phi\;ds \qquad \text{Integration by parts} \\
&= 0 - \int_a^b \left(\frac{g^{'}}{|g^{'}|}\right)^{'}\cdot\phi\;ds \qquad \phi(a) = \phi(b) \\
&= \int_a^b \Big(\kappa\boldsymbol{n}|g^{'}|\Big)\cdot\phi\;ds \qquad \text{Frenet - Serret formula} \\
&= \int_a^b \kappa\,(\boldsymbol{n}\cdot\phi)\,|g^{'}|\;ds \\
&= \int_\Gamma \kappa\,(\boldsymbol{n}\cdot\phi)\;\;dl \qquad dl = |\Gamma^{'}|ds
\end{aligned} \tag{A.4}$$

A.4 A listicle of anisotropies

Here we present several examples of anisotropies from literature [22, 9, 25, 30, 64].

$$
\begin{aligned}
(a)\,\gamma &= \sqrt{\sum_{i=1}^{3}(\lambda_i x_i)^2}, \;\; \lambda_i \in \mathbb{R} \\
(b)\,\gamma &= |X|_{l^r} = \left(\sum_{k=1}^{3}|x_k|^r\right)^{1/r}, \;\; 1 \leqslant r \leqslant \infty \\
(c)\,\gamma &= \sqrt{GX \cdot X}, \text{ where } G \text{ is positive definite matrix.} \\
(d)\,\gamma &= \sqrt{x_1^2\left[\frac{11}{2} + \frac{9}{2}sign(x_1)\right] + x_2^2} \\
(e)\,\gamma &= |X|_{l^2}\left[1 - A\left(1 - \frac{|X|_{l^4}^4}{|X|_{l^2}^4}\right)\right], \text{where} A < 0.25. \\
(f)\,\gamma &= \left[|x_1|^{1001} + \left|\frac{x_1}{2} + \frac{\sqrt{3}x_2}{2}\right|^{1001} + \left|\frac{x_1}{2} - \frac{\sqrt{3}x_2}{2}\right|^{1001}\right]^{\frac{1}{1001}} \\
(g)\,\gamma &= |x_2| + \frac{1}{\sqrt{2}}|x_1 + x_2| + \frac{1}{\sqrt{2}}|x_1 - x_2| \\
(h)\,\gamma &= |x_1| + |x_2| + \frac{1}{\sqrt{2}}|x_1 + x_2| + \frac{1}{\sqrt{2}}|x_1 - x_2| \\
(i)\,\gamma &= \sqrt{\frac{x_1^2}{4} + x_2^2} + \sqrt{\frac{x_2^2}{4} + x_1^2} \\
(j)\,\gamma &= \frac{1}{4} + \frac{5}{4}\left|\sin\left(\theta + \frac{\pi}{4}\right)\right| \\
(k)\,\gamma &= \left[(a\sqrt{x^2 + y^2})^r + (b\sqrt{x^2 + \epsilon^2 y^2})^r(c\sqrt{x^2\epsilon^2 + y^2})^r\right]^{1/r}, \; r \geqslant 1, \; a, b, c \geqslant 0 \\
(l)\,\gamma &= 1 + \beta\cos(m(\theta + \phi)), \text{ with suitable combination of } m \text{ and } \beta.
\end{aligned}
$$

All anisotropies mentioned above belong to the weakly anisotropic class, with a specific choice of their respective parameters. One can obtain strong anisotropies by adjusting parameters in weak anisotropy. In the above list, $(a), (b), (d), (f) - (j)$ can not be modified to strong anisotropy.

A.5 Sub-grid accuracy

Let U^k be a given diffused form of particle. As a first step, we bring the excpected interface to 0-level set of M as follows:

$$M = (U^k - K_{\text{area}}/2)/K_{\text{area}}$$

If we replace all the negative values in M by 0 and all positive values by 1, we obtain a characteristic function for the next time step, which is not smooth.

To obtain the smooth version of the characteristic function, we consider a neighbourhood of each grid point (let's call central point), which consist of 8 grid points, see the figure given below. We excluded the boundary points of the domain from these calculations. If all these 8 neighbouring points have an identical sign, i.e., plus or minus, then the value of central point is either 0 or 1, depending on the sign.

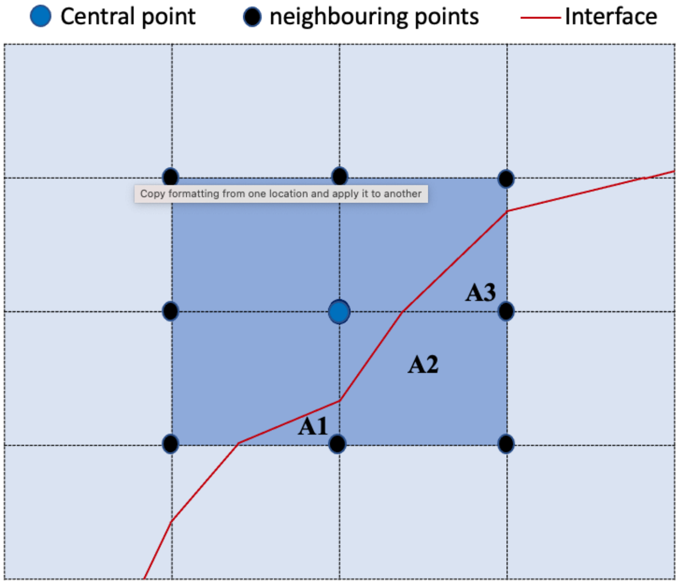

If these points have different signs, then value of central point belong to $(0, 1)$. To find exact value of central point, we need to work further. Consider the interface passing through grid cells, as shown in the above figure, as a red piecewise linear function. Note that neighbouring points give four grid cells, highlighted by dark shade in the above figure. We calculate each grid cell's area that lies inside the interface, i.e., area of triangle $A1$ in the first cell, area of pentagon $A2$ in the second cell, again area of triangle $A3$ in third cell. We calculate the value of the central point by taking the average of all these areas, i.e., $(A1 + A2 + A3)/(4dx^2)$, here dx is length of grid cell.

Derivation to calculate area of grid cell which lie inside the interface is given below. Let a function $u(x)$ in a grid cell $dx \times dx$ be given by four values at the vertices:

$$u(0,dx) = u_1, \quad u(dx,dx) = u_2, \quad u(0,0) = u_3, \quad u(dx,0) = u_4.$$

These values can be interpolated by a bilinear function

$$u(x,y) = ax + by + cxy + d, \qquad a,b,c,d \in \mathbb{R}.$$

Taking into account the values at vertices, we can compute the coefficients a, b, c, d and get

$$u(x,y) = \frac{u_4 - u_3}{dx}x + \frac{u_1 - u_3}{dx}y + \frac{-u_1 + u_2 + u_3 - u_4}{dx^2}xy + u_3.$$

To find the proportion of area divided by the interface, which is the zero level set of the function $u(x)$, we describe the interface by the graph of a function of y taken from the line $x = dx$. This means we need to solve $u(x,y) = 0$ for x, which yields

$$x = -\frac{by + d}{cy + a}.$$

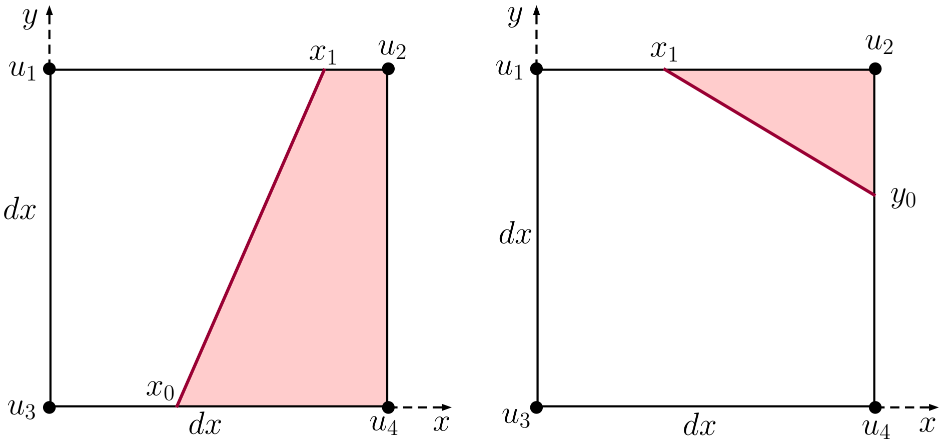

- In the situation of the figure on the left ($u_1 < 0, u_2 > 0, u_3 < 0, u_4 > 0$), the area of the red region is

$$\begin{aligned}
|\{u>0\}| &= dx^2 - \int_0^{dx} -\frac{by+d}{cy+a}\,dy = dx^2 + \frac{b}{c}\int_0^{dx} \frac{y+\frac{d}{b}}{y+\frac{a}{c}}\,dy \\
&= dx^2 + \frac{b}{c}\int_0^{dx}\left(1+\frac{\frac{d}{b}-\frac{a}{c}}{y+\frac{a}{c}}\right)dy \\
&= dx^2 + \frac{b}{c}dx + \left(\frac{d}{c}-\frac{ab}{c^2}\right)\ln\left(y+\frac{a}{c}\right)\Big|_0^{dx} \\
&= dx^2 + \frac{b}{c}dx + \frac{cd-ab}{c^2}\ln\left(1+\frac{c}{a}dx\right) \\
&= \left[\frac{u_2-u_4}{-u_1+u_2+u_3-u_4} + \frac{u_2u_3-u_1u_4}{(-u_1+u_2+u_3-u_4)^2}\ln\frac{u_2-u_1}{u_4-u_3}\right]dx^2.
\end{aligned}$$

This formula does not work as it is when $c' = -u_1+u_2+u_3-u_4 = 0$ There are several ways to resolve this - computing it as a limit, or approximating the term $\ln\left(1+\frac{c}{a}dx\right)$ up to second order by $\frac{c}{a}dx - \frac{1}{2}\frac{c^2}{a^2}dx^2$. Then we get

$$\begin{aligned}
|\{u>0\}| &\approx dx^2 + \frac{b}{c}dx + \frac{cd-ab}{c^2}\left(\frac{c}{a}dx - \frac{1}{2}\frac{c^2}{a^2}dx^2\right) \\
&= \left(1+\frac{ab-cd}{2a^2}\right)dx^2 + \frac{d}{a}dx \\
&= \left(\frac{u_4}{u_4-u_3} + \frac{u_1u_4-u_2u_3}{2(u_4-u_3)^2}\right)dx^2.
\end{aligned}$$

Another (probably best) way is to compute the points of intersection x_0, x_1 of the interface with grid lines and approximate the interface by a straight line connecting those two points. In this case,

$$x_0 = -\frac{d}{a}, \qquad x_1 = -\frac{b\cdot dx+d}{c\cdot dx+a}.$$

Then the area of red region is approximately

$$|\{u>0\}| = dx^2 - \frac{x_0+x_1}{2}dx = \frac{u_2(u_4-u_3)+u_4(u_2-u_1)}{2(u_4-u_3)(u_2-u_1)}dx^2.$$

- In the situation of the figure on the right ($u_1<0, u_2>0, u_3<0, u_4<0$), the intersection of the red line and the vertical line $x = dx$ has the coordinates

$$(dx, y_0) = \left(dx, -\frac{a\cdot dx+d}{c\cdot dx+b}\right),$$

and the area of the red region is

$$
\begin{aligned}
|\{u>0\}| &= dx(dx-y_0) - \int_{y_0}^{dx} -\frac{by+d}{cy+a}\,dy = dx(dx-y_0) + \frac{b}{c}\int_{y_0}^{dx} \frac{y+\frac{d}{b}}{y+\frac{a}{c}}\,dy \\
&= dx(dx-y_0) + \frac{b}{c}\int_{y_0}^{dx} \left(1+\frac{\frac{d}{b}-\frac{a}{c}}{y+\frac{a}{c}}\right) dy \\
&= dx(dx-y_0) + \frac{b}{c}(dx-y_0) + \left(\frac{d}{c}-\frac{ab}{c^2}\right)\ln\left(y+\frac{a}{c}\right)\Big|_{y_0}^{dx} \\
&= \left(dx+\frac{b}{c}\right)(dx-y_0) + \frac{cd-ab}{c^2}\ln\left(1+\frac{c(dx-y_0)}{a+cy_0}\right).
\end{aligned}
$$

Here,

$$
dx{-}y_0 = \frac{u_2}{u_2-u_4}dx, \qquad cd{-}ab = \frac{u_2u_3-u_1u_4}{dx^2}, \qquad \frac{c(dx-y_0)}{a+cy_0} = \frac{u_2cdx^2}{u_1u_4-u_2u_3},
$$

so

$$
|\{u>0\}| = \left[\frac{u_2}{-u_1+u_2+u_3-u_4} + \frac{u_2u_3-u_1u_4}{(-u_1+u_2+u_3-u_4)^2}\ln\frac{(u_1-u_2)(u_4-u_2)}{u_1u_4-u_2u_3}\right]dx^2.
$$

Again, this does not work always and may cause problems in the code even when c is close to zero, so we again consider approximation of the interface by straight line. Then

$$
\begin{aligned}
|\{u>0\}| \approx \frac{1}{2}(dx-x_1)(dx-y_0) &= \frac{1}{2}\left(dx+\frac{b\cdot dx+d}{c\cdot dx+a}\right)\left(dx+\frac{a\cdot dx+d}{c\cdot dx+b}\right) \\
&= \frac{u_2^2}{2(u_2-u_1)(u_2-u_4)}.
\end{aligned}
$$

- All other cases can be reduced to the above two.

A.6 Front tracking solution

We present an overview of the front tracking method developed by D. Sevcovic and S. Yazaki in [66]. Authors propose a method of tangential redistribution of points using curvature adjusted control in the tangential motion of evolving interfaces. The tangential velocity distribution of points representing interface is uniform as well as acquire suitable concentration and/or dispersion depending on the curvature. Basically, authors solve nonlinear PDEs arising by a position vector, tangent angle and curvature of a curve. They use a semi-implicit numerical discretization scheme based on the flowing finite volume method. A summary of their method is given below.

Consider a simple, embedded and closed curve Γ parameterized by a smooth function $\boldsymbol{x} : [0,1] \subset \mathbb{R}/\mathbb{Z} \to \mathbb{R}^2$ such that $\Gamma = \{\boldsymbol{x}(u) \,:\, u \in [0,1]\}$ and $g = |\partial_u \boldsymbol{x}| > 0$.

Let $\boldsymbol{x} \in \Gamma(t)$ be the position vector, and denote the tangential angle by ν and unit tangent vector by $\boldsymbol{t}$; further, $\beta = \beta(\boldsymbol{x}, \nu, \kappa) = \mu(\gamma''(\boldsymbol{n}) + \gamma(\boldsymbol{n}))$ then normal velocity V is the normal component of the following evolutionary equation for the position vector $\boldsymbol{x}$:

$$\partial_t \boldsymbol{x} = \beta \boldsymbol{n} + \alpha \boldsymbol{t}. \tag{A.5}$$

Here, α is the tangential component of the velocity vector. The authors point out that motion in the tangential direction does not affect evolving shape and shape of closed curve is obtained by the value of normal velocity. The basic setting, with $\alpha = 0$ does not redistribute the points.

Without loss of generality, rewrite the normal velocity V as follows:

$$V = \omega(\boldsymbol{x}, \nu, \kappa)\kappa, \tag{A.6}$$

here, $\omega(\boldsymbol{x}, \nu, \kappa) = \mu(\gamma''(\boldsymbol{n}) + \gamma(\boldsymbol{n}))$. If ∂_s^2 and ∂_s denotes arc-length derivatives then Frenet–Serret formula gives $\partial_s^2 \boldsymbol{x} = \partial_s \boldsymbol{t} = \kappa \boldsymbol{n}$; further (A.5) allows to write the following equation for the position vector

$$\partial_t \boldsymbol{x} = \omega \partial_t^2 \boldsymbol{x} + \alpha \partial_s \boldsymbol{x}. \tag{A.7}$$

The authors explicitly gave a formula for the desired tangential velocity α. We fixed some parameters in that equation (as suggested by authors) and ended up with the tangential velocity α satisfying the following equation:

$$\partial_s \alpha = V\kappa - \overline{V\kappa} + (c_1 + c_2 \overline{V\kappa}) \left(\frac{L(t)}{g} - 1 \right), \tag{A.8}$$

where $c_1, c_2 \geqslant 0$ are constants, $L(t)$ is the total length of $\Gamma(t)$ and $\overline{F}$ denotes the average of function F along the curve $\Gamma(t)$. To obtain the unique solution α, authors consider the following condition on α:

$$\overline{\alpha} = 0. \tag{A.9}$$

Authors solve the flow equation by discretizing (A.7) and the tangential velocity equation (A.8) with the constraint (A.9), using finite volume method.

A.7 Fourier transform of $g_{\nu,\epsilon}$

Here we present a detailed derivation of the Fourier transform of (4.6). To make formulas shorter, we set $\epsilon_1 = \epsilon^2 - 1, q = 2\pi, a_1 = \epsilon_1\nu_1^2 + 1, a_2 = \epsilon_1\nu_2^2 + 1, H = 2i\epsilon^2$ and $G = \epsilon_1\nu_1\nu_2$.

$$
\begin{aligned}
\hat{g}_{\nu,\epsilon}(\xi) &= \int_{\mathbb{R}^2} g_{\nu,\epsilon}(x)\ \exp(-2\pi i x\cdot\xi)\ dx \\
&= \frac{1}{4\pi\epsilon}\int_{\mathbb{R}^2} \exp\left(-\frac{(\epsilon^2-1)(x\cdot\nu)^2 + |x|^2 + q4i\epsilon^2 x\cdot\xi}{4\epsilon^2}\right)\ dx \\
&= \frac{1}{4\pi\epsilon}\int_{\mathbb{R}^2} \exp\left(-\frac{\epsilon_1[x^2\nu_1^2 + y^2\nu_2^2 + 2xy\nu_1\nu_2] + x^2 + y^2 + 2qH(x\xi_1 + y\xi_2)}{4\epsilon^2}\right)\ dx \\
&= \frac{1}{4\pi\epsilon}\int_{\mathbb{R}^2} \exp\left(-\frac{x^2[a_1] + 2x[yG + qH\xi_1]}{4\epsilon^2}\right)\exp\left(-\frac{y^2[a_2] + 2qHy\xi_2}{4\epsilon^2}\right)\ dx \\
&= \frac{1}{4\pi\epsilon}\int_{\mathbb{R}^2} \exp\left(-\frac{x^2[a_1] + 2x[yG + qH\xi_1] + \frac{[yG+qH\xi_1]^2}{a_1}}{4\epsilon^2}\right) \\
&\qquad\qquad \exp\left(-\frac{y^2[a_2] + 2qHy\xi_2 - \frac{[yG+qH\xi_1]^2}{a_1}}{4\epsilon^2}\right) dx \\
&= \frac{1}{4\pi\epsilon}\int_{\mathbb{R}^2} \exp\left(-\left[\frac{x\sqrt{a_1} + \frac{[yG+qH\xi_1]}{\sqrt{a_1}}}{2\epsilon}\right]^2\right) \\
&\qquad\qquad \exp\left(-\frac{y^2[a_2] + 2qHy\xi_2 - \frac{[y^2G^2 + (qH\xi_1)^2 + 2GHqy\xi_1]}{a_1}}{4\epsilon^2}\right) dx \\
&= \frac{1}{4\pi\epsilon}\int_{\mathbb{R}}\int_{\mathbb{R}} \exp\left(-\eta^2\right)\ \frac{2\epsilon}{\sqrt{a_1}}\ d\eta \\
&\qquad\qquad \exp\left(-\frac{y^2[a_2 - \frac{G^2}{a_1}] + 2yq\left[H\xi_2 - \frac{[GH\xi_1]}{a_1}\right] - \frac{(qH\xi_1)^2}{a_1}}{4\epsilon^2}\right) dy
\end{aligned}
$$

$$\begin{aligned}
&= \frac{1}{2\sqrt{\pi}\sqrt{a_1}} \int_{\mathbb{R}} \exp\left(- \frac{y^2[a_2 - \frac{G^2}{a_1}] + 2yq\left[H\xi_2 - \frac{[GH\xi_1]}{a_1}\right] - \frac{(qH\xi_1)^2}{a_1}}{4\epsilon^2} \right) dy \\
&= \frac{1}{2\sqrt{\pi a_1}} \int_{\mathbb{R}} \exp\left(- \frac{y^2[a_2 - \frac{G^2}{a_1}] + 2yq\left[H\xi_2 - J\right] - \frac{(qH\xi_1)^2}{a_1}}{4\epsilon^2} \right) dy, \quad \text{where } J = \frac{GH\xi_1}{a_1}, \\
&= \frac{1}{2\sqrt{\pi a_1}} \exp\left(\frac{(qH\xi_1)^2}{4\epsilon^2 a_1} + \frac{q^2\left[H\xi_2 - J\right]^2}{4\epsilon^2 K} \right) \\
&\qquad \int_{\mathbb{R}} \exp\left(- \frac{y^2 K + 2yq\left[H\xi_2 - J\right] + \frac{q^2[H\xi_2 - J]^2}{K}}{4\epsilon^2} \right) dy, \quad \text{where } K = a_2 - \frac{G^2}{a_1}, \\
&= \frac{1}{2\sqrt{\pi a_1}} \exp\left(\frac{(qH\xi_1)^2}{4\epsilon^2 a_1} + \frac{q^2\left[H\xi_2 - J\right]^2}{4\epsilon^2 K} \right) \int_{\mathbb{R}} \exp\left(- \left[\frac{y\sqrt{K} + \frac{q[H\xi_2 - J]}{\sqrt{K}}}{2\epsilon} \right]^2 \right) dy \\
&= \frac{1}{2\sqrt{\pi a_1}} \exp\left(\frac{(qH\xi_1)^2}{4\epsilon^2 a_1} + \frac{q^2\left[H\xi_2 - J\right]^2}{4\epsilon^2 K} \right) \int_{\mathbb{R}} \exp\left(-\eta^2\right) \frac{2\epsilon}{\sqrt{K}} \, d\eta \\
&= \frac{\epsilon}{\sqrt{K}\sqrt{a_1}} \exp\left(\frac{(qH\xi_1)^2}{4\epsilon^2 a_1} + \frac{q^2\left[H\xi_2 - J\right]^2}{4\epsilon^2 K} \right) \\
&= \frac{\epsilon}{A} \exp\left(\frac{q^2}{4\epsilon^2}[B + C] \right), \text{ where } A = \sqrt{K a_1}, B = \frac{(H\xi_1)^2}{a_1} \text{ and } C = \frac{[H\xi_2 - J]^2}{K}. \qquad \text{(A.10)}
\end{aligned}$$

Let us simplify A,

$$\begin{aligned}
A^2 &= K a_1 = a_1 \left(a_2 - \frac{G^2}{a_1} \right) \\
&= a_1 \left(a_2 - \frac{\epsilon_1^2 (\nu_1 \nu_2)^2}{a_1} \right) \\
&= a_1 \left(a_2 a_1 - (\epsilon^2 - 1)(\nu_1 \nu_2)^2 \right), \quad \epsilon_1 = \epsilon^2 - 1 \\
&= (\epsilon^2 - 1)^2 \nu_1^2 \nu_2^2 + 1 + (\epsilon^2 - 1)(\nu_2^2 + \nu_1^2) - (\epsilon^2 - 1)(\nu_1 \nu_2)^2 \\
&= 1 + (\epsilon^2 - 1)(1), \quad \nu \in \mathbb{S}^1 \\
&= \epsilon^2. \qquad \text{(A.11)}
\end{aligned}$$

Further we calculate $B + C$.

$$\begin{aligned}
B + C &= \frac{(H\xi_1)^2}{a_1} + \frac{[H\xi_2 - J]^2}{K} = \frac{(H\xi_1)^2}{a_1} + \frac{\left[H\xi_2 - \frac{GH\xi_1}{a_1}\right]^2}{K} \\
&= \frac{(H\xi_1)^2}{a_1} + \frac{\left[H\xi_2 - \frac{GH\xi_1}{a_1}\right]^2}{a_2 - \frac{G^2}{a_1}} \\
&= \frac{(2i\epsilon^2\xi_1)^2}{[\epsilon_1 \nu_1^2 + 1]} + \frac{\left[2i\epsilon^2\xi_2 - \frac{[2i\epsilon_1\epsilon_1\nu_1\nu_2\epsilon^2\xi_1]}{\epsilon_1\nu_1^2 + 1}\right]^2}{\left[\epsilon_1\nu_2^2 + 1 - \frac{\epsilon_1^2(\epsilon_1\nu_1\nu_2)^2}{\epsilon_1\nu_1^2 + 1}\right]}
\end{aligned}$$

$$
\begin{aligned}
&= \frac{(2i\epsilon^2\xi_1)^2}{a_1} + \frac{\left[2i\epsilon^2\xi_2 - \frac{[2i\epsilon_1\nu_1\nu_2\epsilon^2\xi_1]}{a_1}\right]^2}{\left[a_2 - \frac{(\epsilon_1\nu_1\nu_2)^2}{a_1}\right]} \\
&= \frac{(2i\epsilon^2\xi_1)^2\left[a_2 - \frac{(\epsilon_1\nu_1\nu_2)^2}{a_1}\right] + a_1\left[2i\epsilon^2\xi_2 - \frac{[2i\epsilon_1\nu_1\nu_2\epsilon^2\xi_1]}{a_1}\right]^2}{a_1\left[a_2 - \frac{(\epsilon_1\nu_1\nu_2)^2}{a_1}\right]} \\
&= \frac{(2i\epsilon^2\xi_1)^2\left[\frac{a_1a_2-(\epsilon_1\nu_1\nu_2)^2}{a_1}\right] + \frac{1}{a_1}\left[a_1 2i\epsilon^2\xi_2 - [2i\epsilon_1\nu_1\nu_2\epsilon^2\xi_1]\right]^2}{A^2} \\
&= \frac{(2i\epsilon^2\xi_1)^2\left[\frac{A^2}{a_1}\right] + \frac{1}{a_1}\left[a_1 2i\epsilon^2\xi_2 - [2i\epsilon_1\nu_1\nu_2\epsilon^2\xi_1]\right]^2}{A^2} \\
&= \frac{(i\epsilon^2\xi_1)^2\left[A^2\right] + \left[a_1 i\epsilon^2\xi_2 - [i\epsilon_1\nu_1\nu_2\epsilon^2\xi_1]\right]^2}{\frac{a_1A^2}{4}} \\
&= \frac{(\xi_1)^2\left[A^2\right] + \left[a_1\xi_2 - \epsilon_1\nu_1\nu_2\xi_1\right]^2}{\frac{-a_1A^2}{4\epsilon^4}} \\
&= \frac{(\xi_1)^2\left[A^2 + \epsilon_1^2\nu_1\nu_2\right] + {\xi_2}^2a_1^2 - [2a_1\xi_2\epsilon_1\nu_1\nu_2\xi_1]}{\frac{-a_1A^2}{4\epsilon^4}} \\
&= \frac{(\xi_1)^2\left[a_1a_2\right] + {\xi_2}^2a_1^2 - [2a_1\xi_2\epsilon_1\nu_1\nu_2\xi_1]}{\frac{-a_1A^2}{4\epsilon^4}} \\
&= \frac{(\xi_1)^2\left[a_2\right] + {\xi_2}^2a_1 - [2\xi_2\epsilon_1\nu_1\nu_2\xi_1]}{\frac{-A^2}{4\epsilon^4}} \\
&= \frac{-4\epsilon^4}{A^2}\cdot(\xi_1)^2\left[\epsilon^2\nu_2^2 + \nu_1^2\right] + {\xi_2}^2\left[\epsilon^2\nu_1^2 + \nu_2^2\right] - \left[2\xi_2(\epsilon^2-1)\nu_1\nu_2\xi_1\right] \\
&= \frac{-4\epsilon^4}{\epsilon^2}\cdot\epsilon^2\left[{\xi_1}^2\nu_2^2 + {\xi_2}^2\nu_1^2 - 2\xi_2\nu_1\nu_2\xi_1\right] + \left[{\xi_1}^2\nu_1^2 + {\xi_2}^2\nu_2^2 + 2\xi_2\nu_1\nu_2\xi_1\right] \\
&= (-4\epsilon^2)\cdot\epsilon^2\left[{\xi_1}^2(1-\nu_1^2) + {\xi_2}^2(1-\nu_2^2) - 2\xi_2\nu_1\nu_2\xi_1\right] + (\xi\cdot\nu)^2 \\
&= -4\epsilon^2\left(\epsilon^2\left[-(\xi\cdot\nu)^2 + |\xi|^2\right] + (\xi\cdot\nu)^2\right) \qquad (A.12)
\end{aligned}
$$

Inserting (A.11) and (A.12) into (A.10)

$$
\begin{aligned}
\frac{\epsilon}{A}\exp\left(\frac{q^2}{4\epsilon^2}[B+C]\right) &= \frac{\epsilon}{\sqrt{\epsilon^2}}\exp\left(\frac{4\pi^2}{4\epsilon^2}\cdot -4\epsilon^2\left(\epsilon^2\left[-(\xi\cdot\nu)^2 + |\xi|^2\right] + (\xi\cdot\nu)^2\right)\right) \\
&= \exp\left(-4\pi^2\left(\epsilon^2\left[-(\xi\cdot\nu)^2 + |\xi|^2\right] + (\xi\cdot\nu)^2\right)\right) \\
&= \exp\left(-4\pi^2\epsilon^2\left[-(\xi\cdot\nu)^2 + |\xi|^2\right] - 4\pi^2(\xi\cdot\nu)^2\right) \\
&= \exp\left(-4\pi^2(\xi\cdot\nu)^2\right)\exp\left(\epsilon^2 4\pi^2\left[(\xi\cdot\nu)^2 - |\xi|^2\right]\right).
\end{aligned}
$$

Bibliography

[1] B. Andrews. *Volume-preserving anisotropic mean curvature flow*, Indiana University Mathematics Journal, 50-2, pp. 783-827 (2001).

[2] G. Aubert and P. Kornprobst. *Mathematical Problems in Image Processing*, Applied Mathematical Sciences, Springer, 147, 1-288 (2002).

[3] W. Bao, W. Jiang, D. J. Srolovitz, and Y. Wang. *Stable equilibria of anisotropic particles on substrates: A generalized Winterbottom construction*, SIAM J. Appl. Math. 77 (6), 2093-2118 (2017).

[4] G. Barles and C. Georgelin. *A simple proof of convergence for an approximation scheme for computing motions by mean curvature*, SIAM J. Numer. Anal. 32 (2), 484–500 (1995).

[5] G. Bellettini and M. Paolini. *Anisotropic motion by mean curvature in the context of Finsler geometry*, Hokkaido Math. J. 25, 537–566 (1996).

[6] G. Bellettini, V. Caselles, A. Chambolle and M. Novaga. *The volume preserving crystalline mean curvature flow of convex sets in $\mathbb{R}^N$*, Journal de Mathématiques Pures et Appliquées, 92, 499-527 (2009).

[7] M. Bertagnolli, M. Marchese, and G. Jacucci. *Modeling of particles impacting on a rigid substrate under plasma spraying conditions*, Journal of Thermal Spray Technology 4, 41–49 (1995).

[8] E. D. Bolker. *A class of convex bodies*, Trans. Amer. Math. Soc. 145, 323–345 (1969).

[9] E. Bonnetier, E. Bretin, and A. Chambolle. *Consistency result for a non monotone scheme for anisotropic mean curvature flow*, Interface Free Bound. 14, 1-35 (2012).

[10] L. Bronsard and F. Reitich. *On three-phase boundary motion and the singular limit of a vector-valued Ginzburg–Landau equation*, Arch. Rational Mech. Anal. 124, no. 4, 355-379 (1993).

[11] M. Burger, C. Stocker, and A. Voigt. *Finite element-based level set methods for higher order flows,* J. Sci. Comput., 35(2-3), 77–98 (2008).

[12] W. K. Burton, N. Cabrera and F. C. Frank. *The growth of crystals and the equilibrium structure of their surfaces*, Trans. R. Soc. Lond. A 243, 299, (1951) .

[13] F. Catte, F. Dibos, and G. Koepfler. *A morphological scheme for mean curvature motion and applications to anisotropic diffusion and motion of level sets,* SIAMJ. Numer. Anal. 32(6), 1895–1909 (1995).

[14] A. Chambolle , *An algorithm for mean curvature motion*, Interfaces Free Bound. 6, 195–218 (2004).

[15] A. Chambolle, M. Morini, and M. Ponsiglione. *Existence and uniqueness for a crystalline mean curvature flow*. Comm. Pure Appl. Math. 70(6), 1023–1220 (2017).

[16] A. Chambolle, M. Morini, M. Novaga and M. Ponsiglione. *Generalized crystalline evolutions as limits of flows with smooth anisotropies*. Anal. PDE 12(3), 789-813 (2019).

[17] Y.G. Chen, Y. Giga and S. Goto. *Uniqueness and existence of viscosity solutions of generalized mean curvature flow equations*, J. Differential Geom. 33, 749–786 (1991).

[18] Chou. *A blow-up criterion for the curve shortening flow by surface diffusion*, Hokkaido Math. J. 32(1), 1–19 (2003).

[19] U. Clarenz, F. Haußer, M. Rumpf, A. Voigt, and U. Weikard. *On level set formulations for anisotropic mean curvature flow and surface diffusion, in Multiscale Modeling in Epitaxial Growth*, Internat. Ser. Numer. Math., Birkhauser, Basel, 149, 227–237 (2005).

[20] M.G. Crandall, H. Ishii and P.L. Lions. *User's guide to viscosity solutions of second order partial differential equations*, Bull. Amer. Math. Soc. 27, 1–67 (1992).

[21] K. Deckelnick, C. M. Elliott and V. M. Styles. *Numerical diffusion-induced grain boundary motion*, Interfaces Free Bound. 3, 393–414 (2001).

[22] K. Deckelnick, G. Dziuk, C. M. Elliott. *Computation of geometric partial differential equations and mean curvature flow*, Acta Numerica 14, pp. 1–94 (2005).

[23] J.J.Eggleston, G.B.McFadden and P.W.Voorheesa. *A phase-field model for highly anisotropic interfacial energy*, Physica D: Nonlinear Phenomena, 150, 1-2, 91-103 (2001).

[24] Elliott, C.M., Garcke, H. *Existence results for diffusive surface motion laws*, Adv. Math. Sci. Appl. 7(1), 467–490 (1997).

[25] M. Elsey, and S. Esedoglu. *Threshold dynamics for anisotropic surface energies*, Math. Comput. 87(312), 1721-1756 (2017).

[26] J. Escher and G. Simonett. *The volume preserving mean curvature flow near sphere*, Proceedings of the Amer. math. Soc. 126-9, 2789-2796 (1998).

[27] K. Ecker. *Heat equations in geometry and topology*. Jahresber. Deutsch. Math.-Verein. 110(3), 117–141 (2008).

[28] S. Esedoglu, and F. Otto. *Threshold dynamics for networks with arbitrary surface tensions*, Commun. Pure Appl. Math. 68(5), 808-864 (2015).

[29] S. Esedoglu, and M. Jacobs. *Convolution kernels and stability of threshold dynamics methods*, SIAM J. Numer. Anal. 55(5), 2123-2150 (2017).

[30] S. Esedoglu, M. Jacobs, P. Zhang. *Kernels with prescribed surface tension and mobility for threshold dynamics schemes*, Journal of Computational Physics 337, 62-83 (2017).

[31] L. C. Evans and J. Spruck. *Motion of level sets by mean curvature I*, J. Differential Geom. 33, 636–681 (1991).

[32] L. C. Evans and J. Spruck. *Motion of level sets by mean curvature II*, Trans. Amer. Math. Soc. 330, 321–332 (1992).

[33] L. C. Evans and J. Spruck. *Motion of level sets by mean curvature III*, J. Geom. Anal. 2, 121–150 (1992).

[34] L. C. Evans and J. Spruck. *Motion of level sets by mean curvature IV*, J. Geom. Anal. 5, 77–114 (1995).

[35] L. C. Evans. *Convergence of an algorithm for mean curvature motion*, Indiana Univ. Math. J. 42 (2), 533–557 (1993).

[36] S. Gavhale and K. Švadlenka. *Dewetting dynamics of anisotropic particles: A level set numerical approach*, Applications of Mathematics, first online, 1-29 (2021).

[37] M. Gage, R. S. Hamilton. *The heat equation shrinking convex plane curves*, J. Differential Geom. 23(1), 69-96 (1986).

[38] M.E. Gage. *On an area-preserving evolution equation for plane curves*, Nonlinear problems in geometry (Mobile, Ala., 1985), Contemp. Math., 51 , Amer. Math. Soc., Providence, RI, 51–62 (1986).

[39] H. Garcke. *Curvature driven interface evolution*, Jahresbericht der Deutschen Mathematiker-Vereinigung, 15, 63–100 (2013).

[40] Y. Giga. *Surface Evolution Equations :A Level Set Approach*, Monographs in Mathematics, Vol.99, (2006).

[41] Y. Giga and K. Ito. *On pinching of curves moved by surface diffusion*, Commun. Appl. Anal. 2(3), 393–405 (1998).

[42] M. Grayson. *The heat equation shrinks embedded plane curves to round points*, J. Differential Geom. 26, 285–314 (1987).

[43] M. A. Grayson. *A short note on the evolution of a surface by its mean curvature*, Duke Math. J. 58(3), 555–558 (1989).

[44] J. Huang, F. Kim, A. R. Tao, S. Connor, and P. Yang. *Spontaneous formation of nanoparticle stripe patterns through dewetting*, Nature Materials 4, 896–900 (2005).

[45] G. Huisken. *Flow by mean curvature of convex surfaces into spheres*, J. Differential Geom. 20, 237–266 (1984).

[46] G. Huisken. *The volume preserving mean curvature flow*, Journal für die reine und angewandte Mathematik, 382, 35-48 (1987).

[47] H. Ishii, G E. Pires, and P.E. Souganidis. *Threshold dynamics type approximation schemes for propagating fronts*, J. Math. Soc. Japan 51(2), 267-308 (1999).

[48] W. Jiang, W. Bao, C.V. Thompson, and D.J. Srolovitz. *Phase field approach for simulating solid-state dewetting problems*, Acta Mater. 60, 5578-5592 (2012).

[49] L. Kim and Y. Tonegawa. *On the mean curvature f low of grain boundaries*, Ann. Inst. Fourier, Grenoble 67 (1) (2017).

[50] I. Kim, D. Kwon and N. Pozar. *On volume-preserving crystalline mean curvature flow*, Mathematische Annalen, (2021).

[51] M. Kimura. *Numerical analysis of moving boundary problems using the boundary tracking method*, Japan J. Indust. Appl. Math. 14, 373–398 (1997).

[52] C. Mantegazza, M. Novaga and V.M. Tortorelli. *Motion by curvature of planar networks*, Ann. Scuola Norm. Sup. Pisa CI.Sci. 5 (3), 235-324 (2004).

[53] L. Mugnai, C. Seis, and E. Spadaro. *Global solutions to the volume-preserving mean-curvature flow*. Calc. Var. 55, 18 (2016).

[54] H. Kroner, M. Novaga , and P. Pozzi. *Anisotropic Curvature Flow of Immersed Networks*, Milan J. Math. Vol. 89, 147–186 (2021).

[55] T. Laux, and F. Otto. *Convergence of the thresholding scheme for multi-phase mean-curvature flow*, Calc. Var. 55(129), (2016).

[56] T. Laux, D. Swartz. *Convergence of thresholding schemes incorporating bulk effects*. Interfaces Free Bound. 19 (2), 273–304 (2017).

[57] A. Magni, C. Mantegazza, and M. Novaga. *Motion by curvature of planar networks, II*, Ann. Sc. Norm. Super. Pisa Cl. Sci. 15 (5), 117-144 (2016).

[58] P. Mascarenhas. *Diffusion Generated Motion by Mean Curvature*, CAM report, Dept. of Math., University of California, Los Angeles, 92-33 (1992).

[59] B. Merriman, J.K. Bence, and S.J. Osher. *Motion of multiple junctions: a level set approach*, J. Comput. Phys. 112, 334-363 (1994).

[60] O. Misiats, and N. K. Yip. *Convergence of space-time discrete threshold dynamics to anisotropic motion by mean curvature*, Discrete and Continuous Dynamical Systems - A 36, 6379-6411 (2016).

[61] A.M. Oberman. *A convergent monotone difference scheme for motion of level sets by mean curvature*, Numer. Math., 99(2), 365–379 (2004).

[62] S. Osher and J. Sethian. *Fronts propagating with curvature-dependent speed: Algorithms based on Hamilton-Jacobi formulations*, J. of Comp. Physics, 79-1, 12-49 (1988).

[63] S.J. Ruuth. *Efficient algorithms for diffusion-generated motion by mean curvature*, J. Comput. Phys. 144 , 2, 603–625 (1998).

[64] S.J. Ruuth, and B. Merriman. *Convolution-generated motion and generalized Huygens' principles for interface motion*, SIAM J. Appl. Math. 60(3), 868-890, (2000).

[65] S. J. Ruuth, B.T.R. Wetton. *A simple scheme for volume-preserving motion by mean curvature*. J. Sci. Comput. 19(1–3), 373–384 (2003).

[66] D. Ševčovič, and S. Yazaki. *Evolution of plane curves with a curvature adjusted tangential velocity*, Japan J. Indust. Appl. Math. 28(3), 413-442 (2011).

[67] K. Svadlenka, E. Ginder and S. Omata. *A variational method for multiphase area-preserving interface motions*, J. Comp. Appl. Math, 257, 157-179 (2014).

[68] K. Takasao. *Existence of Weak Solution for Volume-Preserving Mean Curvature Flow via Phase Field Method*, Indiana Uni. Math. Jour., 66-6, 2015-2035 (2017).

[69] C.V. Thompson. *Solid-state dewetting of thin films*, Annual Review of Materials Research 42(1), 399–434 (2012).

[70] Y. Wang, W. Jiang, W. Bao, and D.J. Srolovitz. *Sharp interface model for solid-state dewetting problems with weakly anisotropic surface energies*, Phys. Rev. B 91, 045303, (2015).

[71] W.L. Winterbottom. *Equilibrium shape of a small particle in contact with a foreign substrate*, Acta Metallurgica 15(2), 303-310 (1967).

[72] G. Wulff. *Zur Frage der Geschwindigkeit des Wachsthums und der Auflösung der Krystallflächen*, Zeitschrift für Kristallographie, Vol.34, pp. 449 (1901).

[73] X. Xu, D. Wang, X.P. Wang. *An efficient threshold dynamics method for wetting on rough surfaces*, Journal of Computational Physics 330, 510-528 (2017).

[74] H. Yagisita. *Non-uniqueness of self-similar shrinking curves for an anisotropic curvature flow*, Calc. Var. 26(1), 49–55 (2006).